The β delayed γ and neutron emission from the ^{11}Li halo nucleus

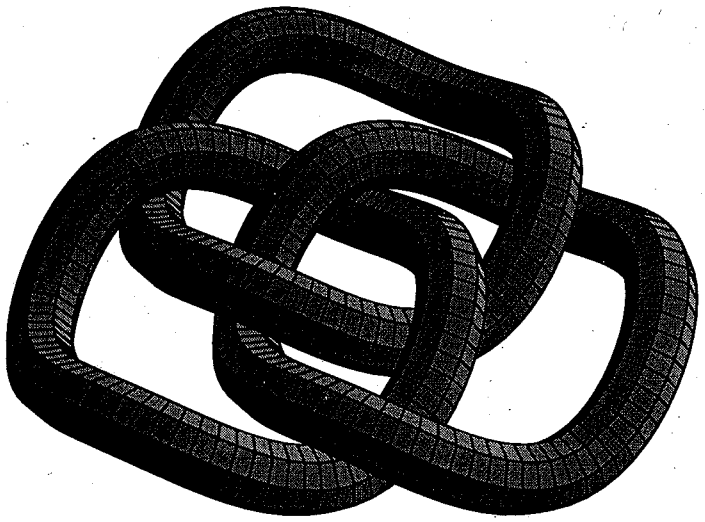

February 9, 1996

Torben Eilskov Leth,
Institute of Physics and Astronomy,
University of Aarhus,
Denmark

Dedicated in memory of my mother, Vera Leth

Contents

Front-page figure[1]**:** The Borromean rings, which are the escutcheon of the Italian family Borromeo. The family lives on the Borromean Islands (four tiny islands of about 20 ha) in Lago Maggiore in the Novara province, in the Piemonte region in northwestern Italy, and the islands have belonged to the Borromeo's since the 12th century[66]. The rings display the same binding properties as ^{11}Li (see Chapter 2).

[1]The figure is taken from the **Mathematica**[68] *vers.* 2.2.3 Notebook: *Knots and Links*

This document was prepared with LaTeX 2_ε

Chapter 1

Introduction

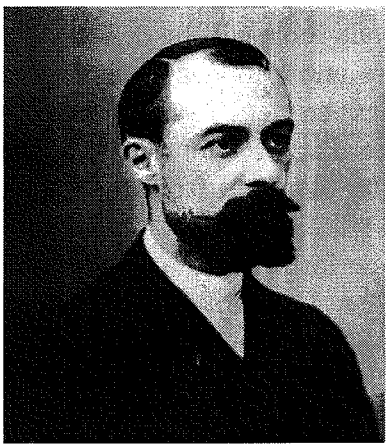

Figure 1.1: Henri Antoine Becquerel ($\star$1852 †1908) received the Nobel Price in Physics "in recognition of the extraordinary services he has rendered by his discovery of spontaneous radioactivity" [51] in 1903.

Since Henri Antoine Becquerel (see figure 1.1) in 1896 discovered spontaneous radioactivity from natural nuclei a tremendous effort has been done both theoretically and experimentally to understand nuclei, their properties and interactions. In the beginning only nuclear radiation was investigated, but when the first man-made particle accelerator was constructed by J. D. Cockcroft and E. T. S. Walton in 1932[1] a whole new dimension of nuclear

[1] They applied the high-voltage electrostatic generator made by R. J. van de Graaff in 1931

decay of ^{11}Be from the first excited state at 320 keV to the groundstate with a lifetime of the excited state of only $1.7 \cdot 10^{-13}$ s. When taking both charge and energy into account this decay is the fastest transition in nuclear physics known so far. Two years later Isao Tanihata *et al.*[65] were measuring the sizes of neutron rich radioactive ions, and they found that ^{6}He and ^{8}He and in particular ^{11}Li were much larger than expected (see figure 2.1a). There were two possible explanations for these results: either ^{11}Li was extremely deformed, which would give the same calculations of the average volume or the volume of the nucleus had indeed increased. The first possibility was soon after ruled out by Rainer Neugart *et al.*[4] by a series of optical experiments carried out at ISOLDE at CERN in Switzerland. They measured the magnetic and electric moments of radioactive lithium isotopes, and they found almost identical moments for mass 7, 9 and 11, where the first two isotopes have normal radii. This indirectly suggested that the increase in volume was due to the neutrons. In 1987 P. G. Hansen and Björn Jonson[33] pointed out

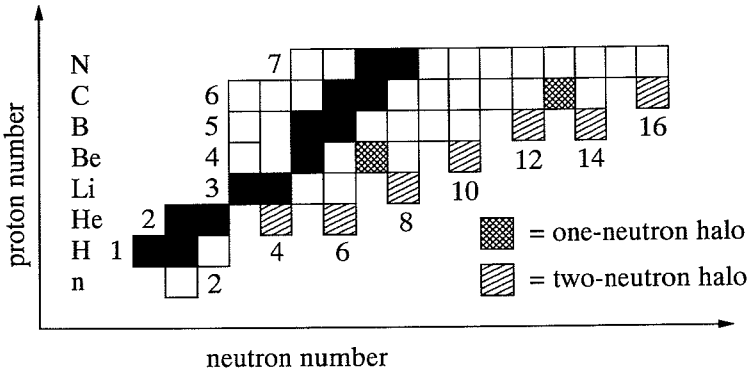

Figure 2.2: Extract of the nuclear scheme showing the lightest nuclei. The marked nuclei at the neutron drip-line have all confirmed halo structures. ^{8}He does not really fit into the marking of two-neutron halos, since it as an exception consists of four halo neutrons surrounding an α core.

that the separation energy of two neutrons in the ^{11}Li nucleus was about 0.25 MeV which is low enough to make the neutron halos very likely. This suggestion also agreed well with the results found by Rainer Neugart *et al.* In 1992 Blank *et al.*[14] measured the charge-changing cross sections for the lithium isotopes of masses 8, 9 and 11. The charge-changing cross sections are nearly equal for the three different isotopes (see figure 2.1b). Comparing them to

the total cross section[1] which increases drastically for ^{11}Li, it was concluded that the cross section belonging to the charge-change is not influenced by the halo neutrons. A further emphasis of the two-neutron halo structure.

These new discoveries gave rise to an intensive search for other possible candidates among the light neutron rich nuclei also exhibiting this new halo structure. The nuclei with experimentally confirmed halo structures known so far are shown in figure 2.2 with the exception of ^{17}B, ^{19}B and ^{22}C, which are not yet observed, but thought of being good candidates.

2.2 The ^{11}Li nucleus

The heaviest lithium nucleus, ^{11}Li, which was experimentally investigated in the experiment to be discussed in Chapter 4 and 5, has many intriguing properties. Both theoretical and experimental reviews of these properties can be found in the references [11, 31, 57, 70]. The following will consist of a brief overview of some of the properties discovered so far.

The ^{11}Li nucleus consists of a core of 3 protons and 6 neutrons and two halo neutrons spending most of the their time outside the range of the strong nuclear force (see figure 2.3). The separation energy of one and two neutrons

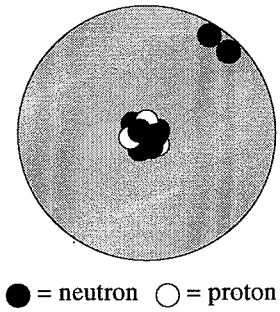

Figure 2.3: "Holographic" view of the ^{11}Li halo nucleus.

from ^{11}Li is very small as mentioned in the previous section . The separation energies are listed in table 2.1. The combination of the low separation energy and the short range of the nuclear force allows the neutrons to tunnel into the space surrounding the nuclear core (^{9}Li) so that the halo neutrons are present within a large space extent. The large space extent gives a narrow momentum distribution[3, 37], which can be explained by Heisenberg's

[1]This article contains a very good example of recurrent citation. The total cross sections are in the article taken from the authors reference [16] which is the article itself.

uncertainty relation:

$$\overline{(\Delta p)^2} \cdot \overline{(\Delta x)^2} \geq \frac{\hbar^2}{4} . \tag{2.1}$$

The correlation of the two halo neutrons is known to be important, but

ISOTOPE	Particle(s)	Separation energy[6] [MeV]
^{11}Li	n	0.720±0.070
	2n	0.310±0.040

Table 2.1: The separation energies for one and two neutrons from ^{11}Li.

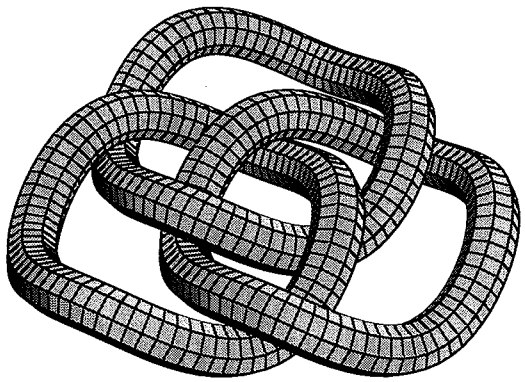

Figure 2.4: The Borromean rings (see frontpage explanation, page iii). The rings correspond to the ^{9}Li core and two neutrons, respectively

the interaction is never the less not stronger than between the neutron and the proton in deuteron which exhibit properties somewhat similar to halo nuclei. The half-life of ^{11}Li is 8.83±0.12 ms[12]. ^{11}Li can be considered as a three body system, where the core only provides the attractive potential.

The properties of the nucleus can be estimated by only looking at the tail of the wave function for the halo neutrons. The three body paradox of ^{11}Li can be visualized by the Borromean rings (see figure 2.4). The evidence so far is that the ^{10}Li nucleus is unbound and the same applies for the di-neutron. This consequently makes all three possible subsystems of ^{11}Li unbound. On the contrary, together they will be bound[70]. This phenomenon is the same for the Borromean rings which, when one ring is removed, will fall apart.

2.3 The nuclear β decay

When discussing nuclear or particle physics the following three fundamental interactions have to be considered: electromagnetic interactions where the force has a infinite range and strong and weak interactions where both forces have short ranges. Weak interactions do not normally conserve isospin opposite to the strong and electromagnetic interactions. Nuclear β decay is a manifestation of the weak interactions.

2.3.1 β decay in general

The basic β decay processes[15, page 395] can be divided into three main categories:

$$n \rightarrow p + e^- + \overline{\nu} \qquad \text{negative beta decay} \quad (\beta^-) \tag{2.2}$$

$$p \rightarrow n + e^+ + \nu \qquad \text{positive beta decay} \quad (\beta^+) \tag{2.3}$$

$$p + e^- \rightarrow n + \nu \qquad \text{orbital electron capture} \quad (\varepsilon) \tag{2.4}$$

One should add here that there exist two other processes which are closely related to the β decay: neutrino or antineutrino capture by a nucleon also called *the inverse β decay*. Neutron rich nuclei decay by the β^- process. Whether the interaction is a Fermi (anti-parallel) or a Gamow-Teller (parallel) interaction is determined[10] by the relative orientation of the spins of the e^- and $\overline{\nu}_e$.

2.3.2 Classification of β transitions

β interactions can be characterized by the ft-value, which is the product of the half-life $t_{\frac{1}{2}}$ and the statistical function f which will be defined in (2.8):

$$ft = \frac{K}{G_V^2 B_F + G_A^2 B_{GT}}, \tag{2.5}$$

where the numerical constants are[16, 63]:

$$\frac{K}{G_V^2} = 6141 \pm 4 \ s \ , \tag{2.6}$$

and

$$\left(\frac{G_A}{G_V}\right)^2 = 1.59 \pm 0.01 \ . \tag{2.7}$$

B_F and B_{GT} are the Fermi and the Gamow-Teller matrix elements, respectively. The magnitude of the matrix elements depends on the overlap of the wave functions of the initial and the final states in the transition. A small change of angular momentum results in a large transition probability. Super-allowed decays are normally decays where there is no change in spin and isospin and a conservation of parity, in other words a Fermi transition[10]. Allowed transitions involve a change of spin of one unit, but no change of the angular momentum: $\Delta I = 0, \pm 1$, $\Delta T = 0, \pm 1$ and no parity change. Gamow-Teller decays satisfy these selection rules. One can also define the super-allowed transitions in a more quantitative way by demanding $log(ft) < 4$[69]. This demand implies the existence of super-allowed Gamow-Teller transitions. The β transitions of neutron rich light nuclei are Gamow-Teller transitions, but they can involve very large transition rates, which sometimes leads to the naming *super-allowed* even though they by strict definition only are *allowed* transitions.

2.3.3 The statistical rate function

The statistical rate function f for a β decay may be written as[59, 60]:

$$f = \int_1^{W_0} F(Z,E)E\sqrt{(E^2-1)}(E_0 - E)^2 dE \ , \tag{2.8}$$

where the energy E of the fed level in the daughter nucleus and the momentum p are measured in absolute units. In the limit of small Z (no Coulomb field) the Fermi function F becomes unity, and (2.8) may be integrated by[67]:

$$\begin{aligned} f_{Z=0} &= \int_1^{W_0} \sqrt{E(E^2-1)}(E_0 - E)^2 dE \\ &= \frac{1}{60}(2W_0^4 - 9W_0^2 - 8)p_0 + \frac{1}{4}W_0 ln(W_0 + p_0) \ , \end{aligned} \tag{2.9}$$

where the total β particle energy W is:

$$W = \frac{Q - E}{m_e} + 1 \,, \tag{2.10}$$

with end point W_0 and the corresponding maximum momentum:

$$p_0 = \sqrt{W_0^2 - 1} \,. \tag{2.11}$$

m_e is the electron mass in units of keV and Z is the nuclear charge.

2.3.4 The β decay of ^{11}Li

The ^{11}Li nucleus has a very large β decay Q-value of 20.68 MeV[1] which opens a large number of β delayed decay channels. These channels are listed in table 2.2 together with the energy windows $Q - S_X$.

Particle X (References)	β^- decay of ^{11}Li	$Q - S_X$ (MeV)	Reference
d	$^{11}Li \rightarrow {}^{11}Be^* \rightarrow d + {}^{9}Li$	2.70	[49]
t	$^{11}Li \rightarrow {}^{11}Be^* \rightarrow t + {}^{8}Li$	4.90	[43]
α	$^{11}Li \rightarrow {}^{11}Be^* \rightarrow \alpha + {}^{7}Li$	12.37	[44]
n	$^{11}Li \rightarrow {}^{11}Be^* \rightarrow n + {}^{10}Be$	20.23	[58]
2n	$^{11}Li \rightarrow {}^{11}Be^* \rightarrow 2n + {}^{9}Be$	13.41	[8]
3n	$^{11}Li \rightarrow {}^{11}Be^* \rightarrow 3n + 2\alpha$	11.75	[7]

Table 2.2: Experimental observed β delayed particles from the decay of Li. Q is the Q-value of the β decay and S_X is the separation energy of the particle X from the daughter nucleus.

2.3.4.1 The β delayed γ emission

The γ decay of the daughter nuclei from the β decay of ^{11}Li is shown in figure 2.5. The 320 keV transition is as earlier explained one of the fastest nuclear decays known today, and it is believed[64] that this transition can contribute to further understanding of the halo properties of ^{11}Be. The branching ratios of the displayed γ lines have all been determined earlier by C. Détraz *et al.*[27] in 1980. Additionally T. Björnstad *et al.*[12] have measured the branching ratios for the 320 $\rightarrow$ 0 keV transition in ^{11}Be and the 3368 $\rightarrow$ 0 keV in ^{10}Be. The results from these two experiments together with a comparison with the

values obtained in our experiment can be seen in Chapter 4. It should be noted that the γ transitions in ^{10}Be are Doppler shifted due to the neutron emission from the parent nucleus ^{11}Be. The extent of these shifts depends on the life times of the various states, because if the life time of a given state is relative long then will the ^{10}Be nucleus lie still and no shift will be observed.

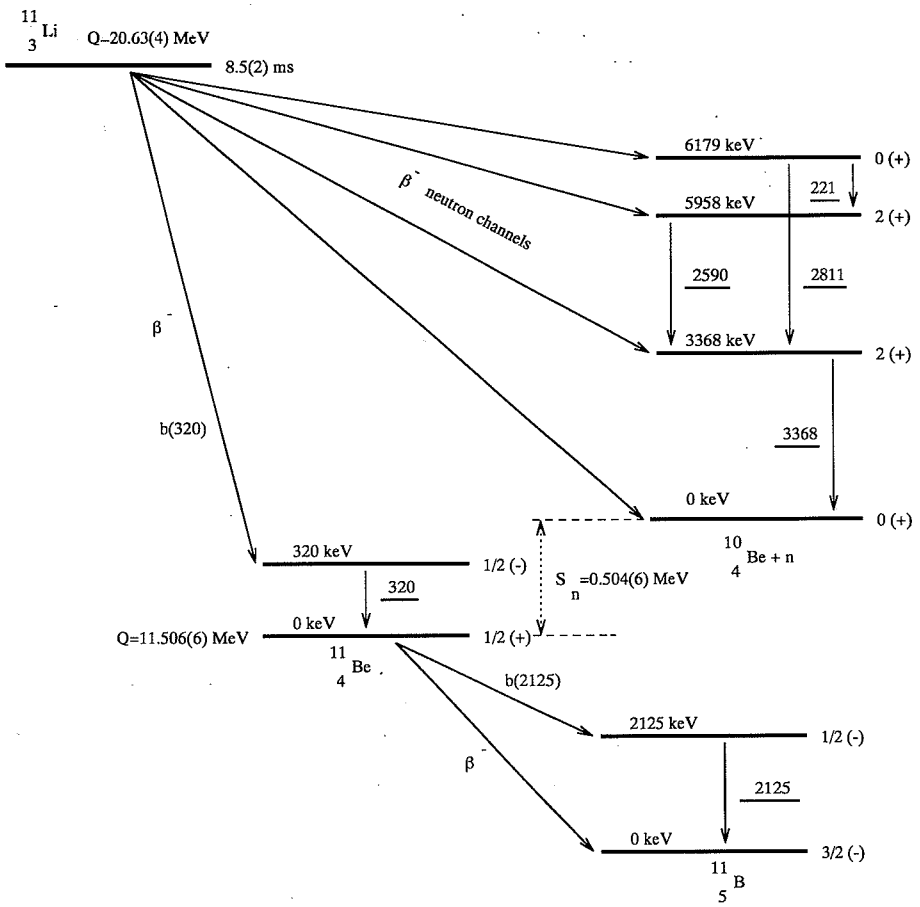

Figure 2.5: The γ decay scheme of ^{11}Li.

2.3.4.2 The β delayed neutron emission

As seen in table 2.2 both one, two and three neutron emission[38] from the excited states of ^{11}Be is very likely, but the analysis of the experiment discussed in Chapter 5 only investigates one-neutron emission channels. Some

of the possible one-neutron emission channels are shown in figure 2.6. The interpretation of the results from the one-neutron part of the experiment is strongly depended on the γ transitions from the highly excited states of ^{10}Be. This fact will be discussed in more detail in Chapter 5, but the γ results has in principle a very valuable normalization function in the interpretation of the obtained neutron data.

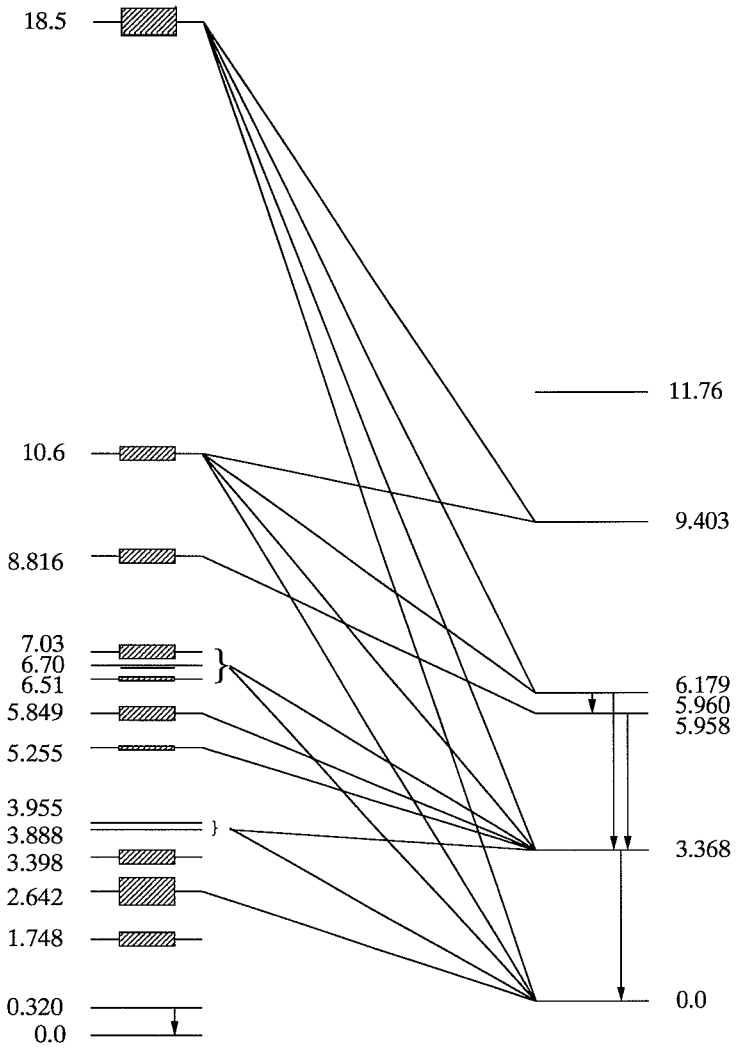

Figure 2.6: Some possible one-neutron emission channels.

Chapter 3

Experimental tools

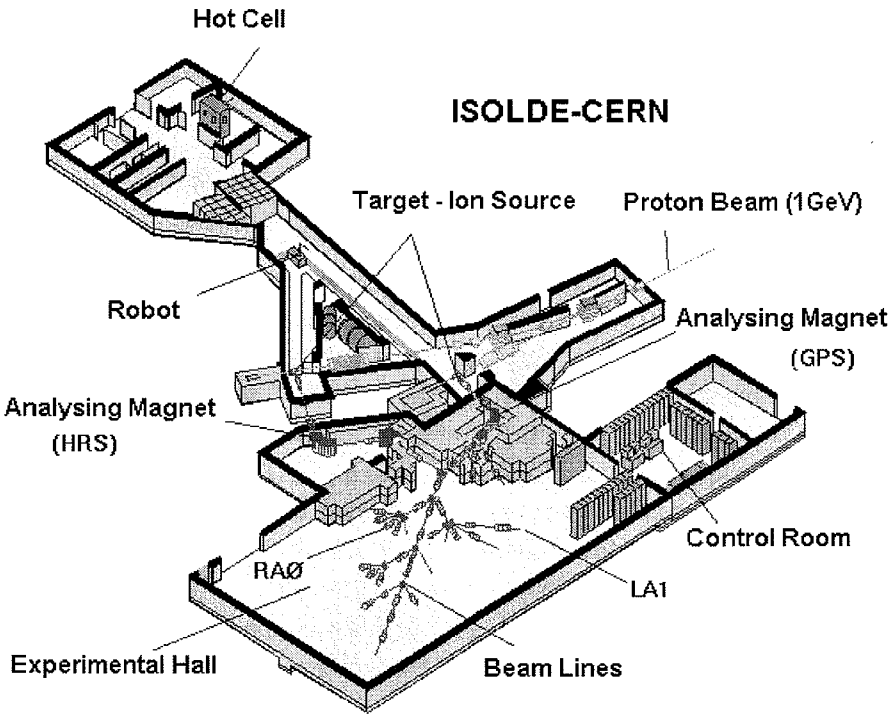

Figure 3.1: The nuclear experimental facility ISOLDE at CERN, Geneva in Switzerland with the applied beam lines indicated as RAØ and LA1.

3.1 Experimental facilities at ISOLDE

The ISOLDE facility[2, 39] at CERN in its present version was taken into use for the first time in the spring 1992. A 3-dimensional view of ISOLDE is shown in figure 3.1. ISOLDE is situated near and connected with the CERN Proton-Synchrotron Booster (CPSB) via an underground transfer line. The CPSB consists of a stack of four small synchrotrons which accelerates protons, preaccelerated by a linear accelerator, every 1.2 s. The protons which either can be directed to the CERN Proton-Synchrotron (CPS) or to ISOLDE are delivered in very short pulses of about 2.4 μs with a high intensity. The CPS delivers protons to the high energy facilities at CERN. The proton pulses from the CPSB are divided into supercycles lasting 14.4 s which again are divided into 12 subcycles lasting 1.2 s. These subcycles can be distributed to both the CPS and ISOLDE. The experiment discussed in Chapter 4 and 5 was supplied with 7 subcycles during each supercycle. The pulse numbers were 4, 6, 8, 9, 10, 11, 12. This structure was perfect for ^{11}Li which as earlier mentioned has a half-life of circa 8 ms, and one subcycle lasts well above 100 half-lives. The activity from the fast decay of ^{11}Li could therefore easily be measured within each subcycle. The maximum intensity of protons in each subcycle is about $3.2{\cdot}10^{13}$ protons/pulse[42], and during our experiment is was about $2.7{\cdot}10^{13}$ protons/pulse.

3.1.1 The targets

The different targets which are in a highly radioactive area are changed, stored and removed by an industrial robot. The targets not in use are stored on shelves, and it is possible to park the robot, which goes on rails, outside the radioactive zone to be able to safely do repair jobs. The protons are traveling the last few meters in air before hitting the target. This is done so the robot can find space to handle the targets. The highly radioactive zone is in addition of steel and concrete shielding blocks around the ISOLDE targets also buried under up to 8 m of earth. The ventilation system is specially designed to ensure that radioactive contamination is kept within the confined area in case of e.g. leaking targets. This should later show not to be completely true (see Section 4.3.3). The produced nuclei are transfered by molecular flow in vacuum into the ion source via a tubular line. There exist various ion sources for the ISOLDE facility, but the one used in the experiment discussed in Chapter 4 and 5 was made of a small tube of Tungsten (W). When the atoms from the target drift through the tube the relatively high electronegativity of 2.36 of W[22, page 62] causes one electron per passing atom to be stripped off to create ions. These ions are then accelerated by a 60 kV voltage drop before

entering the mass separators. The power supply providing the acceleration voltage is constructed in such a way that about 35 μs[39] before the protons hit the target it is turned off and turned on again after the 2.4 μs beam pulse. This is done because when the protons hit the target the surrounding air will be ionized and cause the power supply to break down if not turned off. After 5 ms the voltage is back at 60 kV within a ripple of 1 V.

3.1.2 The mass separators

ISOLDE has two on-line mass-separators: the General Purpose Separator (GPS) and the High Resolution Separator (HRS). GPS is of the same type of machine as used at the old ISOLDE-2[13] and HRS is essentially a slightly modified ISOLDE-3[13] separator. The HRS was not ready for use until December 1995. The GPS was used in the experiment IS320 analyzed in Chapter 4 and 5. The mass resolution of the GPS is $\frac{M}{\Delta M} = 2400$ or about 0.5 % for mass 11. When leaving the GPS the ions are passed trough a "switch-yard", which by electrostatic deflectors can switch the beam down the desired beam line.

3.2 Detectors

The choice of detector can be quite crucial for the expected results of a given experiment. Some detector types work best at some specific ranges of energies or count rates, and some detectors have better resolution than others. One has to consider carefully what one wants to measure and how, and then select the most adequate detector for this purpose. In the following subsections different particle detectors will be described. Most importance has been attached to detector types used in the experiment IS320.

3.2.1 γ detectors

The γ rays were discovered in 1900 when Villard[24, Chapter 1] observed that radiation from the natural activity discovered by Becquerel(see figure 1.1) included a component whose flight path was not bent in a magnetic field as the earlier discovered α and β rays. These observations were done by the help of photographic plates, which were very troublesome and time consuming. After irradiation the plates had to be developed before any physical result could be obtained. Soon the more-easy-to-handle gas filled counters were used because they also provided a quantitative measurement of the radiation present. The mechanism for detection with the gas filled detectors was the photoelectric

effect, where the secondary electrons had to be stopped within the gas volume to ensure proportionality. This requirement caused only detection of γ-rays with energies low enough to only interact through the photoelectric effect. This kind of detectors were mainly used to determine the number of events occurring in the detector, and not the energy of of the photons involved. When Hofstadter[34] around 1948 introduced the NaI(Tl) detectors a major improvement was done. They allowed measurement of energy spectra over a wide range of energies. After a short period of development it was possible to produce NaI detectors with sufficiently large crystals to ensure a high absorption rate for photons with energies up to approximately 1 MeV. The resolution was circa 7 % , which means a FWHM[1] of 45 keV for a 662 keV γ line from ^{137}Cs. Even though the NaI detectors now provided energy spectra over a large range of energies the question of whether an ionization chamber could be made from a high-density material was still there. This led to the construction of the Ge(Li) detector by among others E. M. Pell[53] in 1962.

The germanium crystal in the detector is a semiconductor whose outer shell atomic levels exhibit an *energy band structure* which is shown in figure 3.2. For comparison also the energy band structures of insulators and metals are shown. The *energy bands* are regions of many discrete levels which are

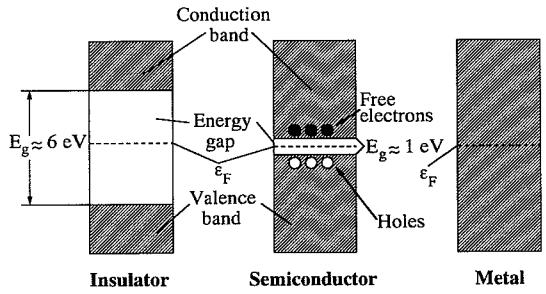

Figure 3.2: Energy band structure of insulators, semiconductors and conductors.

so closely spaced that they may be considered as a continuum, while the *forbidden* energy gap is a region in which there are no available energy levels at all. The band structure arises from the periodic arrangement of the atoms in the crystal, which causes an overlapping of the electron wavefunctions. The Pauli principle forbids more than one electron in the same state, which implies the degeneracy of the outer atomic levels to break up and form many discrete levels only slightly separated. Two electrons with opposite spin may reside in

[1]See Appendix C.2 for the definition of FWHM

the same level, and the number of levels is therefore the same as the number of electron pairs in the crystal. The highest energy band is the conduction band, and electrons belonging to this band are detached from their parent atoms and free to move around in the crystal. The electrons in the valence band are more tightly bound and will keep to their respective lattice atoms. The width of the energy gap is dependent on the spacing of the lattice atoms, and

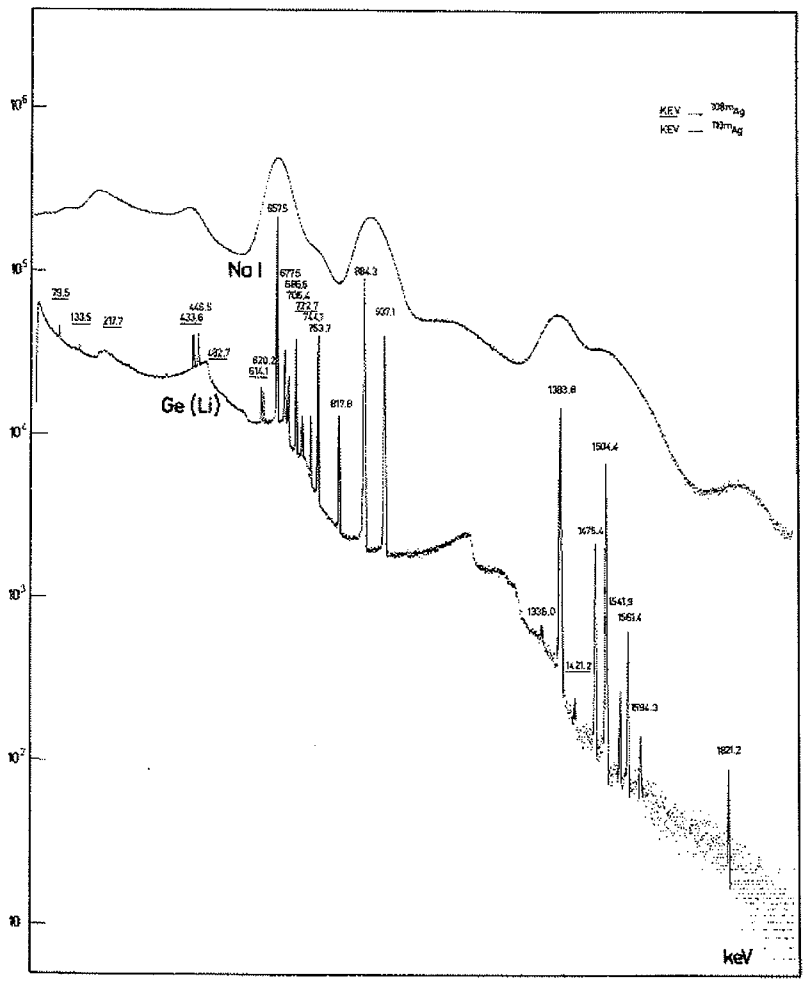

Figure 3.3: Comparative height spectra recorded using a NaI and a Ge(Li) detector. The source was γ radiation from the decay of ^{108m}Ag and ^{110m}Ag. Energies of the peaks are labeled in keV. Taken form reference [40, page 399] (originally from reference [54]).

therefore also dependent on the temperature and pressure. At normal temperatures all electrons in an insulator reside in the valence band and thermal energy is not enough to excite them to the conductor band. When an external electric field is applied there is consequently no flow of charge and therefore no current. For conductors this is totally opposite. In semiconductors the energy gap is smaller than for insulators, and a small current will therefore be observed when an electric field is applied at normal temperatures. When cooling the crystal down all electrons will fall into the valence band and the conductivity will decrease. One can increase the conductivity of the semiconductor by doping it with impurity atoms. All crystals contain some natural impurity atoms which are called either *donors* or *acceptors* depending on their mode of operation[5]. The typical impurity concentrations are of the order of 10^{13} atoms/cm^3 and the density of germanium in the crystals are of the order 10^{22} atoms/cm^3 (approximately concentrations of impurity atoms of a few parts per billion). If the number of *donors* and *acceptors* including the additional doped impurities are equal then a cancelation will occur. The very important discovery of Pell in the 1960's was that when adding lithium the impurification result could be controlled, i.e. the type of semiconductor, and better conductivity could be obtained. This technique is called *compensating*. Even though the efficiency hereby was increased, it was still much lower than the efficiency for NaI detectors. However the new germanium detectors offered very good energy resolutions with FWHM of about 1 keV for the 662 keV γ line from ^{137}Cs. One had by this new detector gained a very good spectroscopic tool for very precise energy determination. A comparison of the resolution of a NaI and a Ge detector is shown in figure 3.3. The two spectra illustrates the very large difference of the resolution. The spectrum for the NaI consists of large bulks where the spectrum of the Ge detector also include the narrow peaks from the γ ray transitions. Even though the NaI suffers of a very bad energy resolution, it is not totally outdated yet. The time signals from this type of detector are usually much faster than the signals from the Ge detectors, and is therefore often used in experiments requiring fast timing. The Ge(Li) detectors have become somewhat old fashioned, and the new *High Purity* germanium detectors have been applied to a greater extent recently.

3.2.2 Neutron detectors

There exist a large variety of types of neutron detectors with special properties suitable for different kinds of experiments[40, Chapter 15]. Some detectors are made of solid scintillators, e.g. the LAND detector which is divided into sections allowing experiments involving position determination[35, 62], and some use liquid scintillator material. The following discussion will only deal

with this type of neutron detectors.

Like the γ rays neutrons are neutral and can therefore not interact via the Coulomb force. A nuclear interaction is consequently necessary where the energy of the neutron is converted into energy of the charged particles in the scintillator material. Every type of neutron detector involves this conversion of energy. Because of the short range of the strong nuclear force the interaction probability is small and neutrons are therefore difficult to detect. The different materials used for the conversion of neutron energy to charged particles provides various neutron capture reactions depending on the energy of the neutrons. For slow and epithermal neutrons ($E_{neutron} \simeq \frac{1}{40}$ eV - 100 keV) the following neutron capture reactions are most often used: (n,γ), (n,p), (n,α) and (n,f). For fast neutrons ($E_{neutron} \simeq$ 100 keV - 100 MeV) elastic scattering A(n,n)A dominates. If the neutrons have energies beyond approximately 1 MeV also inelastic scattering, i.e. A(n,n')A* and A(n,xn')B, may occur by excitation of the nuclei in the detector material. For very high neutron energies (more than 100 MeV) hadron showers can occur.

Fast neutrons are normally detected by a combination of elastic and inelastic scattering against the atoms in the detector material. It can be shown[45, Section 2.8.1] that the energy of a fast neutron, with an initial en-

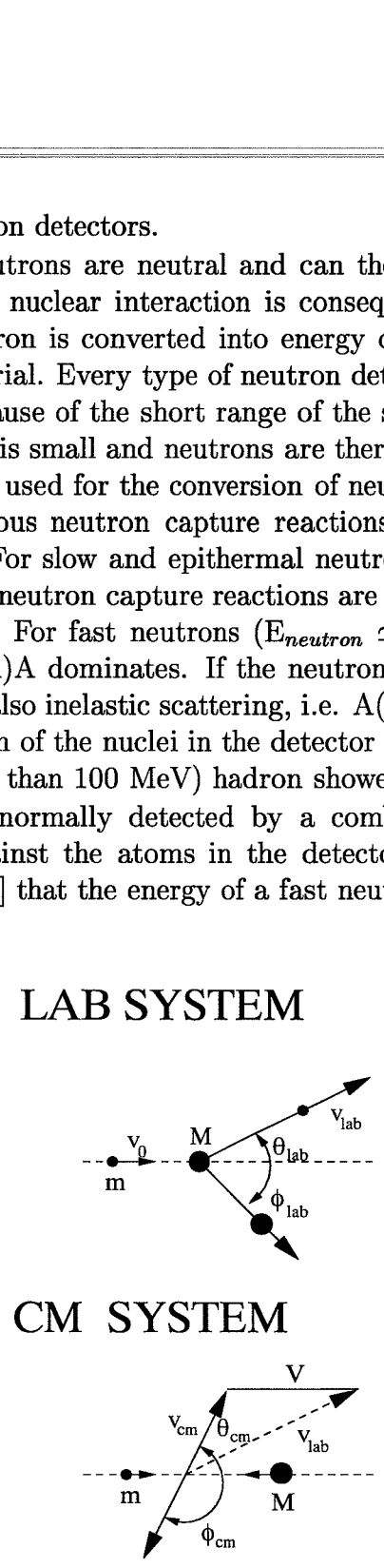

Figure 3.4: Elastic scattering of a neutron on a nucleus with mass M. In the calculation of equation (3.1) the masses m = 1 and M = A.

ergy E_0 scattering on the detector material with atomic mass A, is limited by the following equation (see figure 3.4):

$$\left(\frac{A-1}{A+1}\right)^2 E_0 < E < E_0 \tag{3.1}$$

where the limits correspond to scattering at $cos\theta_{cm} = \pm 1$. In the particular case of scattering on protons, $A = 1$ and:

$$0 < E < E_0 \tag{3.2}$$

This means that neutrons scattering on protons can be stopped totally. This is due to the fact that lighter nuclei absorb more recoil energy from the neutron than heavy nuclei. This is also the explanation of the choice of hydrogenous materials such as water or paraffin (CH_2) as neutron moderators (nuclear power plants) and shielding.

The neutron detectors used in the experiment discussed in Chapter 5 consist of a scintillator material called NE213. NE213 is an organic liquid and mainly used for experiments where detection of fast neutrons with Pulse Shape Discrimination against γ rays (see Section 3.2.2.2) should be applied[40, Chapter 8].

3.2.2.1 The response function

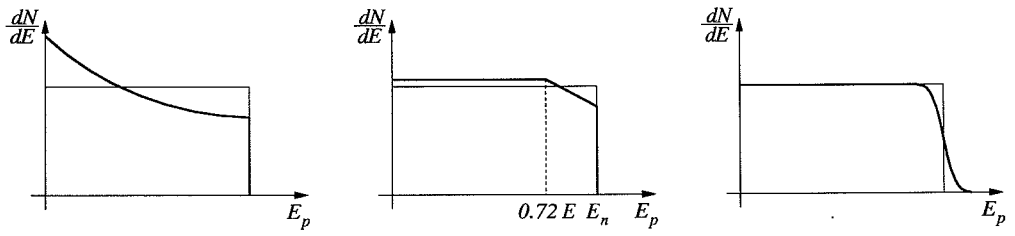

(a) Scintillator nonlinearity

(b) Carbon scattering

(c) Finite resolution

Figure 3.5: Distortion to the rectangular recoil proton energy spectrum, due to three separate factors. Taken from [40, page 540].

The ideal response function for detection of mono-energetic neutrons scattering on the protons in the organic scintillator material is a square function.

When using small detectors the response function will be very close to this square function, because neutrons entering the detector will most likely only scatter once and then leave the detector again. Unless the dimensions of the scintillator are less than a few millimeters, the protons will not escape the surface. When the dimensions increase, the neutrons will perform multiple scatterings and the response function will differ from the square function. Most organic scintillators exhibit nonlinearly light output as a function of the deposited energy. This effect raises the response function for small proton recoil energies (see figure 3.5a). All organic scintillators contain carbon as well as hydrogen. Because of the more narrow energy range (3.1) of the elastic scattered neutrons on carbon, the carbon recoils do not directly contribute much to the detector output. But since the neutrons, which scatter on the carbon atoms, will loose some of their initial energy before they scatter on the protons, they will not produce an energy spectrum with the same level of energy as unscattered neutrons. Incident neutrons can loose from 0% to 28% of their initial energy (see figure 3.5b). The last distortion is the finite resolution of the detector. Non-uniform light collection, photoelectron statistics and other sources of noise tend to wash out some of structure around the maximum neutron energy (see figure 3.5c). In real experiments there will not only be mono-energetic neutrons, but several different initial neutron energies coming from different decay modes. They will add up to a distribution of neutron energies ranging from the lower threshold of the detector to the maximum energy of the incident neutrons. An example of a real neutron

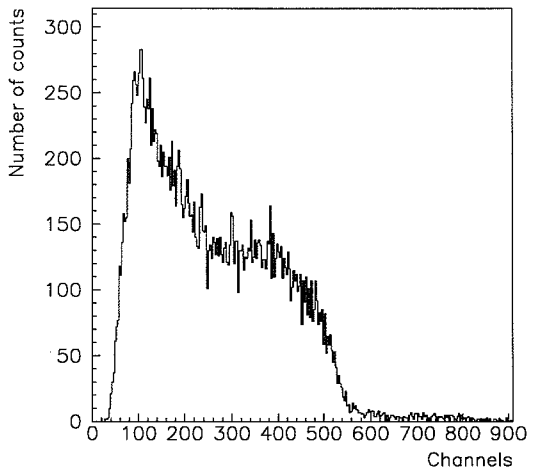

Figure 3.6: Typical neutron amplitude spectrum.

spectrum is shown in figure 3.6.

3.2.2.2 Pulse Shape Discrimination

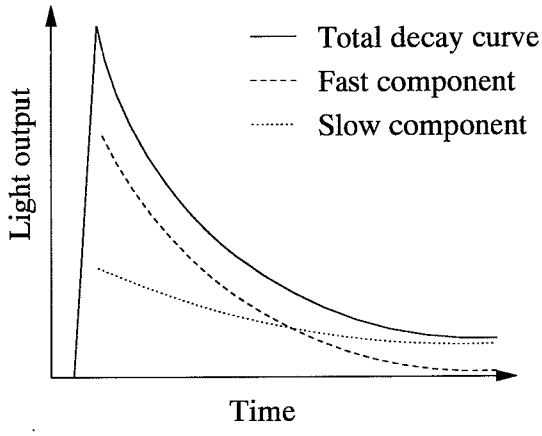

Figure 3.7: Resolving scintillation light into *fast* (prompt) and *slow* (delayed) components. The *solid* line represents the total exponential light decay.

Neutron detectors do not only detect neutrons, but are also sensitive to γ rays. To distinguish between these rays and the neutrons special scintillator material, which provides different shapes of the output pulses from the detector, has to be used. This applied technique is called Pulse Shape Discrimination (PSD), and it can be used with both organic scintillators and some inorganic crystals. The cause of this possible filtration is the excitation of different fluorescence mechanisms by particles of different ionizing power. Scintillator materials exhibit this property known as *luminescence*, which means that when the material is exposed to radiation, it absorbs and reemits

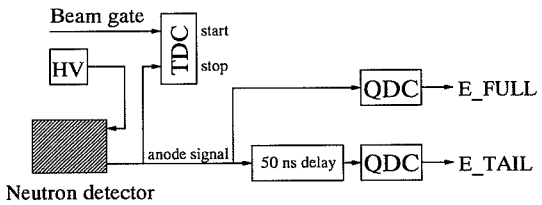

Figure 3.8: Schematic overview of PSD setup.

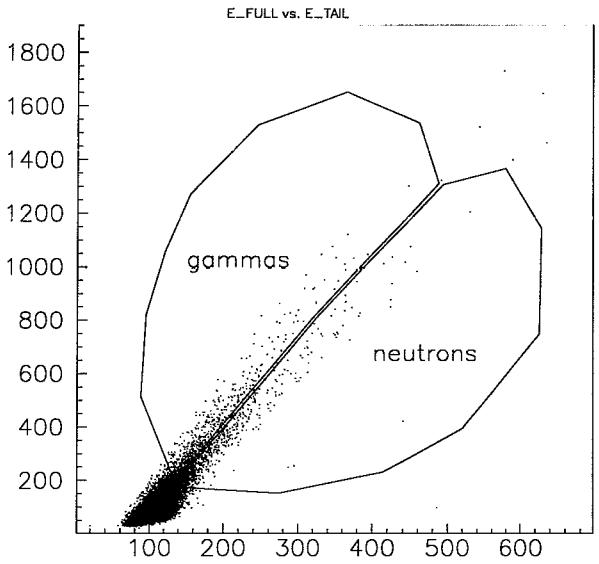

Figure 3.9: An example of a Pulse Shape Discrimination with the selective graphical cuts indicated.

the energy in the form of visible light. If the reemission occurs within 10^{-8} s this process is called *fluorescence*. If the reemission is delayed, however, it is called *phosphorescence*. This happens if the excited state is metastable, and the delaytime can be from a few microseconds to several hours depending on the material. For most scintillators one component of the light output is generally much faster than the other. The two components originating from the neutron and γ interactions with the scintillator material are designated as the *fast* and *slow* components, respectively. These components are shown in figure 3.7 together with the total light output decay. A schematic overview of a PSD setup[23, 60] is presented in figure 3.8. The electronic modules are briefly discussed in Section 3.3.5. As it will be explained in Chapter 5 the PSD method did not function well for all detectors and a Time Of Flight calibration was used instead for discrimination of the γ rays and the neutrons (Section 5.3.3).

3.2.3 β detectors

Detection of β particles (electrons) depend very much on the scintillator material of the applied detector. Nearly all electrons entering the scintillator will result in detectable signals, only very few will fail to do so. But because of the

low mass of the electron, it can undergo large angle scatterings in matter. This can result in backscattering or side scattering of the incident electron, and it can during this process accidently escape the scintillator material before it has deposited all its energy. Obtaining satisfactory energy measurements under these conditions can be quite difficult. The backscattering effect depends strongly on the atomic number of the scintillator material, and it increases rapidly with increasing proton number Z. Organic scintillators have proved to be the most convenient scintillator material for ordinary electron energies, due to the low effective proton number Z. The intrinsic efficiency of these detectors are normally considered as 100%. For very high electron energies the use of inorganic materials can be preferable. High energy electrons will mainly loose their energy by the production of bremsstrahlung. This effect can be reduced by using high Z materials, due to their high density and atomic number. Detectors made of plastic are often used for β particle detection. It is an organic material which can be produce in many various forms and shapes. The detector used in the experiment IS320 will be treated in Section 4.2 and 5.2. The energy spectrum of electrons originating from a β decay

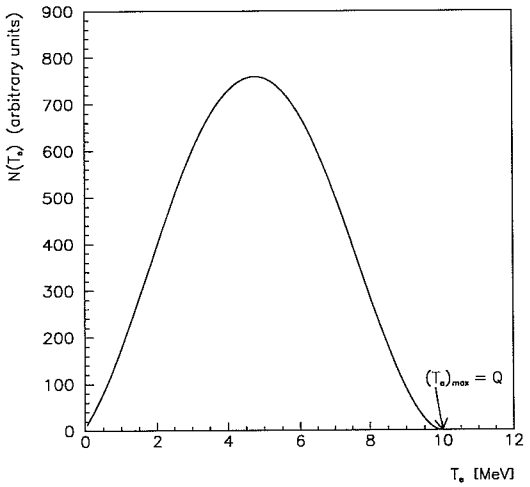

Figure 3.10: Expected electron energy distribution for Q = 10 MeV.

can, when assuming low Z and high energy (no Coulomb), be calculated to be[41, Chapter 9]:

$$N(T_e) \propto \sqrt{T_e^2 + 2T_e m_e c^2}\,(Q - T_e)^2 \left(T_e + m_e c^2\right) , \qquad (3.3)$$

where $N(T_e)$ is the distribution of the electron energies in arbitrary units, T_e is the kinetic energy of the electron, m_e the electron mass and Q is the energy

released in the β decay. The distribution of the electron energies for $Q = 10$ MeV is plotted in figure 3.10. The actual spectrum the β detector may differ from the figure, due to the lower threshold provided by the electronics and the detector itself.

3.2.4 Gas telescopes

In the experimental setup for the neutron experiment a gas telescope[50] also figures. The telescope was not used in the neutron analysis in Chapter 5, but the analysis results are published in our article in reference [49]. Gas telescopes are used for particle identification which is done by the use of a gas detector combinated by a silicon detector. The particles entering the telescope looses a small fraction ΔE of their energy by ionization of the gas (here freon). Then they hit the silicon detector which is thick enough to stop the particles totally and determine their kinetic energy E. When plotting ΔE versus E one will get a plot of different curves for different charges and masses of the incident particles. Consequently it is possible to identify the particles as long as the resolution of the detector allows it.

3.2.5 Detector efficiency

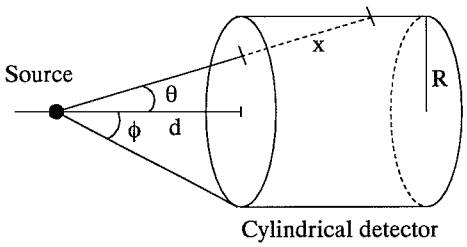

Figure 3.11: Sketch of a detector.

The absolute or total efficiency of a detector is defined[45, Chapter 5] by the fraction of events emitted by the "source" which is actually registered by the detector:

$$\varepsilon_{total} = \frac{\text{events registrered}}{\text{events emitted by the "source"}} . \tag{3.4}$$

As an example, a cylindrical detector with a point source at a distance d on the detector axis is considered (see figure 3.11). The probability of a

"particle" being emitted at an angle θ is, when isotropically radiation is assumed, defined by:

$$P(\theta)d\Omega = \frac{d\Omega}{4\pi} . \tag{3.5}$$

and the probability that a "particle" hitting the detector will interact with the detector material is:

$$P(x) = 1 - e^{-\frac{x}{\lambda}} . \tag{3.6}$$

Combining (3.5) and (3.6) gives:

$$d\varepsilon_{tot} = \left[1 - e^{-\frac{x}{\lambda}}\right] \frac{d\Omega}{4\pi} , \tag{3.7}$$

where x is the path length in the detector and λ is the mean free path for an interaction. The total efficiency can then be found by integrating (3.7) over the volume of the detector. Often x does not vary too much over the detector volume or the mean free path λ is so small that the exponential in (3.7) can be considered as zero. The total efficiency ε_{total} can then be factored into an intrinsic efficiency ε_{int} and a geometrical efficiency ε_{geom} also called *acceptance*:

$$\varepsilon_{total} \simeq \varepsilon_{int} \cdot \varepsilon_{geom} . \tag{3.8}$$

The intrinsic efficiency ε_{int} is the fraction of events actually hitting the detector which is registered:

$$\varepsilon_{int} = \frac{\text{events registrered}}{\text{events impining on the detector}} . \tag{3.9}$$

This fraction depends on the interaction cross sections of the incident radiation on the detector medium and is therefore a function of the type of radiation, its energy and the detector material. The intrinsic efficiency ε_{int} for charged particles is generally good for most detector types, because charged particles very rare do not produce some sort of ionization. For heavier particles quenching effects can be present and the ionization rate is reduced. The efficiency of a detector is often more varying for neutral particles than charged particles , due to the fact that they must first interact to create secondary charged particles. These interactions are much more rare than direct interaction and a good detection of the fraction of the incident neutral radiation is often not possible. In this situation the detector dimensions can become very important to provide a sufficient amount of detector material to get a good probability of interaction.

The geometrical efficiency ε_{geom} is the fraction of the source radiation which is geometrically intercepted by the detector. It therefore only depends on the geometrical configuration of the source and detector, i.e. the solid angle. The solid angle Ω for a detector (for example the cylindrical detector in figure 3.11) is calculated by:

$$\Omega = \frac{1 - cos\theta}{2}, \tag{3.10}$$

and

$$\tan\theta = \frac{R}{d}. \tag{3.11}$$

R is the radius of the detector and d is the distance from the source to the surface of the active volume of the detector.

3.3 Data acquisition and electronics

The amount of different electronic modules used in experiments is huge. The different properties and possibilities for use belong to a jungle of knowledge. I have in the following included descriptions of a few, but basic modules and standards.

3.3.1 The NIM standard

The *Nuclear Instrument Module* (NIM) system is designed for small-scale linear pulse processing normally encountered in the routine application of radiation detectors. The modules fit into the standard relay rack with a maximum of 12 modules. Each of the 12 bin locations are provided with a 42 pin connector that mates with the corresponding connectors on the back of the modules. The primary means of transmitting linear and logic pulses between the NIM modules is by coaxial cables connected to either the back or the front panel of the modules by BNC connectors. The NIM standard also includes logic signal levels which are shown in table 3.1[40, Appendix A].

3.3.2 The CAMAC standard

The *Computer Automated Measurement and Control* standard is based on a crate, which is subdivided into 25 individual module stations. Electrical connection between each module and the crate is made by a printed circuit board edge connector with 86 contacts. Within the crate, each connector provides

	Output (must deliver)	Input (must respond to)
NIM Standard Logic Levels		
logic 1	+4 to +12 V	+3 to +12 V
logic 0	+1 to -2 V	+1.5 to -2 V
NIM Fast Logic Levels for 50 Ω Systems		
logic 1	-14 to -18 mA	-12 to 36 mA
logic 0	-1 to +1 mA	-4 to +20 mA

Table 3.1: NIM Standards.

access to the *dataway*, which is a data highway consisting of busses for digital data, control signals and power. The digital communication between the modules within a crate occurs over this dataway. It replaces external interconnection of modules for many digital functions. Still, however, coaxial cable connections must be retained for linear signals etc. These signals can be coupled to either the front or back of a module using a special connector. The extreme right-hand station in the crate is called the *control station*. Here is the double width *crate controller* module located. This module control all necessary data transfer between the modules in the crate and works as an interface to the external computer handling the data acquisition. The CAMAC system cannot function without the controller. The data acquisition program must know how to handle the internal coding and indexing of the individual modules. The modules cannot communicate directly with each other, but need to "talk" with the crate controller first. The controller uses a coded subaddress and function, which should be provided by the main acquisition program on the external computer.

3.3.3 TTL and ECL logic signals

	TTL [V]	ECL [V]
Logic 1	2-5	-1.75
Logic 0	0-0.8	-0.90

Table 3.2: TTL and ECL signal levels.

While not part of the NIM or CAMAC standard two other logic families are often used in modern nuclear physics electronics. The first is the *Transistor Transistor Logic* family. This is a positive logic signal which is very often found on NIM modules. The second is a logic family which is becoming increasingly popular in many-parameter physics experiments. This is the *Emitter Coupled Logic* which is currently the fastest form of digital logic available. The levels for these two logic families can be viewed in table 3.2. ECL modules are very often high density modules due to the high impedance of 100 Ω which allows the use of space-saving twisted pair and flat ribbon cables instead of the usual coaxial cables with BNC connectors.

3.3.4 Gsi Online Offline S Ystem

GOOSY[29] is a data acquisition program developed at the *Gesellschaft für Schwerionenforschung* (GSI) in Darmstadt, Germany. It is acquiring data from the CAMAC system via an *ethernet* connection and storing the data in an event database. The contents can viewed and analyzed online while storing the data on tape. The platform is VMS for VAX/AXP computers.

3.3.5 Various electronic modules

The main problem within physics experiments today is to convert the analog signals from the detectors to digital signals which then later can be analyzed and interpreted by the use of computers. This is done by an innumerable number of electronic modules, some commercial fabricated and some made especially for certain experiments. In the following some basic information on the different module types will be presented.

3.3.5.1 ADC

Analog to Digital Converters are the most fundamental instruments in the link between analog and digital electronics. The ADC's can be divided in two main types: *peak-sensing* and *charge sensitive.* The former is used for digitizing a maximum voltage signal and the latter is used for digitizing the total integrated current. Peak-sensing ADC's are used with slow signals which has already been integrated. Charge-sensitive ADC's, on the other hand, are used with current-generating devices such as fast detectors. The ADC has an allowed range of input signals which are converted into digital signals. The more bits available in this conversion the better the resolution of the digital signals.

3.3.5.2 TAC

The *Time to Amplitude Converter* provides a possibility of converting a time interval into an analog signal whose amplitude corresponds to the length of time interval. This is done by supplying a logic START signal to the TAC, which then starts the discharging of a capacitor. The discharging is stopped by a logic STOP signal. The amount of charge discharged from the capacitor is then converted into an analog signal which corresponds to the space of time between the START and STOP signals. It is possible on most modules to control the time window in which the START and STOP signals should be.

3.3.5.3 TDC

The *Time to Digital Converter* is actual a TAC and an ADC combined. The output of the TAC is digitized by the ADC. The TDC module is made to provide better counting techniques and stable oscillators. The module, however, is operated in the same way as the TAC and ADC.

3.3.5.4 CFD

The *Constant Fraction Discriminator* is a device which always triggers at the optimum constant fraction of the pulse height for nearly any pulse type. The pulse shaping employed in a constant-fraction timing discriminator is done by first splitting the negative input signal into two parts. One part is attenuated to a fraction f of the original amplitude, and the other part is delayed and interverted. These two signals are subsequently added to form a constant-fraction timing signal. The delay is chosen to make the optimum fraction point on the leading edge of the delayed pulse line up with the peak amplitude of the attenuated pulse. Consequently, adding the two signals yields a bipolar signal with a zero-crossing that corresponds to the original point of optimum fraction on the delayed signal. Additionally, the zero-crossing will be independent of the pulse amplitude. CFD's are very often used in coincidence setups and for PSD.

3.3.5.5 TFA

The *Timing Filter Amplifier* is used for shaping pulses and optimizing the signal-to-noise ratio for timing measurements. Very often the TFA is used together with the CFD in timing applications with germanium or silicon charged-particle detectors. It provides the possibility of control of the rise time and amplification of the detector signal obtained directly from the preamplifier output.

3.4 Analysis tools

Modern nuclear experiments often involve huge amounts of data. This results in the necessity of the use of computers to handle all these data. Combined with statistical tools they provide a very powerful implement to extract the physical results. In the following the *chi-square* distribution, which many physicists use for fitting their data, will be discussed. Also some different tools for fitting the obtained spectra will be explained.

3.4.1 The χ^2 distribution

The *chi-square* distribution is particularly useful for testing the *goodness-of-fit* of theoretical formulae to experimental data, and it is very popular by a lot of physicists all around the World for data analysis. One should, however, be aware of the danger[36] when having low statistics. In that case one should turn to the *Maximum Likelihood Method* instead. This turned out to be no problem in the analysis in Chapter 4, and the χ^2 distribution was therefore used in all fits performed in the analysis of the β delayed γ emission. The distribution is defined[45, Chapter 4] as follows. If a set of n independent random variables x_i is considered, and it is assumed that they are distributed as Gaussian densities with theoretical means μ_i and standard deviations σ_i respectively, then:

$$\chi^2 = \sum_{i=1}^{n} \left(\frac{x_i - \mu_i}{\sigma_i} \right)^2 , \tag{3.12}$$

is known as the *chi-square*. Since x_i is a random variable, χ^2 is a random variable as well, and it can be shown that it follows the distribution:

$$P(\chi^2) d\left(\chi^2\right) = \frac{\left(\frac{\chi^2}{2}\right)^{\left(\frac{\nu}{2}\right)-1} e^{-\frac{\chi^2}{2}}}{2\Gamma\left(\frac{\nu}{2}\right)} d\left(\chi^2\right) , \tag{3.13}$$

where ν is an integer and $\Gamma\left(\frac{\nu}{2}\right)$ is the *Gamma function*. ν is known as the *degrees of freedom* and it is the only parameter of the distribution. It therefore determines the shape of the distribution. ν can be interpreted as a parameter related to the number of independent variables in the sum (3.12). It can be shown that the mean and variance of (3.13) are:

$$\mu = \nu \tag{3.14}$$

$$\sigma^2 = 2\nu , \tag{3.15}$$

respectively. Each term in the sum (3.12), ignoring the exponent, can be interpreted as the deviation of x_i from its theoretical mean divided by its expected dispersion. χ^2 thus characterizes the fluctuations in the data x_i. By forming the χ^2 between the measured data and the assumed theoretical mean, a measure of the *reasonableness* of the fluctuations in the measured data about this hypothetical mean can be obtained. If an improbable χ^2 value is obtained, one must then begin questioning the theoretical parameters applied. The actual fit of the data involves a minimization of (3.12) (here written in a more general form allowing different types of fit functions):

$$S = \sum_{i=1}^{n} \left[\frac{y_i - f(x_i; a_j)}{\sigma_i} \right]^2 , \tag{3.16}$$

where $f(x; a_1, a_2, ..., a_m)$ is the desired fit function with $a_1, a_2, ..., a_m$ unknown parameters to be determined. When the minimum of (3.16) is reached an easy check can be done. Whether S is reasonable or not can be estimated by introducing the *reduced chi-square*:

$$\frac{\chi^2}{\nu} = \frac{S}{\nu} . \tag{3.17}$$

If the fit involves n independent data points from which m parameters are extracted, then the degrees of freedom is:

$$\nu = n - m . \tag{3.18}$$

If e.g. f is a linear function then $\nu = n - 2$. According to (3.14) which implies that the mean of χ^2 is equal to the degrees of freedom, (3.18) should be close to 1. A more rigorous test is to look at the probability of obtaining a χ^2 value greater than S, i.e. $P(\chi^2 \geq S)$. This can be done by integrating (3.13) or using cumulative distribution tables. The fit can be accepted in general if $P(\chi^2 \geq S)$ is greater than 5 %. On the other hand if S is very small carefulness is required.

3.4.2 Physics Analysis Workstation

The data from the ISOLDE experiment IS320 has been analyzed with the program *PAW*[18], which is a part of the *CERN Program Library*[19] of analysis tools. PAW works with two general types of data files: histogram files which are direct data files, i.e. there is no opportunities to make restrictions and combinations of the contents of the data files, and NTUPLE files, which are event based with possible cross references and combinations of the

parameters in each file. PAW can both be used interactively and in a kind of batch mode, where the PAW commands are stored in macro files called *kumac's*. These macro files have been used intensively in the analysis, because they provide an opportunity of invoking several PAW commands by just one command line. I have written some analysis tools for the analyses in Chapter 4 and 5, but only the programs for β delayed γ emission will be discussed here, because they might have common interest as standard tools for γ analysis. The programs used in the β delayed neutron emission analysis are more special and can properly not find any broad applicability.

3.4.2.1 The *GFIT* fitting routine

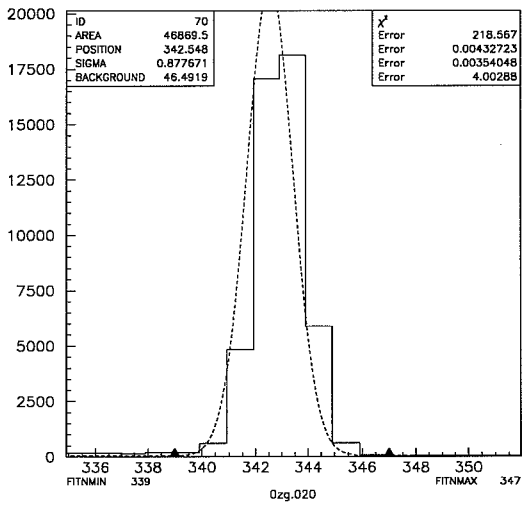

Figure 3.12: Output from the GFIT program.

When fitting from PAW one has the opportunity to use the *MINUIT*[20] tool which is a part of the CERN Program Library. This tool enables determination of the minimum value of a multi-parameter function and a further analysis of the shape of the function around the minimum. But since the internal Gauss function in PAW is not normalized and the calls to MINUIT can be unstable the fitting routine *GFIT* was used instead. The normalized Gaussian distribution is defined by(see Appendix C.2):

$$G(E) = \frac{1}{\sigma\sqrt{2\pi}} e^{\left(-\frac{(x-\mu)^2}{2\sigma^2}\right)} . \tag{3.19}$$

The function used for minimization can be written as:

$$G(E)_{min} = X(4) + X(1)\cdot\left[dfreq\left(\frac{dble(i+1.5)-X(2)}{X(3)}\right) - dfreq\left(\frac{dble(i+0.5)-X(2)}{X(3)}\right)\right], \tag{3.20}$$

where *dfreq* is the *CERNLIB*[19] *Normal Frequency Function* in double precision and $X(1-4)$ are the fit parameters. *GFIT* consists of two components: the PAW macro *gfit.kumac* (see Appendix A.2.1) and the compiled fortran code *gfit.out* (see Appendix A.2.2). A further description of how the macro *gfit.kumac* works can found in the header of the macro file. The fortran code also uses *HBOOK*[21] routines which are a part of the CERN Program Library as well. This macro starts with calling the compiled fortran code *gfit.out*, and it uses a data file *gaussfit.dat* with values made by the fortran code. A fit output of a typical γ line is shown in figure 3.12.

3.4.2.2 The *LFIT* fitting routine

The Gaussian distribution does not work for the Doppler shifted 3368 keV line in ^{10}Be (see decay scheme in figure 2.5). Instead the normalized Lorentz distribution (also known as the Cauchy distribution by statisticians and the Breit-Wigner distribution by non-atomic physicists) is used:

$$L(E) = \frac{\frac{\Gamma}{2\pi}}{(E-E_0)^2 + \frac{\Gamma^2}{4}}\,. \tag{3.21}$$

The corresponding minimization function is defined by:

$$L(E)_{min} = X(4) + X(1)\cdot\frac{\frac{X(3)}{2\pi}}{(dble(i+0.5)-X(2))^2 + \frac{X(3)^2}{4}}\,. \tag{3.22}$$

This distribution provides more trust worthy results than the Gaussian distribution, but it is still not good enough (see the discussion of the experimental ^{11}Li results in Section 4.4). The programs used for the Lorentz fitting are the PAW macro *lfit.kumac* and the compiled fortran code *lfit.out*. The macro is very similar to the *gfit.kumac* macro. The only difference is the call of the *lfit.out* program and the designation of the width of fitted peak (changed to Γ). The intermediate data file is called *lorentz.dat*. The fit function is changed to (3.22) in the subroutine *FCN* in the fortran code (see Appendix A.3.2). A further description of how to invoke the fitting routine can be seen in the header of the macro file in Appendix A.2.1.

3.4.2.3 The *SUM* fitting routine

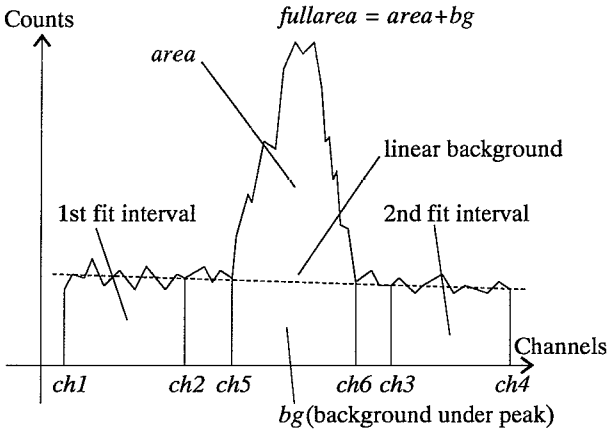

Figure 3.13: Sketch of summation on a peak.

The *GFIT* routine is not providing a correct estimation (see figure 3.12) of the area and the position of a given peak. This is because the γ lines are not Gaussians[24, from page 166], but have peak shapes consisting of several contributions. Therefore another more robust and less model dependent routine is necessary, and it is called *SUM*. It counts the number of counts in each channel instead of fitting them to a distribution. A sketch of a peak fitted by the summation macro is shown in figure 3.13. A description of how to invoke the macro *sum.kumac* can be found in the header of the macro file in Appendix A.1. The macro calculates the value of the peak area and the number of background counts under the peak and their respective errors. The calculation of these values is done by first extracting from the left fit interval ($ch1$-$ch2$) two vectors X and Y which are the channel numbers and number of counts respectively (see table 3.3 for explanation of the variables). The errors from the Y vector is calculated just by taking the square root of the values in the Y vector and stored in the vector ΔY. The same is done for the right fit interval ($ch3$-$ch4$), where the new vectors are appended to the vectors from the left interval. X, Y and ΔY now have the indices from 1 to the sum $fi = ch4 - ch3 + ch2 - ch1 + 3$ (3 because of the way PAW treats vectors) of the channels in the two intervals. A linear fit of the vectors X, Y and ΔY is now performed, and the resulting values are stored in the variables α and β , which are the slope and interception of the linear fit. The errors are stored in the variables $\Delta\alpha$ and $\Delta\beta$. The number of background counts under peak

Names in *sum.kumac*	Names in *text*	Comments
XXX	X	x-values for the linear background fit
YYY	Y	y-values for
DYYY	ΔY	errors of the y-values
alpha	α	slope from the linear fit
beta	β	interception from the linear fit
dalpha	$\Delta\alpha$	error of the slope
dbeta	$\Delta\beta$	error of the interception
bg	bg	background under the peak
dbg	Δbg	error of the background
fullarea	$fullarea$	total area of the peak
dfullarea	$\Delta fullarea$	error of the total area
area	$area$	area of the peak
darea	$\Delta area$	error of the area
x1	$ch1$	1st point in left interval
x2	$ch2$	2nd point in left interval
x3	$ch3$	1st point in right interval
x4	$ch4$	2nd point in right interval
x5	$ch5$	1st point in peak interval
x6	$ch6$	2nd point in peak interval
x5r	$ch5R$	real value of $x5r$
x6r	$ch6R$	real value of $x6r$
fi	fi	length of fit interval for lin. fit
XX	XX	contents of the histogram
XY	XY	running sum of XX

Table 3.3: The first column are the variable names used in the PAW macro in Appendix A.1, and the second column are the corresponding names used in the text below. The third column are some short explanations of what the variables are used for.

is then calculated by (linear background assumed):

$$bg = 0.5(ch6R - ch5R)(\alpha(ch6R + ch5R) + 2 \cdot \beta) \,, \tag{3.23}$$

and by assuming a negative slope of the linear fit. $ch5R$ and $ch6R$ are the *real* values of the peak fit interval ends. The error of bg is calculated by:

$$\Delta bg = \sqrt{\left[(-0.5(ch5R - ch6R)(ch5 + ch6)\Delta\alpha)^2 + ((ch6R - ch5R)\Delta\beta)^2\right]} \,. \tag{3.24}$$

The area of the peak with background included is calculated by a feature of the PAW *array manipulation* component *SIGMA*[18, Chapter 6], called *sumv*. The vector XY consists of a running sum of the vector XX, which is the contents of the total histogram. The area $fullarea$ of the peak with background is then the difference between the values of the vector XY for the indices $ch6$ and $ch5$ and the error $\Delta fullarea$ is the square root of $fullarea$.

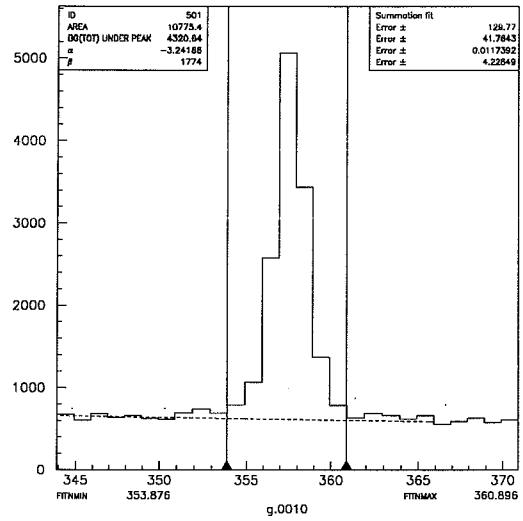

Figure 3.14: Output from summation macro *sum.kumac* .

The area of the peak alone can then be calculated as:

$$area = fullarea - bg \ , \tag{3.25}$$

and the corresponding error as:

$$\Delta area = \sqrt{\Delta fullarea^2 + \Delta bg^2} \ . \tag{3.26}$$

3.4.3 The efficiency fitting program *eff_calib.f*

As will be discussed in Section 4.3.1 it is sufficient to only fit the linear part of the efficiency curve for the HPGe detector. The program used for this purpose is called *eff_calib.f* . It is written in *Fortran 77*[9], and it uses HBOOK and MINUIT function calls (see Appendix A.4 for the fortran code). The fit problem is discussed in Section 4.3.1. The fortran program uses four data files, each corresponding to the used calibration sources in the γ analysis (two known and two unknown sources). It is fitting four parameters: slope , interception, offset for ^{56}Co and offset for ^{152}Eu. First it fixes the two offsets and calculates a linear fit for the known sources. Then it releases the offset for ^{56}Co and fixes the calculated slope and interception from the known sources. It now includes the relative efficiencies for ^{56}Co and calculates the offset. This offset is now fixed and then it calculates the offset for ^{152}Eu including the corresponding relative efficiencies. The result of the linear efficiency fit is

then the slope, interception and the two offsets, all including the calculated errors.

Chapter 4

β delayed γ emission from ^{11}Li

4.1 The experiment

This experiment was performed at the experimental Nuclear Physics Department ISOLDE at CERN in Geneva, Switzerland. The motivation was to improve the precision of earlier experimentally found branching ratios of the γ decays of the daughter nuclei ^{11}Be, ^{10}Be and ^{11}B from the β decay of ^{11}Li. In particular the extremely fast decay of the first excited state of ^{11}Be at 320 keV to the ground state was of special interest (see Section 2.3.4.1).

4.2 The setup

The experimental setup for the γ experiment was build at the end of August, 1993, and the ^{11}Li experiment was performed October, 1993. The experiment was done simultaneously with the neutron-experiment (will be discussed in Chapter 5) and the calibration of the γ detector was performed November 20, 1993. The setup was placed at the beam line end called RAØ just after the ISOLDE tape station (see figure 3.1). The target used in this experiment was made of Tantalum and placed in the GPS target station. The ion source was a small tube of Tungsten (see Section 3.1.1). With the GPS ^{11}Li ions were selected (Section 3.1) and directed to the experimental setup RAØ. The beam time was shared between the two setups (RAØ and LA1) by switching the beam by the "switch-yard" in the beam line system to the two setups.

4.2.1 The experimental setup

At the end of the ISOLDE beam line system a circa 50 cm long collection tube of 2 mm thick stainless steel was attached (see figure 4.1). The beam

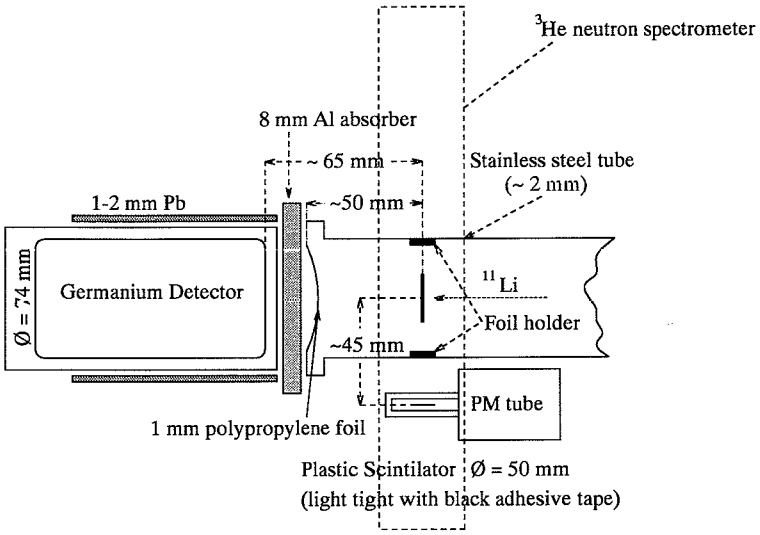

Figure 4.1: Experimental setup

was stopped on a thin aluminized mylar foil . Since it was not possible to drill any holes in this tube, the holder shown in figure 4.2 was constructed. The base of the holder was a strong spring, which when compressed could be put in place in the tube (circa 50 mm from the end of the tube). This had to be done with a special pair of tongs. To the spring four steel wires were attached, making up a square, on which the foil was placed by squeezing it in between the wires. Glue was not used because of the fumes, which would reduce the quality of the vacuum drastically . Four screws were mounted in the spring to secure that it would not move when the setup was pumped.

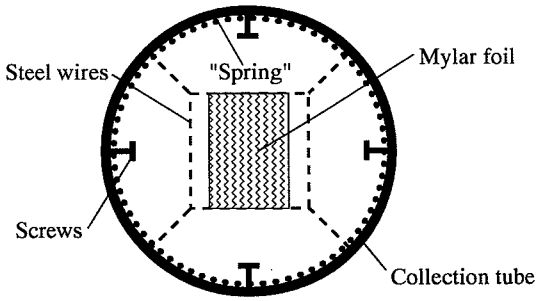

Figure 4.2: Cross section of the collection tube.

Behind the foil a Germanium detector was placed and below the foil a plastic β detector was situated. On the sides two ^{3}He n-spectrometers were located, but due to excessive noise they did not give usable results. All detectors were placed outside the collection tube. The Germanium detector was wrapped in a 2-3 millimeter thick lead "foil" to prevent background disturbances from the experimental hall. An 8 millimeter aluminum absorber was placed between the end of the collection tube and the front of the Germanium detector leaving circa 2 mm of space between them. This was done to prevent electrons from the β decay to enter the Germanium detector, and distort the coincidence efficiency. The Germanium detector was a *GEM-25185-P*[28, page 500] of the *High Purity* type, and the solid angle was calculated by (3.10) and (3.11) to $\Omega_{HPGe} \simeq 6.5$ %. The β detector was a plastic scintillator which will be described in more detail in the next chapter, where this type of detector also was used. The solid angle of the detector was $\Omega_\beta \simeq 6.3$ % in this setup.

4.2.2 The electronic setup

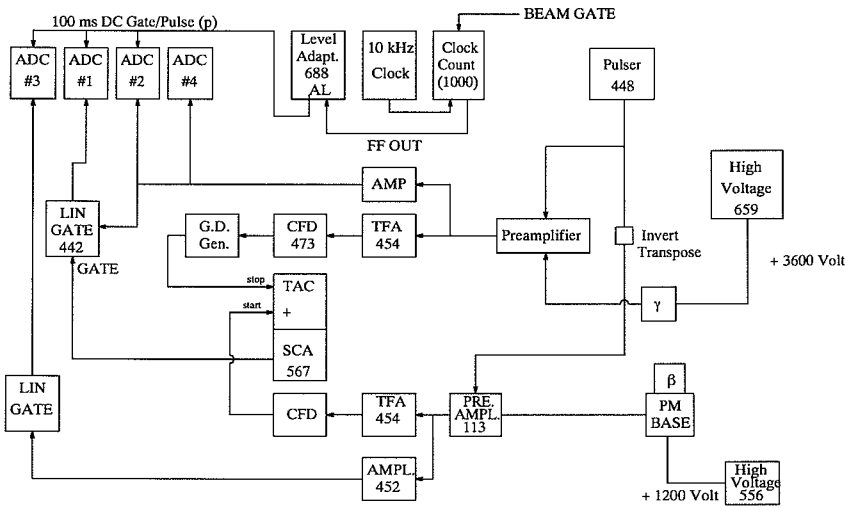

Figure 4.3: Electronic setup

A schematic overview of the electronic setup is shown in figure 4.3. The main gate of the experiment was the beam gate from the PS-BOOSTER supplied via the ISOLDE control room. This beam gate came just after the impact of the 1 GeV proton pulse. The beam gate was activating our clock counter system which provided a 100 ms DC gate for the ADC's 1-3 (see table 4.1 for

ADC #	Particle Detection	Comments
1	hardware β/γ-coincidences	Pulse gated
2	γ-singles	Pulse gated
3	β-singles	Pulse gated
4	free running γ-singles	Not gated

Table 4.1: ADC configuration.

the ADC arrangement). The HPGe detector was powered by a high voltage module which provided 3600 Volts. The signal from the HPGe detector was sent to a preamplifier combined with the signal from a pulser, which served as a reference in the spectra from the different ADC's. The pulser signal could be seen as a high energy peak at approximately 3 MeV in the spectra involving γ measurement. The number of counts, 10 pulses/s, illustrated the duration of the experiment runs. This should later show out to be quite important due to problems with ADC 4. From the preamplifier the signal was sent to an amplifier and the coincidence arrangement of modules. From the amplifier is was sent further to ADC 4 and to a linear gate module. The plastic β detector was powered by a high voltage module which provided 1200 Volts. The signal was sent to a preamplifier and again mixed by the pulser signal. From the preamplifier is was sent to an amplifier and to the coincidence arrangement. From the amplifier it was sent to a linear gate and then into ADC 3. From the coincidence modules a signal was sent to the linear gate with the amplified γ signal and from the linear gate into ADC 1. The obtained data were sent via an ethernet connection from the crate controlling the applied modules to a VMS VAX computer for storage on tape in singles mode.

4.3 Calibration experiment

As discussed in Section 3.2.5 the efficiency of the HPGe detector is quite important, because of the relatively low efficiency of detection compared to detectors used for charged particles. This fact is due to the necessity of secondary interactions of the neutral γ rays to provide light pulses in the detector (see Section 3.2.1). This part of the experiment was done without any beam gate.

4.3.1 The efficiency calibration of the HPGe detector

When the total efficiency ε_{tot} was defined in equation (3.4) is was assumed that no matter how low the energy was, all interactions were expected to be registered. When considering a differential pulse height distribution like the one shown in figure 4.4, it is worth while considering peak efficiencies instead. The peak efficiency assumes that only those interactions which deposit the full

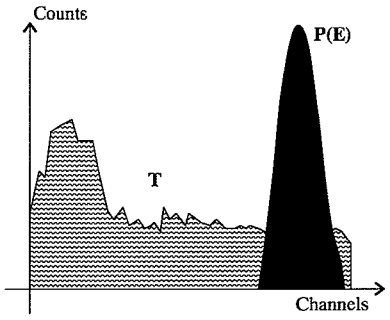

Figure 4.4: Sketch of a differential pulse hight distribution with one peak. T is the total number of counts in the spectrum and P(E) is the number of counts in the peak.

energy of the incident radiation are registered. These full energy events in a differential pulse height distribution normally are evidenced by a peak which appear in the right of the spectrum. The events which do not deposit all their radiation energy will appear to the left in the "swamp" in the spectrum. The number of full energy events can be found by integrating the area under the peak (shown in black). The peak efficiency can be expressed in terms of the total efficiency by:

$$\varepsilon_\gamma^P(E) = \varepsilon_{tot} \cdot \frac{P(E)}{T} = \varepsilon_\gamma^{int} \cdot \frac{\Omega}{4\pi} \cdot \frac{P(E)}{T} \,, \tag{4.1}$$

where the $\frac{P(E)}{T}$ indicates the ratio between counts in the peak and the total number of counts at all energies (see figure 4.4). Ω is the solid angle of the setup. We do not know the intrinsic efficiency $\varepsilon_\gamma^{int}(E)$, but instead we can use the definition of the energy dependent intensity from the γ decay of parent nuclei:

$$N_\gamma(E) = N_0 \cdot \varepsilon_\gamma^P(E) \cdot b_\gamma(E) \,, \tag{4.2}$$

where $b_\gamma(E)$ is the branching ratio. If we know the initial γ intensity N_0 at the beginning of the experiment run, we can in theory by measuring $N_\gamma(E)$

for the reference lines from the applied calibration sources ^{133}Ba and ^{60}Co (both have known initial activities) and ^{56}Co, ^{152}Eu and ^{106}Rh/^{106}Ru (all unknown), find $\varepsilon_\gamma^P(E)$ which then is the only unknown term in (4.2). This makes us able to make an efficiency curve like the one shown in figure 4.5. The range of γ energies from the calibration sources from this experiment only allows us to get the linear part of the efficiency curve in figure 4.5. This will later show out to be no problem in fact an advantage, since the lowest ^{11}Li γ energy is at approximately 219 keV and the linear part begins at circa 150 keV.

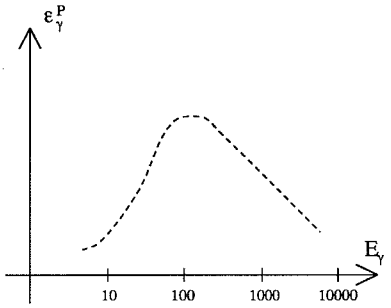

Figure 4.5: Sketch of an ideal efficiency curve.

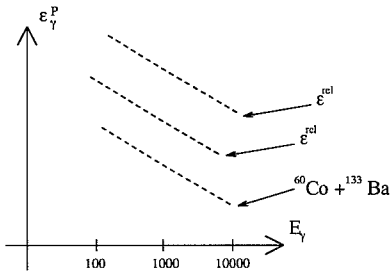

Figure 4.6: Sketch of an efficiency curve with relative lines included

In reality we do not know N_0, but instead we know the activities $A_{20/11/93}$ of the sources ^{60}Co and ^{133}Ba at the time of experiment (see table 4.3). We can by measuring N_γ calculate the "experimental activity" from the known sources for the different γ energies, since we know the time periods of the ^{60}Co and ^{133}Ba runs from table B.1 by:

$$A_\gamma^{exp}(E) = \frac{N_\gamma(E)}{\Delta T}\,, \tag{4.3}$$

where ΔT is the time period of the experiment. The efficiency for the known sources can then be calculated by:

$$\varepsilon_\gamma^{exp}(E) = \frac{A_\gamma^{exp}(E)}{b_\gamma(E) \cdot A^\gamma_{20/11/93}} \,. \tag{4.4}$$

Using the calculated activity (4.3) of the known sources we can finally write the experimental efficiency as:

$$\varepsilon_\gamma^{exp}(E) = \frac{N_\gamma(E)}{\Delta T \cdot A^\gamma_{20/11/93} \cdot b_\gamma(E)} \,, \tag{4.5}$$

where all terms on the right side are known or measurable entities. The corresponding errors found by applying the *Law of propagating errors* (Appendix C.3) are:

$$\Delta\varepsilon_\gamma^{exp}(E) = \varepsilon_\gamma^{exp} \sqrt{\left[\frac{\Delta N_\gamma}{N_\gamma}\right]^2 + \left[\frac{\Delta b_\gamma}{b_\gamma}\right]^2 + \left[\frac{\Delta A^\gamma_{20/11/93}}{A^\gamma_{20/11/93}}\right]^2 + \left[\frac{\Delta(\Delta T)}{\Delta T}\right]^2} \,. \tag{4.6}$$

For the unknown sources ^{56}Co, ^{152}Eu and ^{106}Rh/^{106}Ru we do not know N_0 or the activities at the experiment time, but instead we can calculate a relative value of the efficiency by:

$$\varepsilon_\gamma^{rel}(E) = \frac{N_\gamma(E)}{b_\gamma(E)} \,, \tag{4.7}$$

where $b_\gamma(E)$ is the branching ratios for the unknown sources. The corresponding errors are:

$$\Delta\varepsilon_\gamma^{rel}(E) = \varepsilon_\gamma^{rel}(E) \sqrt{\left[\frac{\Delta N_\gamma(E)}{N_\gamma(E)}\right]^2 + \left[\frac{\Delta b_\gamma(E)}{b_\gamma(E)}\right]^2} \,. \tag{4.8}$$

If we plot the values of the relative efficiencies in the same plot as the absolute values of the efficiency for the known sources, we will get something like figure 4.6. The data points from the unknown sources will theoretically be on straight lines with slopes equal to the slope of the straight line from the ^{60}Co and ^{133}Ba data points. The straight line behavior is due to the energy range of the calibration sources. If the γ energies were lower than approximately 200 keV, this linear approximation would not work. We now need to move the relative efficiency lines down to the line of the known sources. By "moving"

the lines from the relative efficiency until they fit the line from ^{60}Co and ^{133}Ba we get two factors $F_{^{56}Co}$ and $F_{^{152}Eu}$ for the two unknown sources ^{56}Co and ^{152}Eu (^{106}Rh/^{106}Ru is not included, see Section 4.3.3). $\varepsilon_\gamma^{rel}(E)$ should then in non logarithmic scale be divided by these factors to get the absolute semi experimental efficiency:

$$\varepsilon_{ABS}^{semi}(\text{source}) = \frac{\varepsilon_\gamma^{rel}(E)}{F_{\text{source}}} . \tag{4.9}$$

When plotting these values together with the values for the known sources we will get a "straight" line with a formula, for which we can determine the parameters by an ordinary linear regression. The quotation of "moving"implies that this is not straight forward to do. One could of course do it by eye on a log-log scaled paper, but to be more accurate one has to use a special fitting routine. This routine is described in section 3.4.3. The Fortran program used for this fitting routine can be seen in Appendix A.4. It drags the relative efficiency lines down as well as making a linear regression calculation at the same time. The calculated theoretical efficiency can then be written as:

$$\varepsilon_\gamma(E) = 10^{A \cdot log(E)+B} , \tag{4.10}$$

and the calculated errors as:

$$\Delta\varepsilon_\gamma(E) = \varepsilon_\gamma(E) \cdot ln(10) \cdot \sqrt{(log(E) \cdot \Delta A)^2 + (\Delta B)^2} . \tag{4.11}$$

Since A and B are not physical entities, we cannot use the calculated errors when determining the efficiency for a given γ energy. Instead we have to estimate the errors of the efficiencies, where the errors of the activities will be essential. This will be done in Section 4.3.3.

4.3.2 The calibration sources

The datasheet of the two known sources for the calibration of the efficiency of the Germanium detector is presented in table 4.2. The British Calibration Service has approved the measurements of the reference sources 2669RP and 2667RP done by Amersham International UK, and an estimation of the overall uncertainty of ^{60}Co and ^{133}Ba data is $\pm$ 3.9 % and $\pm$ 7.0 %, respectively. The time from the manufacturing of the sources until the date of the experiment is $t = 8.55 \pm 1.37 \cdot 10^{-3}$ years, where the uncertainty of this period of time is taken to be 0.5 days. The activities of the known sources November 20,

Source	Reference Number	Reference Time GMT 01/05/1985	$T_{1/2}$ [years]	A_0 [μCi]
^{60}Co	2669RP	12.00	5.2719±0.0014	1.092±0.043
^{133}Ba	2667RP	12.00	10.57±0.04	0.983±0.069

Table 4.2: Datasheet of the two known calibration sources.

Source	Reference Number	$A_{20/11/93}$ [bq]
^{60}Co	2669RP	13123.1±899.2
^{133}Ba	2667RP	21010.7±1579.7

Table 4.3: The activities and errors of the two known sources

1993 are calculated by:

$$\begin{aligned} A_{20/11/93} &= A_0 \exp(-k \cdot t) \\ &= A_0 \exp(-\frac{\ln 2}{T_{1/2}} \cdot t) \ . \end{aligned} \tag{4.12}$$

and the errors of the activities are calculated by using the *Law of propagating errors* (explained in Appendix C.3):

$$\Delta A_{20/11/93} = A_{20/11/93} \sqrt{\left[\frac{\Delta A_0}{A_0}\right]^2 + \left[\frac{\ln 2 \cdot t \cdot \Delta T_{1/2}}{T_{1/2}^2}\right]^2 + \left[\frac{\ln 2 \cdot \Delta t}{T_{1/2}}\right]^2} \ . \tag{4.13}$$

The activities of the sources ^{60}Co and ^{133}Ba at the experiment start time calculated by (4.12) and (4.13) using the values in table 4.2 are shown in table 4.3.

4.3.3 The experimental results

The calibration experiment involves fourteen runs with various calibration sources. Every run consists of three parameters: γ singles, β/γ coincidences and additional γ singles with higher cut-off. Only the γ singles were used

in the efficiency calibration. The histogram identification numbers and run durations are shown in table B.1 in Appendix B. An extract of the experimental fit values of the γ singles of the most useful runs is shown in table 4.4 and table 4.5. Column 1 is the energies of the γ lines and column 2 is the

E_γ [keV]	$b_\gamma \pm \Delta b_\gamma$ [%]	N_{Sum} [counts]	N_{Gauss} [counts]	σ	Fit pos. [ch]
^{133}Ba - ID 70 - Known source # 2667RP					
276.4	7.17±0.04	6715.6±98.4	6836.6±99.0	0.83±0.01	255.83±0.01
302.853	18.3±0.07	16023.6±137.8	16234.0±136.2	0.851±0.007	284.657±0.008
356.015	62.0±0.3	46389.1±220.9	46815.0±218.2	0.877±0.003	342.547±0.004
383.8505	8.93±0.06	6344.9±93.2	6388.5±82.9	0.89±0.01	372.83±0.01
^{60}Co - ID 71- Known source # 2669RP					
1173.238	99.89±0.02	27476.9±176.4	27826.0±172.9	1.173±0.006	1235.834±0.008
1332.502	99.980±0.001	24865.7±167.4	24981.8±159.4	1.232±0.006	1412.830±0.008
^{133}Ba - ID 72					
276.4	7.17±0.04	2350.9±68.2	2433.3±83.9	0.86±0.04	255.81±0.03
302.853	18.3±0.07	5658.4±90.6	5810.8±92.5	0.841±0.01	284.63±0.01
356.015	62.0±0.3	16571.0±137.0	16943.4±136.9	0.859±0.007	342.547±0.008
383.8505	8.93±0.06	2367.0±64.5	2314.2±61.0	0.86±0.02	372.86±0.02
^{56}Co - ID 73					
846.764	99.930±0.006	362641.3±617.0	363803.4±636.8	1.037±0.002	875.446±0.002
1037.844	14.12±0.04	42018.7±242.8	42935.7±263.3	1.126±0.007	1085.781±0.007
1238.287	66.8±0.7	171356.7±424.7	172480.2±433.2	1.203±0.003	1308.087±0.003
1771.35	15.48±0.04	29172.5±188.9	29466.5±204.8	1.403±0.009	1902.884±0.009
2015.179	3.03±0.01	5156.0±96.4	5235.9±120.6	1.52±0.03	2176.53±0.03
2034.759	7.76±0.03	13071.7±136.6	13141.1±140.0	1.52±0.02	2198.55±0.02
2598.46	16.95±0.04	22920.8±177.2	22957.7±178.5	1.74±0.01	2834.87±0.01
3201.954	3.09±0.05	3455.3±93.1	3282.9±73.2	1.89±0.04	3520.96±0.04
3253.417	7.60±0.15	8331.5±108.5	8438.9±109.9	2.02±0.03	3579.61±0.02
3272.998	1.81±0.03	1954.2±87.4	2050.6±60.2	2.17±0.06	3602.01±0.05
3451.154	0.9±0.2	892.6±49.2	883.4±39.7	1.98±0.09	3806.32±0.08
^{56}Co - ID 74					
846.764	99.930±0.006	223304.6±481.8	224141.4±500.0	0.914±0.002	915.337±0.002
1037.844	14.12±0.04	26133.3±183.2	26608.4±218.9	1.001±0.008	1127.817±0.008
1238.287	66.8±0.7	105803.4±332.9	106117.0±340.1	1.078±0.003	1351.820±0.004
1771.35	15.48±0.04	18171.3±150.9	18398.8±169.9	1.29±0.01	1950.17±0.01
2015.179	3.03±0.01	3141.0±81.9	3162.4±80.0	1.36±0.03	2225.22±0.03
2034.759	7.76±0.03	8069.6±114.5	8134.9±109.3	1.39±0.02	2247.38±0.02
2598.46	16.95±0.04	14286.5±141.4	14369.5±143.1	1.66±0.02	2886.36±0.02
3201.954	3.09±0.05	2154.9±83.4	2156.9±53.8	1.88±0.05	3573.95±0.04
3253.417	7.60±0.15	5012.9±95.3	5029.3±81.0	1.86±0.03	3632.61±0.03
3272.998	1.81±0.03	1242.1±79.4	1275.9±42.0	1.98±0.06	3655.0±0.06
3451.154	0.9±0.2	562.4±46.1	578.5±31.2	1.9±0.1	3859.49±0.09

Table 4.4: The experimental results from the calibration runs with histograms ID 70 to 74. σ and *Fit pos.* are parameters from *GFIT*. All energies and branching ratios are taken from reference [24].

corresponding branching ratios or photon emission probabilities[24, Chapter 6]. Column 3 is the number of counts in the peaks fitted by *SUM* and column 4 is the equivalent number of counts fitted by *GFIT*. Column 5 and 6 are σ width and peak position, respectively; both fit parameters from the Gaussian

fit routine. In figure 4.7 the relative difference between the number of counts found by *SUM* and *GFIT* is presented. One can see that the Gaussian fit method overestimates a bit compared to the sum method because of the majority of positive residua. This overestimation is, however, within 5 %, so the

E_γ [keV]	$b_\gamma \pm \Delta b_\gamma$ [%]	N_{Sum} [counts]	N_{Gauss} [counts]	σ	Fit pos. [ch]
^{133}Ba - ID 75A					
276.4	7.17±0.04	15706.7±154.9	16235.6±188.6	0.711±0.009	291.469±0.008
302.853	18.3±0.07	38018.2±216.2	38277.4±243.9	0.721±0.005	320.883±0.005
356.015	62.0±0.3	112044.3±345.5	112608.4±350.6	0.735±0.002	379.955±0.003
383.8505	8.93±0.06	15535.3±143.4	15560.7±153.4	0.731±0.008	410.895±0.008
^{56}Co - ID 75B					
846.764	99.930±0.006	48946.3±229.4	48999.2±231.7	0.927±0.004	926.814±0.005
1037.844	14.12±0.04	5695.6±94.0	5756.7±95.7	0.99±0.02	1140.78±0.02
1238.287	66.8±0.7	23312.6±162.1	23321.1±160.1	1.097±0.007	1365.881±0.008
1771.35	15.48±0.04	3942.2±87.0	3999.9±71.2	1.28±0.02	1965.51±0.02
2015.179	3.03±0.01	729.2±65.0	760.1±40.0	1.53±0.08	2240.5±0.07
2034.759	7.76±0.03	1663.0±69.2	1691.0±49.9	1.42±0.04	2262.7±0.04
2598.46	16.95±0.04	3037.8±81.4	3044.9±64.1	1.65±0.03	2900.05±0.03
3201.954	3.09±0.05	472.5±55.9	466.9±24.1	1.9±0.1	3583.4±0.1
3253.417	7.60±0.15	1099.8±88.7	1084.8±36.5	1.92±0.06	3641.87±0.07
3272.998	1.81±0.03	259.8±52.4	263.8±19.1	1.8±0.2	3664.2±0.1
3451.154	0.9±0.2	129.5±48.6	103.7±11.6	1.6±0.3	3866.6±0.2
^{152}Eu - ID 76					
244.6989	7.54±0.05	45136.7±257.0	46364.1±311.3	0.848±0.006	221.196±0.006
344.2811	26.52±0.18	117842.7±367.8	120018.4±399.9	0.867±0.003	329.711±0.003
411.126	2.246±0.016	8093.7±124.2	8197.9±162.0	0.86±0.02	402.47±0.02
867.39	4.23±0.03	7909.1±124.5	7950.9±144.8	1.04±0.02	897.74±0.02
964.055	14.60±0.08	25875.8±176.8	25650.3±193.7	1.071±0.008	1003.990±0.008
1112.087	13.56±0.06	21479.7±166.3	21518.9±173.9	1.152±0.009	1167.630±0.009
1212.97	1.423±0.01	1945.0±67.2	1999.3±90.0	1.18±0.05	1279.4±0.04
1299.152	1.630±0.010	2183.1±60.2	2211.9±66.9	1.22±0.04	1375.26±0.03
1408.022	20.80±0.12	27023.8±176.7	26991.4±173.8	1.250±0.007	1496.410±0.008
^{106}Rh + ^{106}Ru - ID 77					
511.860	20.5±0.5	593683.4±791.7	582292.1±854.6	1.136±0.002	511.658±0.002
621.8	9.95±0.18	136968.2±387.3	138252.3±420.5	0.942±0.003	631.456±0.003
1050.4	1.47±0.04	12548.4±134.2	12899.4±177.8	1.12±0.01	1099.19±0.01
^{106}Rh + ^{106}Ru - ID 78					
511.860	20.5±0.5	595806.8±793.8	582292.1±854.6	1.136±0.002	511.658±0.002
621.8	9.95±0.18	136823.9±390.0	138252.2±420.5	0.942±0.003	631.456±0.003
1050.4	1.47±0.04	12699.8±134.0	12899.4±177.8	1.12±0.01	1099.19±0.01
^{106}Rh + ^{106}Ru - ID 79					
511.860	20.5±0.5	1813690.4±1381.0	1775643.0±1491.2	1.230±0.001	511.372±0.001
621.8	9.95±0.18	273390.4±547.7	275674.8±603.3	0.943±0.002	631.388±0.002
1050.4	1.47±0.04	26208.0±204.0	26575.9±278.9	1.16±0.01	1099.06±0.01

Table 4.5: The experimental results from the calibration runs with histograms ID 75 to 79. σ and *Fit pos.* are parameters from *GFIT*. All energies and branching ratios are taken from reference [24].

agreement is acceptable. For all further illustration the data from the *SUM* method have been applied. In table 4.6 the experimental efficiencies for the

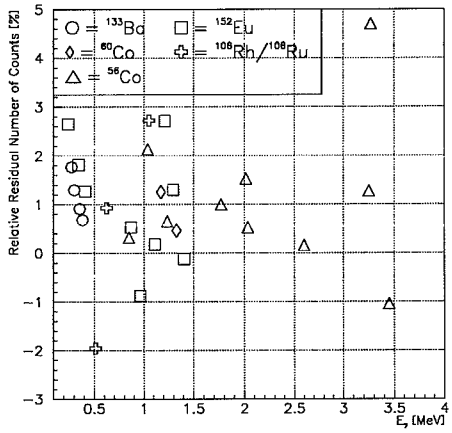

Figure 4.7: The relative residual difference $\frac{NGauss-NSum}{NGauss} \cdot 100$ of the efficiencies found by *GFIT* and *SUM* for all calibration sources.

histograms 70, 71, 73, 76 and 77 are presented. Run 73 has been chosen on the grounds of better statistics and run 77 has been chosen on the basis of being the cleanest ^{106}Rh/^{106}Ru run (run 77 and 78 are identical). The efficiencies and corresponding errors are calculated by (4.5) and (4.6) for the

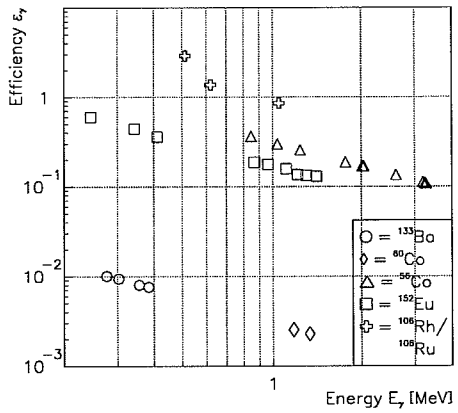

Figure 4.8: Plots of the efficiencies from table 4.6. The relative efficiencies are divided by 10000 to make them appear at the same scale as the absolute efficiencies for the known sources ^{133}Ba and ^{60}Co. The calculated values for ^{106}Rh/^{106}Ru are from histogram ID 77

E_γ [kev]	b_γ [%]	ε_{Sum} [%]	ε_{Gauss} [%]	E_γ [keV]	b_γ [%]	ε_{Sum} [%]	ε_{Gauss} [%]
^{133}Ba - # 2667RP - ID 70				^{56}Co - ID 73 continued			
276.4	7.17±0.04	1.007±0.073	1.025±0.074	3272.998	1.81±0.03	1080±51	1133±38
302.853	18.3±0.07	0.941±0.067	0.954±0.068	3451.154	0.9±0.2	992±227	982±223
356.015	62±0.3	0.804±0.057	0.812±0.058	^{152}Eu - ID 76			
383.8505	8.93±0.06	0.764±0.055	0.769±0.055	244.6989	7.54±0.05	5986±52	6149±58
^{60}Co - # 2669RP - ID 71				344.2811	26.52±0.18	4444±33	4526±34
1173.238	99.89±0.02	0.254±0.010	0.257±0.010	411.126	2.246±0.016	3604±61	3650±77
1332.502	99.98±0.001	0.229±0.009	0.230±0.009	867.39	4.23±0.03	1870±32	1880±37
^{56}Co - ID 73				964.055	14.6±0.08	1772±16	1757±16
846.764	99.93±0.006	3629±6	3641±6	1112.087	13.56±0.06	1584±14	1587±15
1037.844	14.12+0.04	2976±19	3041±21	1212.97	1.423±0.01	1367±48	1405±64
1238.287	66.8±0.7	2565±28	2582±28	1299.152	1.63±0.01	1339±38	1357±42
1771.35	15.48±0.04	1885±13	1904±14	1408.022	20.8±0.12	1299±11	1298±11
2015.179	3.03±0.01	1702±32	1728±40	^{106}Rh/^{106}Ru - ID 77			
2034.759	7.76±0.03	1684±19	1693±19	511.86	20.5±0.5	88473±2159	86617±2114
2598.46	16.95±0.04	1352±11	1354±11	621.8	9.95±0.18	27476±500	27706±505
3201.954	3.09±0.05	1118±35	1062±29	1050.4	1.47±0.04	17829±505	18079±527
3253.417	7.6±0.15	1096±26	1110±26				

Table 4.6: The experimental efficiencies.

two known sources ^{133}Ba and ^{60}Co. For the three unknown sources the relative efficiencies and corresponding errors are calculated by (4.7) and (4.8). These "efficiencies" have been plotted in figure 4.8. The different sources exhibit the same slope tendency except the ^{106}Rh/^{106}Ru calibration source. This is seen more clearly in figure 4.9 where the relative efficiencies of both

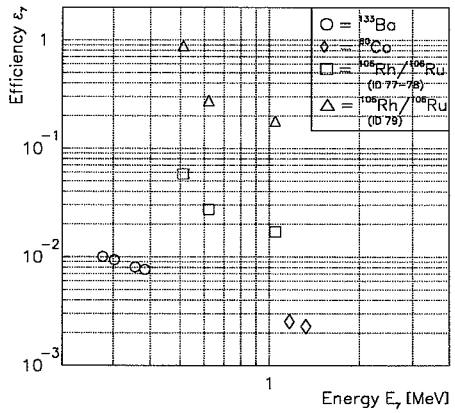

Figure 4.9: Comparison of the slopes of the relative efficiencies of the ^{106}Rh/^{106}Ru runs 77 and 79 to the efficiencies of the known sources ^{133}Ba and ^{60}Co. The relative efficiencies have been divided by 500000 and 100000, respectively.

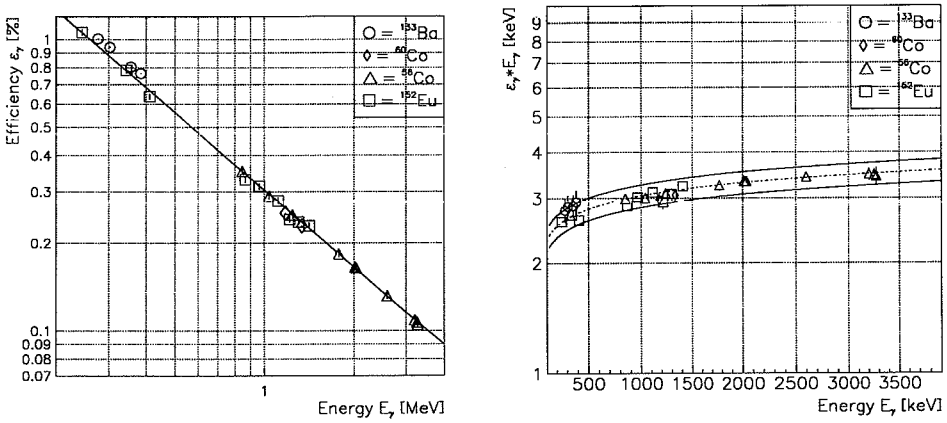

(a) Fitted absolute efficiency.

(b) 7 % error estimation of Efficiency times Energy versus Energy.

Figure 4.10: a) The efficiency fitted by *eff_calib.f* for the *SUM* fitted relative efficiencies. The straight line corresponds to the absolute efficiency from equation (4.10). b) ± 7 % error boundary estimation.

histogram 77/78 and 79 are compared to the absolute efficiencies. The point diverging is the strongest γ line (b_γ = 20.5±0.5 %) at 511.860 keV. This deviation is mainly due to positron annihilation radiation. The ^{106}Rh/^{106}Ru calibration source was therefore not used any further in the efficiency calibration. It is normally difficult to prevent detection of annihilation radiation, so ^{106}Rh/^{106}Ru sources should be used with care. The absolute and relative efficiencies from table 4.6 are fitted by the efficiency program *eff_calib.f* discussed in Section 3.4.3. The result is shown in figure 4.10a. The straight

Linear regression results		
$A \pm \Delta A$	-0.8827 ± 0.0036	Slope
$B \pm \Delta B$	0.132 ± 0.014	Interception
$F_{^{56}Co} \pm \Delta F_{^{56}Co}$	1026836 ± 23678	Offset factor for ^{56}Co
$F_{^{152}Eu} \pm \Delta F_{^{152}Eu}$	565757 ± 13185	Offset factor for ^{152}Eu
FCN	41.01355	χ^2 for the fit

Table 4.7: The results from *eff_calib.f* using *SUM* fitted efficiencies.

line representing the fitted efficiency is calculated by (4.10). The symbols correspond to the absolute efficiency for the known sources and the relative efficiency divided by the offset factors for the unknown sources. The calculated errors from (4.11) disappear in the symbols because of the log scale. The resulting fits are listed in table 4.7. Due to the problem of the additional covariance term in the *Law of propagating errors*, the real errors of the calculated efficiency cannot be derived from (4.11). The main dependence of the size of the errors is from the initial activities of the known calibration sources. These errors was chosen to be 5 %, and the errors on the absolute efficiencies are estimated conservatively to be 7 % (see figure 4.10b).

4.4 The ^{11}Li experiment

During this experiment there was a leak of ^{11}C into the experimental hall. This was due to a minor leak of from the target hall into a room just above. This room had a separate ventilation system which was drawing air from the experimental hall. By a mistake, a repair job on this ventilator made it draw air from the target hall into the experimental hall instead. There was not any health danger at any time. ^{11}C decays into ^{11}B by a β^+ decay with a half-life of 1223.1 ± 1.2 s. It consequently produces lots of positrons which very fast annihilate with electrons to give 511 keV γ rays. Due to the short half life it did not have any consequences for our experiment.

4.4.1 The experimental results

The ^{11}Li part consists of thirteen runs numbered from 1 to 13. Four parameters were measured: β/γ coincidences, γ singles, β singles and free running γ singles. The first three parameters were all gated by the proton beam gate (Section 4.2.2) and the last parameter was not gated at all. The corresponding histogram numbers, run durations and number of proton pulses can be viewed in table B.2. The fit values found by *SUM* of the γ line of 320 keV from ^{11}Be and the 2125 keV line from ^{11}B are listed in table 4.8 together with the lines 219, 2592, 2811 and 3368 keV from ^{10}Be. A Lorentz fit was tried for the 3368 keV peak, but the result was not satisfactory (see figure B.1 in Appendix B). The runs from 1 to 7 are not included, because the 8 mm aluminum absorber was not yet inserted in front of the HPGe detector. The peaks in the γ singles and free running were skew to the right, due to closely angular correlated electrons from the β decay of ^{11}Li entering the detector. The electrons deposited a small amount of their energy in the crystal before backscattering out again, and this could be seen as the skewness. The peaks

ID	The known energies of the β delayed γ emission from ^{11}Li					
	219 keV	320 keV	2125 keV	2590 keV	2811 keV	3368 keV
β/γ coincidences						
8		202.3±44.1				74.8±7.5
10		140.5±37.5				37.7±3.8
11	NA	140.8±33.2	NA	NA	NA	34.8±3.5
12		69.1±24.9				35.3±3.5
500		354.0±41.6				112.6±11.3
γ singles						
58	708.0±62.4	6109.4±103.9		1352.2±164.6	40±20	3625.2±166.3
60	407.4±52.6	4026.5±88.6		740.6±94.5	NA	2240.9±163.4
61	409.8±50.0	4142.3±89.7	NA	728.7⊥102.8	NA	2169.1±168.8
62	205.5±55.4	2378.4±66.9		454.5±127.0	NA	1421.4±152.1
501	945.9±60.7	10505.8±123.7		2063.1±114.0	105.6±33.2	6075.7±171.3
γ free running						
158		4987.1±153.0	711.6±47.1	1163.4±120.1		3000±150
160		3978.3±138.3	483.7±59.3	761.3±109.8		2253.9±197.1
161	NA	3930.8±136.9	483.7±57.1	772.0±111.7	NA	2307.3±210.0
162		2320.9±101.1	320.7±56.7	490.5±136.5		1338.0±147.0
503		10714.5±226.1	1238.5±60.4	1957.7±118.9		6059.3±216.7

Table 4.8: Experimental fit values from ^{11}Li experiment (see also table B.2).

could therefore not be used for internal check of the relative intensities of the lines. These runs showed bad count statistics in the β/γ coincidences as well. Run 9 and 13 were background runs which was used to check if any background lines had the same energies as the lines arising from the β decay of ^{11}Li. This was not the case. The only runs included in the final results are run 8 and the sum of run 10, 11 and 12. As seen in the table it is not possible to resolve the lines 219, 2592 and 2811 keV from the background in the β/γ coincidence spectra. The 2125 keV line will not show up in the coincidence spectra, due to the long-lived β decay of ^{11}Be. The errors of the 3368 keV line in the coincidence spectra were not adopted from *SUM*, but estimated to 10 % relatively. This was due to a very poor background (see figure 4.12) which made the summing routine calculate comparatively large errors. As for the coincidences the 2125 keV line was not present in the γ singles, due the 700 ms short measure time in every super-cycle. The observed peaks belonging to the β delayed γ emission from ^{11}Li are shown for the sum of the γ singles of run 10,11 and 12 in figure 4.11. The corresponding β spectrum is shown in figure 4.13. There was practically no background in the β spectra. In the free running γ singles both the 219 keV and the 2811 keV line drowned in the larger background. To the contrary the 2125 keV line was easily observed. The ADC 4 which was converting the free running pulses was very unstable and stopped during several runs. This is indicated for run 8, 10, 11 and 12 (and consequently for the sum as well) in figure 4.14. The three points in each

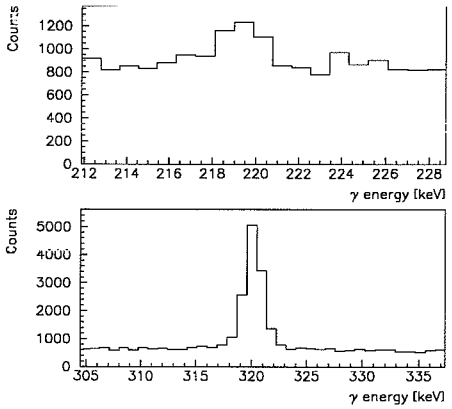

(a) The 219 and 320 keV lines

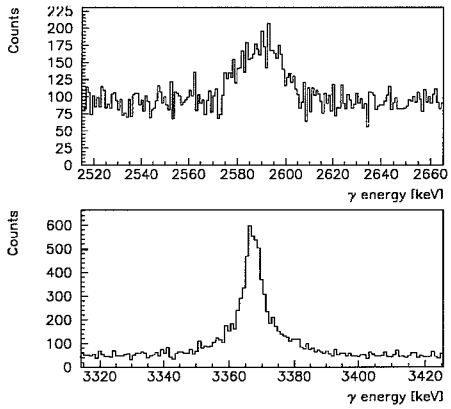

(b) The 2592 and 3368 keV lines

Figure 4.11: The four prominent peaks from the γ singles of the sum of run 10, 11 and 12.

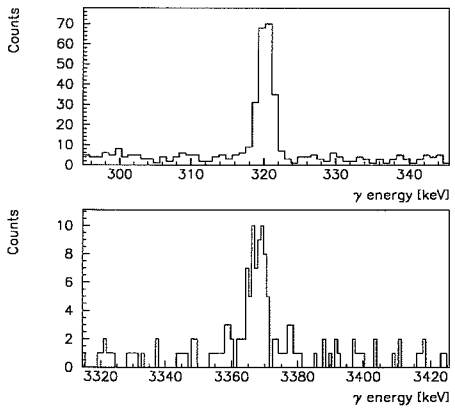

(a) 320 and 3368 keV

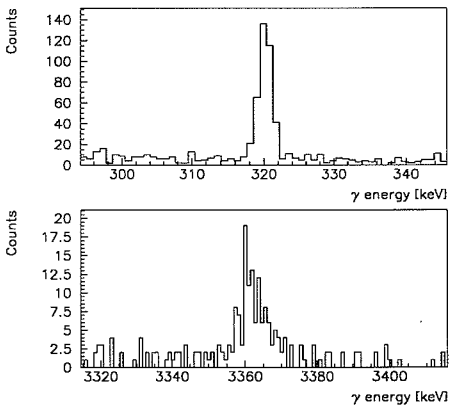

(b) 320 and 3368 keV

Figure 4.12: The β/γ coincidence spectra from histogram 8 and 500. Notice the very low background for both 3368 keV peaks.

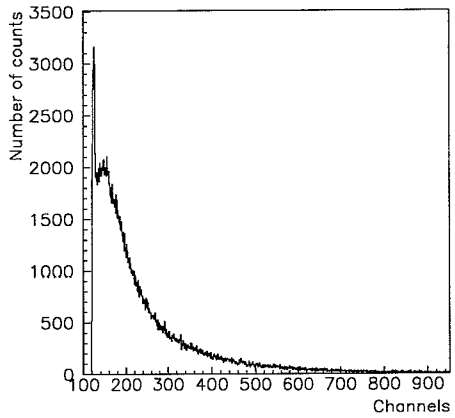

Figure 4.13: β spectrum from the sum of run 10, 11 and 12. The total number of counts is calculated from channel 0 to the channels just before the pulser peak at approximately channel 3500.

sequence belong to the β/γ coincidences, γ singles and β singles, respectively. The points are calculated by:

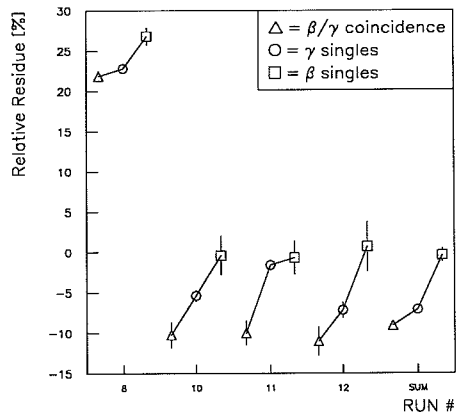

Figure 4.14: Relative residue between the three pulse gated ADC's and the expected number of counts calculated from the free running γ's.

$$Residue = \frac{N_{\beta/\gamma,\gamma,\beta} - P \cdot N_{\text{free running}}}{N_{\beta/\gamma,\gamma,\beta}} \cdot 100\% \,, \tag{4.14}$$

where

$$P = \frac{700 \text{ ms}}{14.4 \text{ s} \cdot 1000} = 4.9\% \,. \tag{4.15}$$

is the percentage of free running events expected to be observed in the pulse gated spectra. One can see that the ADC stopped drasticly in run 8. In run 10, 11 and 12 it did not stop for longer periods. The similar tendency of the β/γ coincidences lying lowest, the γ singles a bit higher and the β singles having the greatests values for every run is due to the dead times in the different detector electronics. The ADC converting the free running γ's would always have smaller dead times, because of the continuous measurement. The three pulse gated ADC's were extremely busy just after the beam gate which was arriving 7 times during each super-cycle and therefore introduced a larger dead time. Due to this unreliability of the ADC the free running γ's were only used for comparison and check of the relative number of counts in the various peaks. A total energy spectrum from the pulse gated γ singles from histogram 501 is shown on page 61.

4.4.2 Analysis

From Section 4.3.3 we recall that the energy dependent efficiencies of the HPGe detector used in this experiment are:

$$\varepsilon_\gamma(E) = 10^{A \cdot log(E_\gamma)+B} \,, \tag{4.16}$$

and the corresponding estimated errors are:

$$\Delta\varepsilon_\gamma(E) = 7\% \cdot \varepsilon_\gamma \,. \tag{4.17}$$

Since the efficiency of the β detector was not investigated thoroughly during the experiment due to shortage of time some tests was performed in the analysis. In theory the branching ratio of the various γ decays could be calculated in the following way. The number of detected γ rays N_γ can be written as:

$$N_\gamma(E) = N_0 \cdot \varepsilon_\gamma(E) \cdot b_\gamma(E) \,, \tag{4.18}$$

where N_0 is the initial number of nuclei, $b_\gamma(E)$ the branching ratio to a specific state and $\varepsilon_\gamma(E)$ the efficiency determined by (4.16). The expected number of counts of β/γ coincidences can be written as:

$$N_{\beta\gamma} = N_0 \cdot \varepsilon_\gamma(E) \cdot \varepsilon_\beta \cdot b_\gamma(E) \,. \tag{4.19}$$

The number of detected β singles can be written in a similar manner as:

$$N_\beta = N_0 \cdot \varepsilon_\beta \,. \tag{4.20}$$

The experimentally observed branching ratio of a given transition can then be calculated by dividing (4.19) by (4.20):

$$\begin{aligned} \frac{N_{\beta\gamma}}{N_\beta} &= \frac{N_0 \cdot \varepsilon_\gamma(E) \cdot \varepsilon_\beta \cdot b_\gamma(E)}{N_0 \cdot \varepsilon_\beta} = \varepsilon_\gamma(E) \cdot b_\gamma(E) \\ &\Updownarrow \\ b_\gamma(E) &= \frac{N_{\beta\gamma}}{N_\beta \cdot \varepsilon_\gamma(E)} \,. \end{aligned} \tag{4.21}$$

The above is only true if the β efficiencies ε_β used in (4.19) and (4.20) are equal. Because of the way the setup was constructed with hardware β/γ coincidences this was not the case. The intrinsic part of the β efficiency used in the expression for the number of observed coincidences (4.19) contains a term $\varepsilon_C < 0$ describing the coincidence efficiency. This additional term is rather difficult to determine in a hardware coincidence setup as the one used in this experiment. Furthermore if dividing the number of β/γ coincidences by the number of γ singles using (4.19) and (4.18) and keeping (3.8) in mind:

$$\frac{N_{\beta\gamma}}{N_\gamma} = \frac{N \cdot b_\gamma(E)\varepsilon_\gamma(E) \cdot \varepsilon_\beta}{N \cdot b_\gamma(E) \cdot \varepsilon_\gamma} = \varepsilon_\beta = \varepsilon_{int} \cdot \Omega_\beta \,, \tag{4.22}$$

one should observe a constant value approximately equal to the solid angle of the β detector for the different γ energies. This is due to the fact that the intrinsic efficiency of the β detector normally can be assumed to be circa 100 % for β particles with energies above 100 keV. When using the previous

E_γ [keV]	$N_{\beta/\gamma}$ counts	ε_γ(E) [%]	b_γ(E) [%]
Run 8		$N_\beta = 189802 \pm 436$	
320	202.3±44.1	0.83±0.06	12.8±2.9
3368	74.8±7.5	0.104±0.007	37.9±4.6
Run 10+11+12		$N_\beta = 271492 \pm 521$	
320	354.0±41.6	0.83±0.06	15.7±2.2
3368	112.6±11.3	0.104±0.007	39.9±4.8

Table 4.9: Branching ratios

calculated solid angle of the β detector of 6.3 % , it shows out that the intrinsic efficiency was only about 53 % for the 320 keV transition and circa 31 % for the 3368 keV line. The cause of the coincidence efficiency being less than 1 can arise from several posible sources of error. One possibility could be that we observed too few β/γ coincidences. This could be the case if the thresholds on the CFD's were too high or if the optical connection from the light guide to the photo multiplier was bad. The other case could be that we observed too few γ singles instead. This could be caused by a too high threshold on ADC 2 which was converting the γ singles. The reason for the β efficiency not being constant for different energies is properly a combination of all these sources of error. The branching ratios calculated by (4.21) are listed in table 4.9. It should be emphasized that these values cannot be used for a precise comparison with earlier results, but can only show the observed order of magnitude. The relative intensities found here are, however, reliable.

4.5 Conclusion

Due to the unreliability of the results of the observed branching ratios in this experiment, the measurement was repeated in a new experiment performed, again at ISOLDE in July, 1994. The statistics were better in the 1993 experiment, but the coincidence setup was reliable and working in the proper way in the new experiment. I also participated in some of the analysis of the data from last experiment and further details can be read in reference [46]. Combining the new results with the γ singles from the 1993 experiment as a check resulted in the values listed in the rightmost column in table 4.10. For comparison, the results from two earlier experiments performed by C. D. Détraz *et al.*[27] and T. Björnstad *et al.*[12], are listed as well. Our values

E_γ [keV]	Energy Levels [keV] $E_i \longrightarrow E_f$	b_γ [%]		
		C. Détraz *et al.*	T. Björnstad *et al.*	Our results
219	6179.3 $\longrightarrow$ 5959.9 in ^{10}Be	0.95(35)	–	0.50(7)
320	320.0 $\longrightarrow$ 0.0 in ^{11}Be	5.2(14)	9.2(7)	6.3(6)
2592	5959.9 $\longrightarrow$ 3368.0 in ^{10}be	3.5(10)	–	7.9(12)
2811	6179.3 $\longrightarrow$ 3368.0 in ^{10}be	1.6(7)	–	0.47(13)
3368	3368.0 $\longrightarrow$ 0.0 in ^{10}be	21(6)	35(3)	29(3)

Table 4.10: γ branching ratios from the β decay of ^{11}Li.

agree quite well within the errors with the results measured by Détraz *et al.* But there exists some small differences of distinction. Their value for the 2811 keV transition differs more than two σ from our value, and this is probably

due to the fact of their low count statistics. On the other hand differs their value for the broad 2592 keV line more than several σ from our result. We believe that our result is more trust worthy duc to the deeper analysis of the origin of this transition (see Chapter 6). Additionally they had systematically uncertainties in their normalization.

There is no obvious reason for the discrepancy of our values to the results of T. Björnstad *et al.*. We performed more cross checks than they did, and due to the lack of branching ratios for the other transitions their obtained values are in all probability not correct.

The Doppler shift of the 2592 keV and 3368 keV lines will be treated in the next chapters together with the results from the neutron analysis.

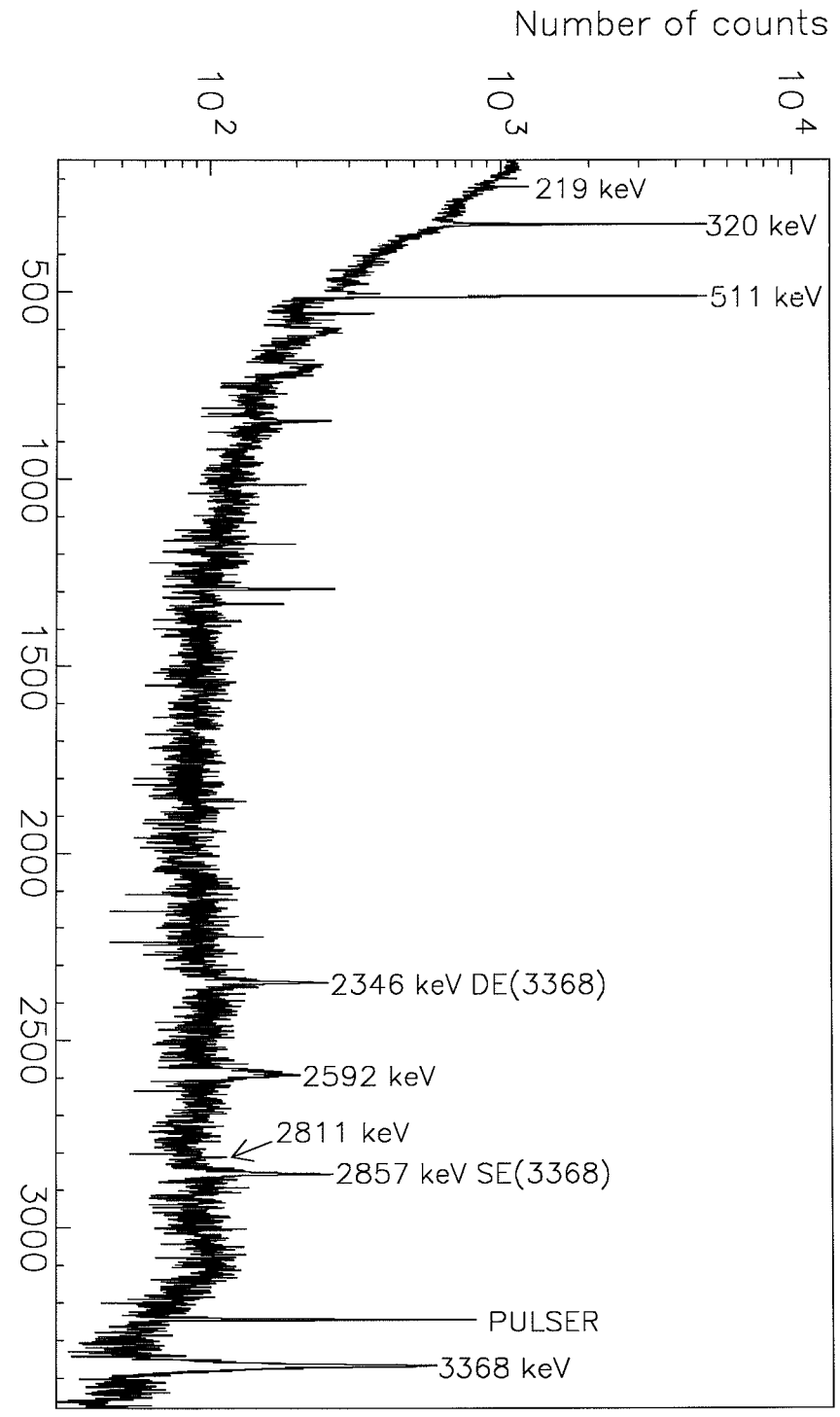

Figure 4.15: Full energy spectrum from the pulse gated γ singles histogram 501.

Chapter 5

β delayed neutron emission from ^{11}Li

5.1 The experiment

This experiment had two purposes: to investigate the β delayed emission of charged particles and to learn more about the β delayed neutron emission. The analysis described in this chapter will only treat the last part. As earlier mentioned this experiment was performed in October 1993 simultaneously with the γ experiment discussed in the previous chapter. There was 42 hours of ^{11}Li beam time and some hours of ^{9}Li calibration beam time, and we got approximately 300 lithium atoms per second in our collection point.

5.2 The setup

The setup was located at the end of the ISOLDE beamline LA1 (see figure 3.1). Around the setup some concrete elements were situated to prevent neutrons from the target to be detected in the neutron detectors in the setup. In direct line from the target hall a paraffin/cadmium[1] wall was situated to be completely sure that no neutrons from the target would reach the setup.

5.2.1 The experimental setup

The base point in the experimental setup was the vacuum chamber, which was connected to the ISOLDE common beam line system. Inside the chamber there was a small table where a collimator, a Faraday-cup and an annular plastic β detector were situated (see figure 5.1). At the end of the chamber

[1]The properties of neutron moderation of paraffin can be viewed in Section 3.2.2

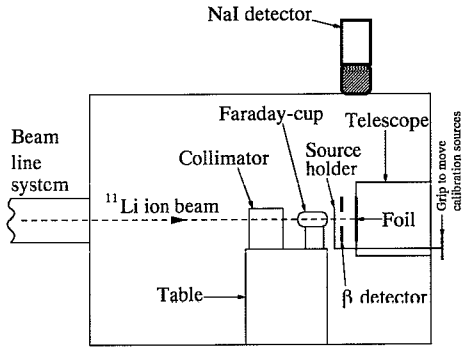

Figure 5.1: Side-view of the vacuum chamber.

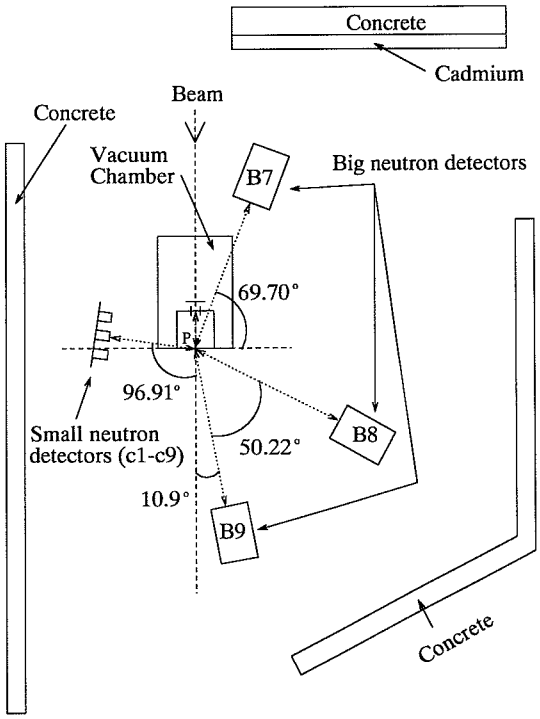

Figure 5.2: Sketch of the relative placement of the vacuum chamber and the neutron detectors. P is the fix point outside the vacuum chamber used for the distance measurements of the neutron detectors. The relative angles are indicated as well.

opposite to the beam entrance a gas telescope was placed. The ^{11}Li ions were implanted on the front foil of the telescope. Outside the chamber 12 neutron detectors were located; nine small neutron detectors in a frame with known mutual distances and three big barrel detectors placed as shown in figure 5.2.

5.2.2 The applied detectors

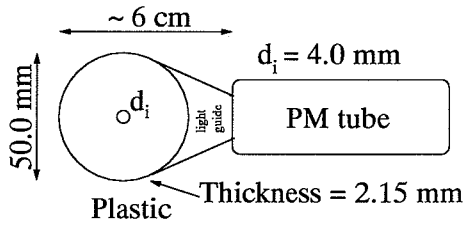

Figure 5.3: beta detector

The β detector was of the plastic scintillator type (described in Section 3.2.3). It consisted of a circular disk with a diameter of 50.0 mm and a thickness of 2.15 mm. In the center there was a hole with a diameter of 4.0 mm. The light from the scintillator material was guided by a light guide to the photo multiplier which was a PM HAMAMATSU E974-05. The active area of the β detector was covered by black adhesive tape, and to prevent charged particles from entering the telescope additional 0.5 mm aluminum was attached to the

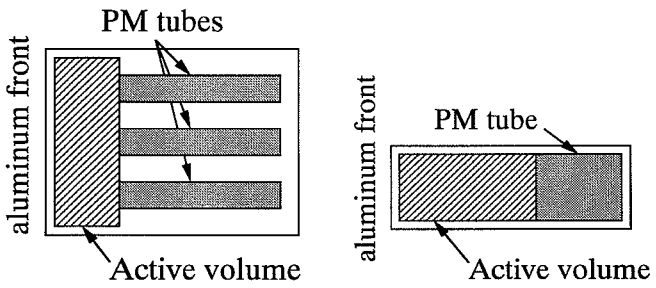

(a) Big barrel detectors.

(b) Small neutron detectors.

Figure 5.4: The applied neutron detectors.

detector. The distance from the center of the β detector to the front foil in the gas telescope was 4 mm.

Two different types of neutron detectors, both consisting of the liquid scintillator material NE213, was used. One type was three big barrel detectors with active volume diameter of 12" and thickness of 2". Each of the large neutron detectors used three separate photo multipliers, each having their own output connections (see figure 5.4a). The front aluminum plate had a thickness of 2 mm. Additionally nine small neutron detectors with an active volume diameter of 2" and a thickness of 4" were applied (see figure 5.4b). A sketch of the neutron detector positions can be viewed in figure 5.2. Detector B8 and B9 were moved during the run. The distances of the neutron detectors can be seen in table B.3 in Appendix B.

The NaI γ detector on top of the chamber was a standard type of detector, and the distance to the collection foil was circa 20 cm. The gas telescope housing was made of Teflon and the front foil was made of polypropylene with a thickness of 70 μg/cm^2 and a negligible aluminum layer[2] with a thickness of 200 Å.

5.2.3 The electronic setup

The electronic setup was very complicated due to the use of many multi channel CAMAC modules, and therefore only a rough sketch of the electronic modules used for one neutron detector, the NaI detector and the β detector is shown in figure 5.5. The outputs from the γ (NaI) and β were measured in *QDC1* and the *tail* and *full* amplitude output from the neutron detectors was registered in *QDC2*. The *TOF* spectra were obtained from the *TFC*. The Master Trigger was a combination of the β detector and a signal from either the NaI detector or a neutron detector.

5.2.4 Data files and spectra

Every event determined by the master trigger resulted in a storage of 48 parameters in the *GOOSY* event database. All parameters were directly connected to hardware signals from the electronic modules, i.e. no software created parameters. When requested the database was written directly to Exabyte tapes in the form of *LMD* files. The storage capacity of the tapes was ca. 1 Gb. To be able to use the data in *PAW* the files were converted into ntuple files which are briefly described in Section 3.4.2. During the conversion it is possible to choose the desired parameters to avoid very large data files.

[2]This layer was applied to prevent collection of static charge on the foil.

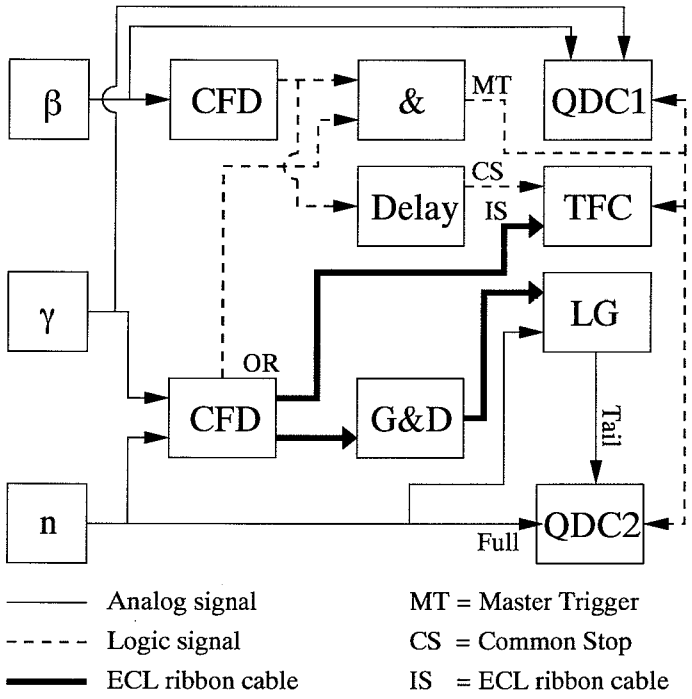

Figure 5.5: electronic setup

A ntuple file consisting of just enough parameters to be able to perform the analysis was created for every detector.

5.3 Calibrations

The calibration of the neutron detectors consists of two main parts: estimation of the energy thresholds of the different detectors and a TOF calibration. The thresholds shall be used when calculating the detector efficiencies and the TOF calibration is necessary to be able to convert the time spectra into energy spectra. The efficiency calibration is a part of this conversion.

5.3.1 Pulse Shape discrimination

As described in Section 3.2.2.2 neutron detectors are sensitive to both neutrons and γ rays. They can be resolved by filtering the output signals from the detectors. This procedure is as earlier mentioned called *Pulse Shape Discrimination.* The technique was applied to the signals from the detectors

used in this experiment, but worked only well for few detectors.

5.3.2 Threshold calibration

To be able to perform an efficiency calibration it is necessary to the know the lower energy thresholds of the amplitude spectra. Therefore an energy calibration of these spectra was made. In principle this was done by determining the positions of the Compton edges of the 3368 keV and 2125 keV[3] lines from the γ decay of ^{11}Be and ^{11}B. Additionally the two neutron lines with

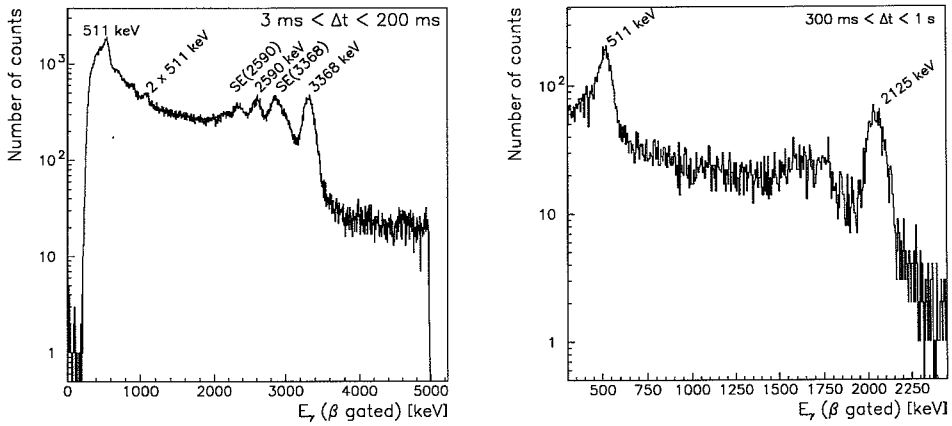

(a) Fast part.

(b) Slow part.

Figure 5.6: NaI spectra.

energies of ca. 2 and 3 MeV were applied as well. As seen in figure 5.6a the ratio between the amplitude of the 3368 keV line and the background following to the right of the peak is approximately 10:1 ; this results in a possible resolving of the Compton edge in the neutron amplitude spectra. The direct γ peak is not observed in the amplitude spectra, due to the worse resolution of the neutron detector compared to the NaI detector. A similar approach was performed for the γ line of 2125 keV from ^{11}B (see figure 5.6b). The kinetic energy of a Compton scattered electron is defined by[47, page106]:

$$T_{kin} = \frac{E_\gamma^2(1 - cos\theta_\gamma)}{m_e c^2 + E_\gamma(1 + cos\theta_\gamma)} \tag{5.1}$$

[3]This line was only used for the big barrel neutron detectors b7, b8 and b9

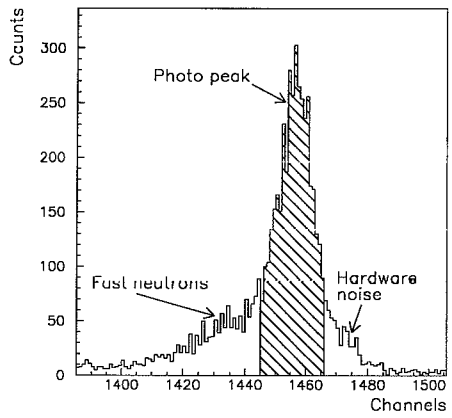

Figure 5.7: Narrow cut on the photo peak in the TOF spectra.

where E_γ is the energy of the incident photon, θ_γ the scattering angle and m_e the electron rest mass. The maximum kinetic energy is obtained when the photon is backscattered, i.e. $\theta_\gamma = 180°$. This energy is called the *Compton edge* and can be written as:

$$(T_{kin})_{max} = \frac{2E_\gamma^2}{m_e c^2 + 2E_\gamma} \tag{5.2}$$

Since the PSD technique did not provide any real opportunity to resolve

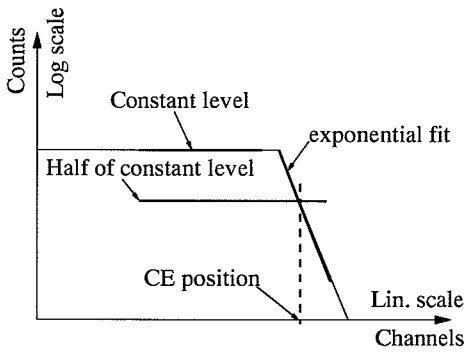

Figure 5.8: Sketch of pulse height CE fitting

the γ's and the neutrons from each other, another solution was used instead. The γ's were filtered from the TOF spectra (see figure 5.9) by introducing a

narrow cut on the photo peak. This was done for all detectors. These cuts were then applied to the amplitude spectra. A typical amplitude spectrum was shown in figure 3.6. The positions were calculated by some special fitting routines written for PAW. The routines work in principle by first determining the maximum constant level to the left of the edge, and then fitting the edge itself by an exponential. Where the half of the maximum and the exponential cross is the position of the Compton edge. This procedure was done for all detectors. A similar procedure was used when determining the pulse height positions for the 2 and 3 MeV neutrons with the only exception that the cuts in the TOF spectra were applied to the two neutron lines instead . With these values we could make an energy calibration and convert the obtained threshold positions from channels to energy. The Compton edge and neutron line positions can be viewed in table B.4.

5.3.3 Time Of Flight calibration

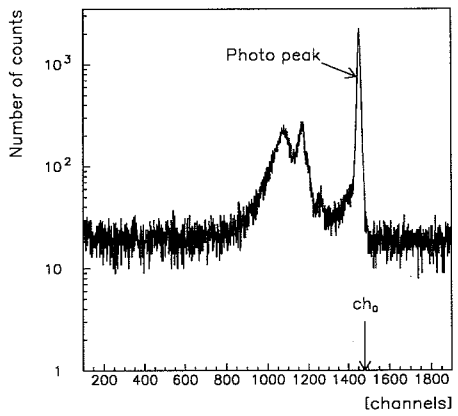

Figure 5.9: TOF spectrum from B7.

A typically TOF spectrum is shown in figure 5.9. It should be noted that C2 and C4 did not have any TOF spectra at all. To be able to convert the observed time of flight measurements to corresponding energies a determination of the zero point of the time scale is necessary. This also includes the calculation of the time resolution of the detectors, and was done by inserting an 8 ns cable for each neutron detector while collecting ^{9}Li. The shift of the photopeak measured in channels was equal to 8 ns, and the detector resolution R could thereby be calculated for each detector. The zero point can be

written as:

$$ch_0 = ch_\gamma + \frac{D}{c \cdot R} \tag{5.3}$$

where ch_γ is the photo peak position, D the distance from the telescope foil to the center of the neutron detector, c the speed of light and R the time resolution of the TOF spectra. The relativistic kinetic energy of a particle with rest mass m_0 traveling with a speed v is defined by[56, page 131]:

$$E_{kin} = m_0 c^2 \left(\frac{1}{\sqrt{1 - \left(\frac{v}{c}\right)^2}} - 1 \right) \tag{5.4}$$

The velocity of the neutrons in the TOF spectra can by using (5.3) be written as:

$$\begin{aligned} v = \frac{D}{\Delta t} &= \frac{D}{R(ch_0 - j)} \\ \Updownarrow & \\ \frac{v}{c} &= \left(\frac{ch_\gamma - ch_0}{ch_0 - j} \right) \end{aligned} \tag{5.5}$$

where j is the channel number corresponding to the time signal of a given neutron. When substituting (5.5) into (5.4) we get a distribution of the relativistic kinetic energies of the neutrons as a function of the channel numbers in the TOF spectra:

$$E = \left(\frac{1}{\sqrt{1 - \left(\frac{ch_0 - ch_\gamma}{ch_0 - j}\right)^2}} - 1 \right) m_n \tag{5.6}$$

where the neutron rest mass $m_n = 939.56563 \pm 0.00028 \mathrm{MeV/c^2}$[55]. When calculating the energies E_j and E_{j+1} for the corresponding channels j and $j+1$, they do not necessarily fit exactly into the bins of the energy spectrum, due to the unlinearity of the transformation. This was taken into account by distributing n counts from a given channel j in the TOF spectrum into the energy spectrum between the values E_j and E_{j+1} by a random function. When having very low statistics in a channel (less than 10 counts) this could change the spectrum to a lesser extent.

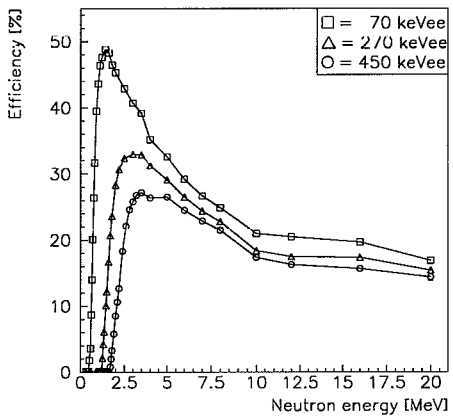

Figure 5.10: Neutron detector efficiency.

5.3.4 Efficiency calibration

The efficiency of the neutron detectors was calculated by a fortran program made by P. Désesquelles[26]. It exists in an early version called *DIAPHONY* and a present version called *MENATE*, which we used. It makes certain reservations for multiple scattering of the neutrons on the scintillator atoms (NE213) by a *Monte Carlo* simulation[25] and includes the corresponding cross sections. The output from the program is shown in figure 5.10 for the thresholds 70, 270 and 450 keVee. The obtained energy spectra for the neutrons should be divided by the efficiency distributions with thresholds depending on the energy range. We used the low amplitude thresholds for low neutron energy ranges and higher thresholds for higher neutron energies.

5.4 The ^{11}Li results

The obtained energy conversions and efficiencies from the previous sections were applied to all detectors with valid TOF spectra. In this rough analysis most attention has been payed to the data from the big barrel neutron detectors. A full energy (0.8-12.0 MeV) spectrum from detector B9 can be seen in figure 5.11. The applied efficiencies were calculated for the threshold of 70 keVee corresponding to 0.5 MeV in the neutron spectrum. One should notice that the main part of the statistics is obtained for neutron energies less than 5 MeV.

When the a nucleus β decays to an unstable level which again decays by

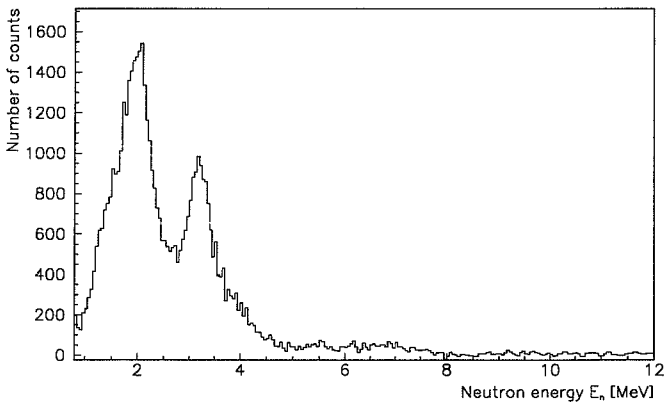

Figure 5.11: Full neutron energy spectrum.

particle emission a problem concerning the interpretation of the data appears. It is not *a priori* clear if the β decay and the decay of the unstable level can be treated separately or not. A more thoroughly discussion of this problem can be found in reference [52, Appendix A]. In principle one has to know the phase space factor or statistical rate function f discussed in Section 2.3.3 and defined in (2.8) and (2.9). f is often approximated by a parameterization which is valid for nuclear charges less than 101 and maximum β particle energies between 10 keV and 20 MeV:

$$f = f_{Z=0} \cdot exp\left[\sum_{n=0}^{3} a_n \cdot ln(E_0)^n\right] , \tag{5.7}$$

where $f_{Z=0}$ is from the expression (2.9) and the coefficients are tabulated in reference [67]. Then together with the phase space factor a Breit-Wigner function is fitted to the data for the various possible transitions by the use of level widths and energies from [1]. In theory one should be able to reconstruct the experimental spectrum by the sum of different Breit-Wigner fits. The procedure for doing this is first to fit the levels known so far and by close reference to possible new decays in the decay scheme try to construct the missing parts of the spectrum. In figure 5.12 the strongest decay channels have been fitted by this method, and the corresponding transitions are shown in the partial decay scheme in figure 5.13.

5.5 Conclusion

The contributions correspond very well with the result of the γ analysis and the work of Hans O. U. Fynbo[30] who has investigated the Doppler shift of the 2592 keV and 3368 keV γ decay transitions in ^{10}Be. The Doppler shift is due to the recoil of the ^{10}Be following the neutron emission of ^{11}Be. He

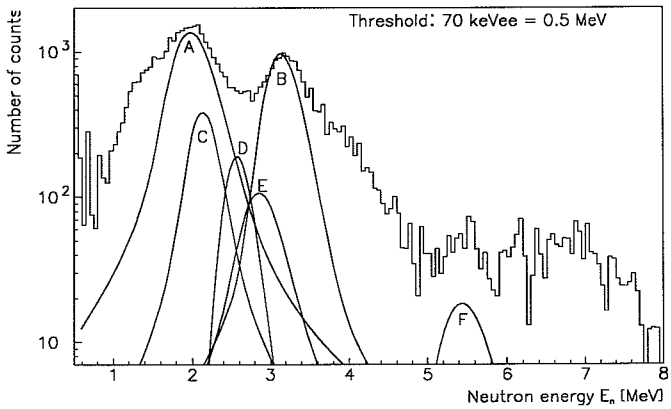

Figure 5.12: Fitted neutron spectrum.

both investigated the direct feeding and cascade feeding from higher lying levels. To the 2590 keV line only direct feeding from the 8816 keV state in ^{11}Be contributes. The corresponding branching ratio is approximately 8 %. The fit of the γ line is shown in 5.14 and the normalized contribution to the

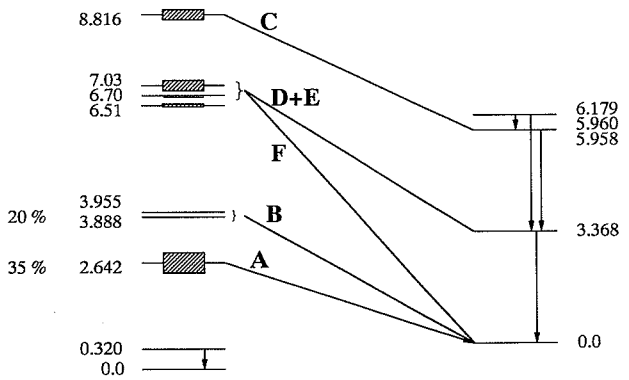

Figure 5.13: Part of decay scheme seen in this work.

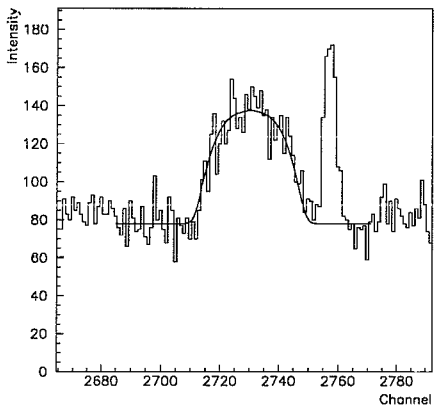

Figure 5.14: Doppler fit of the 2592 keV line.

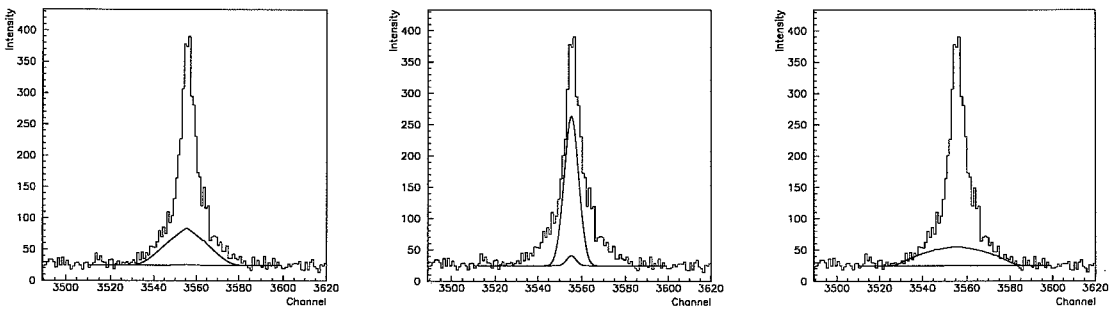

(a) Cascade feeding (b) Narrow direct feeding (c) Broad direct feeding

Figure 5.15: Shape contributions.

neutron spectrum is marked C in figure 5.12. For the 3368 keV line there are several contributions. The level in ^{10}Be at circa 6 MeV which emits the 2592 keV γ line contributes with the cascade feeding. The direct feeding consists of a narrow feeding arising from the level at about 3.9 MeV in ^{11}Be and a broad feeding from the level at about 6.9 MeV also in ^{11}Be with branching ratios of circa 14 % and 7 % , respectively. The former contribution is not observed in our data due to the very low neutron energy of about 200 keV which is equal

to only 4 bins in the neutron energy spectra. The latter contribution is equal to the transitions marked D and E in figure 5.12. The three contributions to the γ fit of the 3368 keV line can be viewed in figure 5.15 and the sum in figure 5.16.

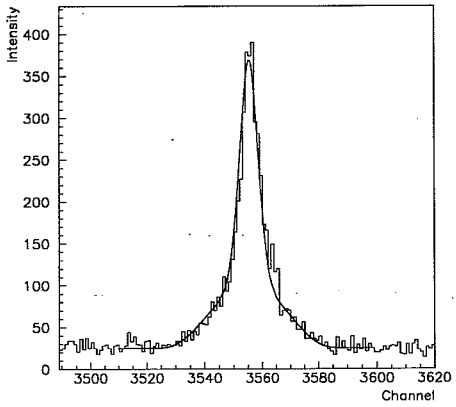

Figure 5.16: The sum of the shape contributions for the 3368 keV line.

Chapter 6

Summary

The experiment IS320 was performed at the ISOLDE facility at CERN, and the β delayed γ and particle emission from ^{11}Li was investigated. The γ part was analyzed and together with the data from a similar experiment performed in July, 1994 a determination of the branching ratios has been obtained. The branching ratio for the 320 keV γ line was found to be 6.3(6) % and the branching ratio for the 3368 keV line was found to be 29(3) %. These values are believed to be the most reliable so far. In the second part a preliminary analysis of the neutron emission was done, and it could be concluded that the main part of the activity arises from the two channels marked A and B in figure 5.13. When using the results from reference [30] it can, by normalization to the known γ parts of the total decay scheme, be shown that we know about 70-80 % of all neutron activity arising from the β decay of ^{11}Li, and that the transitions marked A and B contribute to the total number of neutrons by 20 % and 35 % , respectively. Even though the two analyses here in this thesis have been described separately, they have to be treated together when the more thoroughly analysis and decay scheme determination is going be done in the near future, where the knowledge about the β delayed charged particle emission[49] also will be included.

Chapter 7

Acknowledgments

I would like to thank:

My supervisor Karsten Riisager for introducing me to this very exciting field of research.
Björn Jonson and Göran Nyman for making me feel very welcome at CTH.
Maria J. Borge, Poul Hornshøj and Inmaculada Ramos Lerate for the fruitful co-work on the γ analysis.
Ivan Mukha and Martin Smedberg for the interesting co-work on the neutron analysis.
Thomas Nilsson for his indulgence towards my initial knowledge of electronics and for being a very good friend.
Haik Simon for trying to make me understand VMS and for teaching me German.
The rest of our collaboration not mentioned here.

My family and all my friends.

Especially I would like to thank Pia for her love and support, and for coping with me being absent minded during the preparation of this thesis.

Finally I want express my gratitude to my late mother, who always believed and supported me during my studies. I also want to express my thankfulness for her boundless love and devotion. Without her this thesis would never have been possible.

Torben Eilskov Leth

Appendix A

Fitting routines

A.1 Summation macro *SUM*

The syntax of the macro *sum.kumac* explained in Section 3.4.2.3 is like the following:

```
* Invoked by: PAW> exec sum #1
* argument: #1 = histogram number
* This macro calculates the number of
* counts in a chosen peak.
* It works with non-constant background.
* First it zoom´s into the desired peak.
* Finish with RIGHT MB.
* Then an interval left and right of the
* peak is chosen. The intervals determines
* the background estimation (can be linear).
* Finally the fit interval is chosen and
* finished with the RIGHT MB.
* There should be a hit 6 points with the
* mouse in the background and peak choice.
* It is crusial that the succession of the
* fit intervals are right. This version only
* works for histograms with less than 10000
* channels.

* Set some general options and plot
* the spectrum
opt zfl1
opt nsta
hi/pl [1]
*   Zoom into the desired peak
message ´Zoom into the desired peak and END
        with RIGHT mousebutton´
zoom
*   Choose the 3 intervals
ve/cre x(6)
ve/cre y(6)
message ´ ´
message ´Choose background left & right
        to the peak!´
message ´Then choose the sum interval and END
        with RIGHT mousebutton´
vlocate x y ´p´
*   Create the variables for the calculations
ve/cre xx(10000)
ve/cre xy(10000)
his/get/contents [1] xx
sigma xy = sumv(xx)
  x1 = $sigma(int(x(1)))
  x2 = $sigma(int(x(2)))
  x3 = $sigma(int(x(3)))
  x4 = $sigma(int(x(4)))
  x5 = $sigma(int(x(5)))
  x6 = $sigma(int(x(6)))
* Create real number interval numbers due
* to the way PAW treats vectors
  x5r = $sigma(x(5))
  x6r = $sigma(x(6))
ve/cre xxx(10000)
ve/cre yyy(10000)
ve/cre dyyy(10000)
* Create the LEFT interval as X and Y vectors
* with errors for Y
do i=1,[x2]-[x1]+1
        d = [i]+[x1]
        vec/inp xxx([i]) [d]
        vec/inp yyy([i]) xx([d])
        er = $sigma(sqrt(xx([d])))
        vec/inp dyyy([i]) [er]
enddo
* Append the RIGHT interval to the X and Y
* vectors with erros for Y
do i=[x2]-[x1]+2,[x4]-[x3]+[x2]-[x1]+3
        d = [i]+[x3]
        vec/inp xxx([i]) [d]
        vec/inp yyy([i]) xx([d])
```

```
        er = $sigma(sqrt(xx([d])))
        vec/inp dyyy([i]) [er]
enddo
* The number of points in the new
* background vectors
  fi = [x4]-[x3]+[x2]-[x1]+3
*   Fit the linear background
vec/cre PAR(2)
vec/cre ERRPAR(2)
vec/fit xxx(1:[fi]) yyy(1:[fi]) ! p1 0 2
        PAR ! ! ! ERRPAR
* Assign the results to kumac variables
  alpha = $sigma(PAR(2))
  beta = $sigma(PAR(1))
  dalpha = $sigma(ERRPAR(2))
  dbeta = $sigma(ERRPAR(1))
* Plot the fitted background
func/plot [alpha]*x+[beta] [x1] [x4] s
* Calculate the background under the
* peak and the error
  bg=0.5*([x6r]-[x5r])*([alpha]*
     ([x6r]+[x5r])+2*[beta])
  in=[x5r]-[x6r]
  t1=(-0.5*([x5r]-[x6r])*([x5]+[x6])*[dalpha])
  t2 = (([x6r]-[x5r])*[dbeta])
  dbg = $sigma(sqrt(([t1])**2+([t2])**2))
  fullarea = $sigma(xy([x6])-xy([x5]))
  dfullarea = $sigma(sqrt([fullarea]))
  area = [fullarea]-[bg]
  darea = $sigma(sqrt([dfullarea]**2+
          [dbg]**2))
* Illustrate the peak fit interval with
* vertical lines
line [x5r] 0 [x5r] 10000
line [x6r] 0 [x6r] 10000
*   Write the results on the plot
zone 1 1
selnt 1
TEXT 2.3 17.6 'ID' 0.19 ! 'L'
TEXT 2.3 17.2 'AREA' 0.19 ! 'L'
TEXT 2.3 16.8 'BG(TOT) UNDER PEAK' 0.19 ! 'L'
TEXT 2.3 16.4 '[a]' 0.19 ! 'L'
TEXT 2.3 16.0 '[b]' 0.19 ! 'L'
TEXT 7 17.6 [1] 0.19 ! 'R'
TEXT 7 17.2 [area] 0.19 ! 'R'
TEXT 7 16.8 [bg] 0.19 ! 'R'
TEXT 7 16.4 [alpha] 0.19 ! 'R'
TEXT 7 16.0 [beta] 0.19 ! 'R'
BOX 2  7.2 18.0 15.8
TEXT 13 17.6 'Summation fit' 0.19 ! 'L'
TEXT 13 17.2 'Error "a#' 0.19 ! 'L'
TEXT 13 16.8 'Error "a#' 0.19 ! 'L'
TEXT 13 16.4 'Error "a#' 0.19 ! 'L'
TEXT 13 16.0 'Error "a#' 0.19 ! 'L'
TEXT 17.9 17.2 [darea] 0.19 ! 'R'
TEXT 17.9 16.8 [dbg] 0.19 ! 'R'
TEXT 17.9 16.4 [dalpha] 0.19 ! 'R'
TEXT 17.9 16.0 [dbeta] 0.19 ! 'R'
BOX 12.8 18.0 15.8 18.0
TEXT 2 1 'FITNMIN' 0.19 ! 'L'
TEXT 6 1 [x5r] 0.25 ! 'R'
TEXT 14 1 'FITNMAX' 0.19 ! 'L'
TEXT 18 1 [x6r] 0.25 ! 'R'
selnt 10
text [x5r] 0 '"2' 0.3 ! 'C'
text [x6r] 0 '"2' 0.3 ! 'C'
*   Return to some general options
opt sta
```

A.2 Gaussian fitting routine *GFIT*

The following two subsections conatain the PAW macro and the fortran code for the Gaussian fitting routine *GFIT* explained in Section 3.4.2.1.

A.2.1 The PAW macro *gfit.kumac*

```
macro fit
shell gfit.out
opt nsta
vec/cre dummy(13) r
vec/read dummy gaussfit.dat
A=dummy(1)
B=dummy(2)
C=dummy(3)
D=dummy(4)
E=dummy(5)
F=dummy(6)
G=dummy(7)
H=dummy(8)
I=dummy(9)
J=dummy(10)
K=dummy(11)
L=dummy(12)
M=dummy(13)
N=[J]-[M]
O=[K]+[M]
hi/pl [I]([N]:[O])
func/plot .39894*[A]/[C]*exp(-0.5*(x-[B])**2
          /[C]**2)+[D] [N] [O] S
vec/del dummy
zone 1 1
selnt 1
```

```
TEXT 2.3 17.5 'ID' 0.25 ! 'L'
TEXT 2.3 17.0 'AREA' 0.25 ! 'L'
TEXT 2.3 16.5 'POSITION' 0.25 ! 'L'
TEXT 2.3 16.0 'SIGMA' 0.25 ! 'L'
TEXT 2.3 15.5 'BACKGROUND' 0.25 ! 'L'
TEXT 7 17.5 [I] 0.25 ! 'R'
TEXT 7 17.0 [A] 0.25 ! 'R'
TEXT 7 16.5 [B] 0.25 ! 'R'
TEXT 7 16.0 [C] 0.25 ! 'R'
TEXT 7 15.5 [D] 0.25 ! 'R'
BOX 2  7.2 18.0 15.3
TEXT 13 17.5 '[<V>^2]' 0.25 ! 'L'
TEXT 13 17.0 'Error' 0.25 ! 'L'
TEXT 13 16.5 'Error' 0.25 ! 'L'
TEXT 13 16.0 'Error' 0.25 ! 'L'
TEXT 13 15.5 'Error' 0.25 ! 'L'
TEXT 17.9 17.5 [L] 0.25 ! 'R'
TEXT 17.9 17.0 [E] 0.25 ! 'R'
TEXT 17.9 16.5 [F] 0.25 ! 'R'
TEXT 17.9 16.0 [G] 0.25 ! 'R'
TEXT 17.9 15.5 [H] 0.25 ! 'R'
BOX 12.8 18.0 15.3 18.0
TEXT 2 1 'FITNMIN' 0.25 ! 'L'
TEXT 5 1 [J] 0.25 ! 'R'
TEXT 15 1 'FITNMAX' 0.25 ! 'L'
TEXT 18 1 [K] 0.25 ! 'R'
selnt 10
text [J] 0 '"2' 0.3 ! 'C'
text [k] 0 '"2' 0.3 ! 'C'
opt sta
return
```

A.2.2 The fortran code *gfit.f*

```
      program gfit
      IMPLICIT DOUBLE PRECISION (A-H,O-Z)
      REAL SP1(0:4096)
      DIMENSION NSP(0:4096),ARGLIS(5),VAL(4),
     *ERROR(4)
      EXTERNAL FCN
      COMMON /PAWC/HMEMOR(8000)
      COMMON /SPP/NSP,NSPEC,NMIN,NMAX
      CHARACTER CHNAM*10
      WRITE(*,'(T8,A)') '** Fit of gamma
     *peaks **'
      WRITE(*,'(T8,A)') 'File: eff320.his'
      CALL HLIMIT(8000)
      LRECL = 1024
      CALL HROPEN(2,'IS320','eff320.his'
     *,' ',LRECL,ISTAT)
      WRITE(*,'(A,$)') ' Spectrum number: '
      READ(*,'(I4)') nspec
      CALL HRIN(NSPEC,0,0)
      CALL HUNPAK(NSPEC,SP1,' ',0)
      WRITE(*,'(A,$)') ' Min. channel for fit
     *region: '
      READ(*,'(I4)') NMIN
      WRITE(*,'(A,$)') ' Max. channel for fit
     *region: '
      READ(*,'(I4)') NMAX
      WRITE(*,'(A,$)') ' Approximate peak
     *position: '
      READ(*,'(I4)') npos
      do i=nmin,nmax
         nsp(i) = sp1(i)
      enddo
      CALL MNINIT(5,6,6)
      CALL MNSETI('Gaussfit of gamma peaks')
      CALL MNPARM(1,'area',1.D3,3.D2,0.D0,
     *0.D0,IERR)
      CALL MNPARM(2,'position',dble(npos),
     *1.D0,0.D0,0.D0,IERR)
      CALL MNPARM(3,'sigma',.9D0,.1D0,0.D0,
     *0.D0,IERR)
      CALL MNPARM(4,'background',5.D0,3.D0,
     *0.D0,0.D0,IERR)
      ARGLIS(1) = 1.D0
      CALL MNEXCM(FCN,'CALL FCN',ARGLIS,1,
     *IERR,FAC)
      ARGLIS(1) = 2.D0
      CALL MNEXCM(FCN,'FIX',ARGLIS,1,IERR,
     *FAC)
      ARGLIS(1) = 3.D0
      CALL MNEXCM(FCN,'FIX',ARGLIS,1,IERR,
     *FAC)
      CALL MNINTR(FCN,0)
      do num=1,4
      CALL MNPOUT(num,CHNAM,VAL(num),
     *ERROR(num),D1,D2,I1)
      enddo
      CALL MNSTAT(FMIN,D3,D4,D5,D6,D7)
      OPEN(1,ACCESS='SEQUENTIAL',
     *FILE='gaussfit.dat')
      do num=1,4
      WRITE(1,*) VAL(num)
      ENDDO
      DO num=1,4
      WRITE(1,*) ERROR(num)
      ENDDO
      WRITE(1,'(I4)') NSPEC
      WRITE(1,'(I4)') NMIN
      WRITE(1,'(I4)') NMAX
      WRITE(1,*) FMIN
      WRITE(1,'(I4)') (NMAX-NMIN)/2
      CLOSE(1)
      END
*****************************************
      SUBROUTINE FCN(NPAR,GRAD,FVAL,XVAL,
     *IFLAG,FAC)
      IMPLICIT DOUBLE PRECISION (A-H,O-Z)
      DIMENSION NSP(0:4096),GRAD(*),XVAL(*)
      COMMON /SPP/NSP,NSPEC,NMIN,NMAX
```

```
      SAVE
      fval = 0.
      do i=nmin,nmax
         th = xval(4) + xval(1)*
     *(dfreq((dble(i+1.5)-xval(2))/xval(3))-
     *dfreq((dble(i+0.5)-xval(2))/xval(3)))
        FVAL = FVAL + (NSP(I)-TH)**2/MAX(1,
     *NSP(I))
      enddo
      IF (IFLAG.EQ.3) THEN
         WRITE(*,'(A,I4,A,I4)')
     *    '   Min.ch: ',NMIN,'   Max.ch: '
     *,NMAX
      endif
      end
```

A.3 Lorentzian fitting routine *LFIT*

The next two subsections contain the two parts of the Lorentz fitting program. The mode of operation if briefly explained in Section 3.4.2.2.

A.3.1 The PAW macro *lfit.kumac*

```
macro fit
     shell lfit.out
     opt nsta
     ve/cre dummy(13) r
     ve/read dummy lorentz.dat
     A=dummy(1)
     B=dummy(2)
     C=dummy(3)
     D=dummy(4)
     E=dummy(5)
     F=dummy(6)
     G=dummy(7)
     H=dummy(8)
     I=dummy(9)
     J=dummy(10)
     K=dummy(11)
     L=dummy(12)
     M=dummy(13)
     N=[J]-[M]
     O=[K]+[M]
     hi/pl [I]([N]:[O])
func/plot [A]*([C]/6.283185)/((x-[B])**2+
          [C]**2/4)+[D] [N] [O] S
     ve/del dummy
zone 1 1
selnt 1

TEXT 2.3 17.5 'ID' 0.25 ! 'L'
TEXT 2.3 17.0 'AREA' 0.25 ! 'L'
TEXT 2.3 16.5 'POSITION' 0.25 ! 'L'
TEXT 2.3 16.0 'GAMMA' 0.25 ! 'L'
TEXT 2.3 15.5 'BACKGROUND' 0.25 ! 'L'
TEXT 7 17.5 [I] 0.25 ! 'R'
TEXT 7 17.0 [A] 0.25 ! 'R'
TEXT 7 16.5 [B] 0.25 ! 'R'
TEXT 7 16.0 [C] 0.25 ! 'R'
TEXT 7 15.5 [D] 0.25 ! 'R'
BOX 2  7.2 18.0 15.3
TEXT 13 17.5 '[<V>^2]' 0.25 ! 'L'
TEXT 13 17.0 'Error' 0.25 ! 'L'
TEXT 13 16.5 'Error' 0.25 ! 'L'
TEXT 13 16.0 'Error' 0.25 ! 'L'
TEXT 13 15.5 'Error' 0.25 ! 'L'
TEXT 17.9 17.5 [L] 0.25 ! 'R'
TEXT 17.9 17.0 [E] 0.25 ! 'R'
TEXT 17.9 16.5 [F] 0.25 ! 'R'
TEXT 17.9 16.0 [G] 0.25 ! 'R'
TEXT 17.9 15.5 [H] 0.25 ! 'R'
BOX 12.8 18.0 15.3 18.0
TEXT 2 1 'FITNMIN' 0.25 ! 'L'
TEXT 5 1 [J] 0.25 ! 'R'
TEXT 15 1 'FITNMAX' 0.25 ! 'L'
TEXT 18 1 [K] 0.25 ! 'R'
selnt 10
text [J] 0 '"2' 0.3 ! 'C'
text [k] 0 '"2' 0.3 ! 'C'
opt sta
return
```

A.3.2 The fortran code *lfit.f*

```
      program lfit
      IMPLICIT DOUBLE PRECISION (A-H,O-Z)
      REAL SP1(0:4096)
      DIMENSION NSP(0:4096),ARGLIS(5),
     *VAL(4),ERROR(4)
      EXTERNAL FCN
```

```
      COMMON /PAWC/HMEMOR(8000)
      COMMON /SPP/NSP,NSPEC,NMIN,NMAX
      CHARACTER CHNAM*10
      WRITE(*,'(T8,A)') '**  Fit of gamma
     *peaks **'
      CALL HLIMIT(8000)
      LRECL = 1024
      CALL HROPEN(2,'IS320','is320.his'
     *,' ',LRECL,ISTAT)
      WRITE(*,'(A,$)') ' Spectrum number: '
      READ(*,'(I4)') nspec
      CALL HRIN(NSPEC,0,0)
      CALL HUNPAK(NSPEC,SP1,' ',0)
      WRITE(*,'(A,$)') ' Min. channel for
     *fit region: '
      READ(*,'(I4)') NMIN
      WRITE(*,'(A,$)') ' Max. channel for
     *fit region: '
      READ(*,'(I4)') NMAX
      WRITE(*,'(A,$)') ' Approximate peak
     *position: '
      READ(*,'(I4)') npos
      do i=nmin,nmax
         nsp(i) = sp1(i)
      enddo
      CALL MNINIT(5,6,6)
      CALL MNSETI('Fit of gamma peaks in
     *Li11 decay')
      CALL MNPARM(1,'area',1.D3,3.D2,0.D0,
     *0.D0,IERR)
      CALL MNPARM(2,'position',dble(npos),
     *1.D0,0.D0,0.D0,IERR)
      CALL MNPARM(3,'gamma',7.D0,.1D0,0.D0,
     *0.D0,IERR)
      CALL MNPARM(4,'background',5.D0,3.D0,
     *0.D0,0.D0,IERR)
      ARGLIS(1) = 1.D0
      CALL MNEXCM(FCN,'CALL FCN',ARGLIS,1,
     *IERR,FAC)
      ARGLIS(1) = 2.D0
      CALL MNEXCM(FCN,'FIX',ARGLIS,1,IERR,
     *FAC)
      ARGLIS(1) = 3.D0
      CALL MNEXCM(FCN,'FIX',ARGLIS,1,IERR,
     *FAC)
      CALL MNINTR(FCN,0)
      do num=1,4
      CALL MNPOUT(num,CHNAM,VAL(num),ERROR(num),
     *D1,D2,I1)
      enddo
      CALL MNSTAT(FMIN,D3,D4,D5,D6,D7)
      OPEN(1,ACCESS='SEQUENTIAL',
     *FILE='lorentz.dat')
      do num=1,4
      WRITE(1,*) VAL(num)
      ENDDO
      DO num=1,4
      WRITE(1,*) ERROR(num)
      ENDDO
      WRITE(1,'(I4)') NSPEC
      WRITE(1,'(I4)') NMIN
      WRITE(1,'(I4)') NMAX
      WRITE(1,*) FMIN
      WRITE(1,'(I4)') (NMAX-NMIN)/2
      CLOSE(1)
      END
**************************************
      SUBROUTINE FCN(NPAR,GRAD,FVAL,XVAL,
     *IFLAG,FAC)
      IMPLICIT DOUBLE PRECISION (A-H,O-Z)
      DIMENSION NSP(0:4096),GRAD(*),XVAL(*)
      COMMON /SPP/NSP,NSPEC,NMIN,NMAX
      SAVE
      fval = 0.
      do i=nmin,nmax
         th = xval(4) + xval(1)*
     *    (xval(3)/6.283185)/((dble(i+0.5)-
     *xval(2))**2+xval(3)**2/4)
      FVAL = FVAL + (NSP(I)-TH)**2/
     *MAX(1,NSP(I))
      enddo
      IF (IFLAG.EQ.3) THEN
         WRITE(*,'(A,I4,A,I4)')
     *        '   Min.ch: ',NMIN,'
     *Max.ch: ',NMAX
      endif
      end
```

A.4 Efficiency fit program *eff_calib.f*

The fortran program used to perform the efficiency calculation fit for the germanium detector used in the experiment discussed in Chapter 4 is the following (a briefly overlook of the use of the program can be found in Section 3.4.3):

```
      PROGRAM LI11
*
*     Fit of efficiency in 11Li gamma
*     experiment data:
*     133ba_sum.dat 60co_sum.dat
*     56co_sum.dat 152eu_sum.dat
*     or  :
*     133ba_gauss.dat 60co_gauss.dat
*     56co_gauss.dat 152eu_gauss.dat
```

```
      DOUBLE PRECISION ARGLIS(5),error(4),
     *dummy
      DIMENSION Energy(26),Eff(26),Efe(26)
      INTEGER n


      EXTERNAL FCN
      COMMON /DATAlist/Energy(26),Eff(26),
     *Efe(26),hj(26)
      COMMON /MY/n


      CALL MNINIT(5,6,6)
      CALL MNSETI('Fit of gamma efficiency')
      CALL MNPARM(1,'a',-1.0D0,.1D0,
     *0.D0,0.D0,IERR)
      CALL MNPARM(2,'b',.3D0,.01D0,
     *0.D0,0.D0,IERR)
      CALL MNPARM(3,'co_off',1.D8,1.D7,
     *0.D0,0.D0,IERR)
      CALL MNPARM(4,'eu_off',1.D8,1.D7,
     *0.D0,0.D0,IERR)

      ARGLIS(1) = 1.D0
      CALL MNEXCM(FCN,'CALL FCN',ARGLIS,
     *1,IERR,FAC)
****  Fit of the absolute calibrated peaks
      n=6
      ARGLIS(1) = 3.D0
      ARGLIS(2) = 4.D0
      CALL MNEXCM(FCN,'FIX',ARGLIS,2,
     *IERR,FAC)
      CALL MNEXCM(FCN,'MINI',ARGLIS,0,
     *IERR,FAC)
      CALL MNEXCM(FCN,'MINOS',ARGLIS,0,
     *IERR,FAC)
      CALL MNERRS(1,error(1),dummy,dummy,
     *dummy)
      CALL MNERRS(2,error(2),dummy,dummy,
     *dummy)
**** Fit of the relative peaks
      n=17
      ARGLIS(1) = 1.D0
      ARGLIS(2) = 2.D0
      CALL MNEXCM(FCN,'FIX',ARGLIS,2,IERR,
     *FAC)
      ARGLIS(1) = 3.D0
      CALL MNEXCM(FCN,'REL',ARGLIS,1,IERR,
     *FAC)
      CALL MNEXCM(FCN,'MINI',ARGLIS,0,IERR,
     *FAC)
      CALL MNEXCM(FCN,'MINOS',ARGLIS,0,IERR,
     *FAC)
      CALL MNERRS(3,error(3),dummy,
     *dummy,dummy)
      n = 26
      ARGLIS(1) = 3.D0
      CALL MNEXCM(FCN,'FIX',ARGLIS,1,
     *IERR,FAC)
      ARGLIS(1) = 4.D0
      CALL MNEXCM(FCN,'REL',ARGLIS,1,
     *IERR,FAC)
      CALL MNEXCM(FCN,'MINI',ARGLIS,0,
     *IERR,FAC)
      CALL MNEXCM(FCN,'MINOS',ARGLIS,0,
     *IERR,FAC)
      CALL MNINTR(FCN,0)
      CALL MNERRS(4,error(4),dummy,
     *dummy,dummy)
      write (*,*) error(1),error(2),
     *error(3),error(4)
      END
****************************************
      SUBROUTINE FCN(NPAR,GRAD,FVAL,XVAL,
     *IFLAG,FUTIL)

      IMPLICIT DOUBLE PRECISION(A-H,O-Z)
      DIMENSION GRAD(*),XVAL(*),Energy(26),
     *Eff(26),Efe(26),hj(26)
      INTEGER n
      COMMON /DATAlist/Energy(26),Eff(26),
     *Efe(26),hj(26)
      COMMON /MY/n
      real dummy1,dummy2,dummy3
      data hj /26*1.d0/
      SAVE
      IF (IFLAG.EQ.1) THEN
***   133Ba
      open(22,'../calib/133ba_sum.dat',
     *status='old')
         do i=1,4
            read(22,*) dummy1,dummy2,dummy3
            write(*,*) dummy1,dummy2,dummy3
            Energy(i) = dble(dummy1)
            Eff(i) = dble(dummy2)
            Efe(i) = dble(dummy3)
         end do
         close (22)

***   60co
      open(22,'../calib/60co_sum.dat',
     *status='old')
         do i=5,6
            read(22,*) dummy1,dummy2,dummy3
            Energy(i) = dble(dummy1)
            Eff(i) = dble(dummy2)
            Efe(i) = dble(dummy3)
         end do
         close (22)

***   56co
      open(22,'../calib/56co_sum.dat',
     *status='old')
         do i=7,17
            read(22,*) dummy1,dummy2,dummy3
            Energy(i) = dble(dummy1)
            Eff(i) = dble(dummy2)
            Efe(i) = dble(dummy3)
         end do
         close (22)

***   152eu
      open(22,'../calib/152eu_sum.dat',
     *status='old')
```

```
         do i=18,26
            read(22,*) dummy1,dummy2,dummy3
            Energy(i) = dble(dummy1)
            Eff(i) = dble(dummy2)
            Efe(i) = dble(dummy3)
         end do
         close (22)

      ENDIF
      SUM = 0.d0
***   Offset for the 56Co source
      do i=7,17
         hj(i) = xval(3)
      enddo
***   Offset for the 152Eu source
      do i=18,26
         hj(i) = xval(4)
      enddo

      DO I=1,n
         EFT = 10**(xval(1)*log10(Energy(i))+
     * xval(2))
         SUM = SUM+(EFT*hj(i)-Eff(i))**2/
     *(Efe(i))**2
      enddo
      FVAL = SUM
      IF (IFLAG.EQ.3) THEN
      write(*,*)'      A           B
     * F1        F2'
      write(*,*)xval(1),Xval(2),xval(3),xval(4)
      write(*,*)'

      ENDIF
      END
```

Appendix B

Analysis results

B.1 γ analysis results

ID #	Spectrum Name	Run time ΔT (sec.)	Source	Comments
51	0_g.001	1200	^{106}Rh/^{106}Ru	too large cut-off at low energies
52	0_g.002	55620	^{106}Rh/^{106}Ru	ADC stopped during run
53	0_g.003	1486	^{106}Rh/^{106}Ru	without vacuum
54	0_g.004	36600	^{106}Rh/^{106}Ru	recalibration
70	0_g.020	448.	^{133}Ba	known source 2667RP
71	0_g.021	826.	^{60}Co	known source 2669RP
72	0_g.022	1265.	^{133}Ba	unknown source
73	0_g.023	7288.	^{56}Co	unknown soruce
74	0_g.024	4486.	^{56}Co	unknown source
75	0_g.025	997.	^{56}Co + ^{133}Ba	unknown source
76	0_g.026	7090.	^{152}Eu	unknown source
77	0_g.027	34745	^{106}Rh/^{106}Ru	unknown source
78	0_g.028	34745	^{106}Rh/^{106}Ru	unknown source
79	0_g.029	69223	^{106}Rh/^{106}Ru	while ^{125}Cs was collected

Table B.1: Histograms of γ singles. The spectra ID 70, 71 73 and 76 were used in the efficiency calibration

β/γ coincidences		γ singles		β singles		γ free running		Run	# of
ID #	Spectrum Name	ID #	Spectrum Name	ID #	Spectrum Name	ID #	Spectrum Name	Time [sec.]	P-Pulses
1	b-g.001	51	g.001	101	n1.001	151	n2.001	510±5	NA
2	b-g.002	52	g.002	102	n1.002	152	n2.002	7170±72	NA
3	b-g.003	53	g.003	103	n1.003	153	n2.003	12030±120	NA
4	b-g.004	54	g.004	104	n1.004	154	n2.004	4500±45	2120
5	b-g.005	55	g.005	105	n1.005	155	n2.005	4440±44	NA
6	b-g.006	56	g.006	106	n1.006	156	n2.006	NA	NA
7	b-g.007	57	g.007	107	n1.007	157	n2.007	NA	NA
8	b-g.008	58	g.008	108	n1.008	158	n2.008	3600±36	1755
9	b-g.009	59	g.009	109	n1.009	159	n2.009	3660±37	NA
10	b-g.010	60	g.010	110	n1.010	160	n2.010	2040±20	1001
11	b-g.011	61	g.011	111	n1.011	161	n2.011	2040±20	1001
12	b-g.012	62	g.012	112	n1.012	162	n2.012	1260±13	600
13	b-g.013	63	g.013	113	n1.013	163	n2.013	3600±37	NA
500	b-g.010 b-g.011 b-g.012	501	g.010 g.011 g.012	502	n1.010 n1.011 n1.012	503	n2.010 n2.011 n2.012	5340±53	2602

Table B.2: Histograms contained in the file "is320.his" .

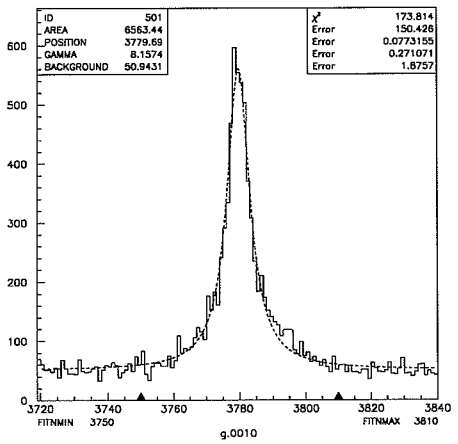

Figure B.1: Fit output from *lfit.kumac* for the 3368 keV γ line in histogram 501.

B.2 Neutron analysis results

Detector	Photo peak [channel]	$Dist_C$ [cm]	$Dist_S$ [cm]	Resolution R [ps/channel]
c1	1666.61±0.06	57.9	53.2	132.6±1.3
c3	1279.14±0.09	56.3	51.3	129.8±1.0
c5	1705.22±0.07	55.9	50.9	129.7±1.7
c6	1622.96±0.08	59.6	54.9	135.4±1.8
c7	1732.90±0.08	56.5	51.6	131.8±3.0
c8	1674.15±0.09	57.2	52.3	131.8±1.9
c9	1721.40±0.10	62.6	58.2	130.2±1.7
b7	1455.91±0.04	100.9	97.6	130.7±0.5
b8	1418.77±0.04	104.0	100.6	133.6±0.6
Run 8-17	-	211.5	208.1	-
Run 18-25	-	102.6	99.2	-
b9	1481.31±0.06	105.1	101.7	133.9±1.6
Run 18-25	-	186.1	182.7	-

Table B.3: Neutron detector properties.

Det.	Pos. of 1.939 MeV neutron line [ch]	Pos. of 3.072 MeV neutron line [ch]	Pos. of 2125 keV Compton edge [ch]	Pos. of 3368 keV Compton edge [ch]
c1	101.0±1.0	193.0±3.0	#	415.7±5.2
c2	#	#	#	#
c3	86.2±0.4	167.6±0.8	#	456.9±3.5
c4	#	#	#	#
c5	115.5±0.9	196.9±1.9	#	419.4±4.7
c6	97.1±0.5	200.2±0.5	#	492.4±4.5
c7	84.5±0.5	138.1±1.1	#	405.9±4.1
c8	85.2±0.9	90.9±1.0	#	206.8±3.8
c9	83.6±0.5	141.6±1.5	#	342.2±3.2
b7	117.1±1.0	202.4±0.9	338.3±5.5	508.0±2.3
b8	116.0±1.1	207.4±0.7	326.4±9.8	466.6±4.2
b9	115.0±1.0	195.6±2.2	281.6±7.6	426.9±3.4

Table B.4: Threshold positions in amplitude spectra.

Appendix C

Additional subjects

C.1 The Liquid Drop nuclear model

The differential cross section for the elastic scattering of neutrons on vaious nuclei can be written as[1]:

$$\frac{\mathrm{d}\sigma}{\mathrm{d}\Omega} \approx \frac{k^2R^2}{4}\left[1-\frac{1}{2}\left(\frac{kR\theta}{2}\right)^2\right]^2 \tag{C.1}$$

where k is the incident wave number, R the radius of the nucleus and θ the angular spread of the scattering. This is also called the *Black Sphere* model[61, Chapter 3]. Equation (C.1) has a minimum at:

$$\theta_{min} \approx \frac{5\pi}{4kR} \tag{C.2}$$

and by observing when the diffraction pattern falls off (θ_{min}) in scattering experiments, it is possible to estimate the radius of the target nucleus. The nuclear volume Ω_r can be estimated from this kind of experiments for various nuclei to be:

$$\Omega_r = \frac{4}{3}\pi R^3 = \frac{4}{3}\pi\left(\frac{4k\theta_{min}}{5\pi}\right)^{-3} \tag{C.3}$$

and it turns out that Ω_r is roughly proportinal to the number of nucleons in the nucleus:

$$\Omega_r = \Omega_0 A \tag{C.4}$$

[1]It is assumed that $kR\theta \ll 1$

or

$$R = r_0 A^{\frac{1}{3}} \tag{C.5}$$

where $r_0 \approx 1.25$ fm and $\Omega_0 \approx 9$ fm^3. This radius is called the *Liquid Drop* radius, due to the similar porportinality of volume and number of water molecules in a liquid drop. This is however complete opposite to atomic physics; where f. ex. the aluminum atom is ca. 10 times lighter than the lead atom, but they have similar sizes.

C.2 The Gaussian distribution and FWHM

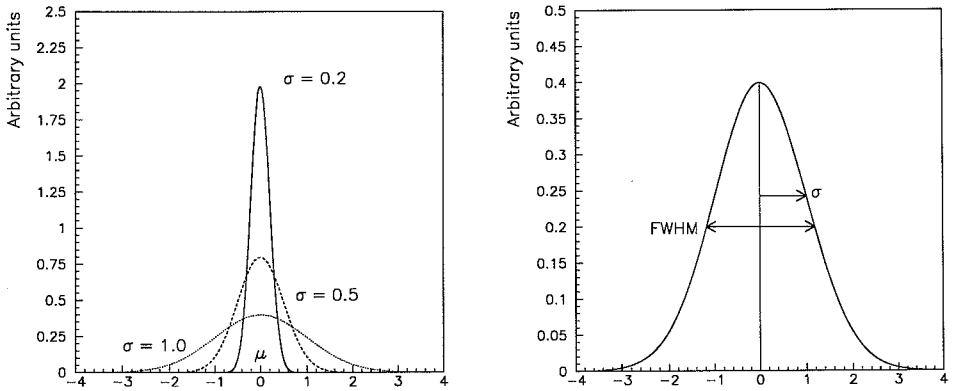

(a) The Gaussian distribution for various σ, which determines the width of the distribution.

(b) Relation between the standard deviation σ and the *FWHM*.

Figure C.1: The behavior of the Gaussian distribution and the connection to FWHM.

The *Gauusian* or *normal* distribution is often used for describing measurement errors and in particular instrumental errors. If applied under conditions where it is not strickly correct it newer the less provides a good approximation to the true distribution. The normalized Gaussian distribution is defined by[45, Chapter 4]:

$$G(E) = \frac{1}{\sigma\sqrt{2\pi}} e^{\left(-\frac{(x-\mu)^2}{2\sigma^2}\right)} \tag{C.6}$$

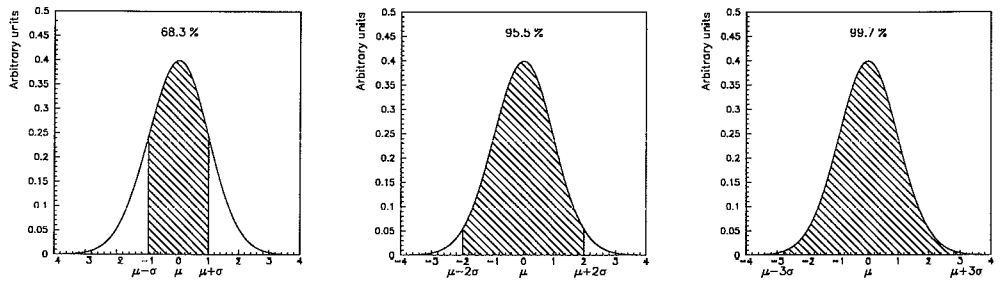

(a) $\mu \pm \sigma$ (b) $\mu \pm 2\sigma$ (c) $\mu \pm 3\sigma$

Figure C.2: The area contained between the three indicated limits in a Gaussian distribution.

It can be shown that μ and σ^2 correspond to the mean and variance of the distribution. Figure C.1a shows the distribution for different values of σ, which determines the width of the distribution. The standard deviation σ is the half width of the peak at about 60 % of the full amplitude. In physics another quantity is often used instead when describing the width. It is called the *Full Width Half Maximum* and as the name designates it is the full width of the peak at the half of the maximum amplitude. It can easily be shown that the relation between FWHM and σ is:

$$\text{FWHM} = 2\sigma\sqrt{2\ln 2} = 2.35\sigma \tag{C.7}$$

and this is illustrated in figure C.1b. The area under the Gaussian between integral intervals of σ should be kept in mind when interpreting measurement errors. The interval $x \pm \sigma$ signifies that the true value has ca. 68 % probability of lying between the limits $x - \sigma$ and $x + \sigma$ or a 95 % probability of lying between $x - 2\sigma$ and $x + 2\sigma$, etc (see figure C.2). The first interval is often chosen as the significant interval and called the 1σ interval. Values lying outside this interval are not considered as true values.

C.3 "Law" of propagating errors

When calculating errors of quantities depending on other measured quantities we have to use the "Law" of propagating errors. We consider a quantity $u = f(x, y)$ where x and y are quantities having errors σ_x and σ_y, respectively. For simplicity only a function of two variables is considered, but it is straight

forward to extend the number of variables. We then want to calculate the standard deviation σ_u as a function of σ_x and σ_y. The moment (mean) about zero can in general be defined as[45, chapter 4]:

$$\mu = E[x] = \int xP(x)dx \tag{C.8}$$

where $P(x)$ is the probability distribution. The *second central moment* can be written as:

$$\sigma^2 = E[(x-\mu)^2] = \int (x-\mu)^2 P(x)dx \tag{C.9}$$

and the *covariance* can be expressed by:

$$cov(x,y) = E[(x-\mu_x)(y-\mu_y)] \tag{C.10}$$

where μ_x and μ_y are the means of x and y respectively. We can now write σ^2 as:

$$\sigma_\mu^2 = E[(u-\overline{u})^2] \tag{C.11}$$

To first order, the mean $\overline{u}$ may be approximated by $f(\overline{x},\overline{y})$. This can be shown by expanding $f(x,y)$ about $(\overline{x},\overline{y})$. We now expand $(u-\overline{u})$ to first order in terms of x and y:

$$(u-\overline{u}) \simeq (x-\overline{x}) \left.\frac{\partial f}{\partial x}\right|_{\overline{x}} + (y-\overline{y}) \left.\frac{\partial f}{\partial y}\right|_{\overline{y}} \tag{C.12}$$

Taking the square of (C.12) and substituting into (C.11) then yields:

$$E[(u-\overline{u})^2] \simeq E\left[(x-\overline{x})^2\left(\frac{\partial f}{\partial x}\right)^2 + (y-\overline{y})^2\left(\frac{\partial f}{\partial y}\right)^2 + 2(x-\overline{x})(y-\overline{y})\frac{\partial f}{\partial x}\frac{\partial f}{\partial y}\right] \tag{C.13}$$

Using that the expectation value E of a sum is the expectation values of the addends, and making use of (C.8), (C.9) and (C.10) we find:

$$\sigma^2\mu \simeq \left(\frac{\partial f}{\partial x}\right)^2 \sigma_x^2 + \left(\frac{\partial f}{\partial y}\right)^2 \sigma_y^2 + 2cov(x,y)\frac{\partial f}{\partial x}\frac{\partial f}{\partial y} \tag{C.14}$$

The errors therefor are added quadratically with a modifying term due to the covariance. Depending on the sign and magnetude, the covariance term can increase or decrease the errors by dramatic amounts. Very often most

measurements in physics experiments are independent and the covariance term will become zero. (C.14) then reduces to a simple sum of squares. Correlations can arise when two or more parameters are extracted from the same set of measured data. While the raw data points are independent, the parameters are often correlated. When applying this error calculation method to parameters resulting from a fit, one has to know the correlation matrix to be able to use several of the parameters in the same calculations.

References

[1] F. Ajzenberg-Selove. *Energy levels of light nuclei A=11-12. Nuclear Physics A*, 506:1–158, 1990.

[2] M. Albrow, R. Billinge, F. Dydak, B. Jonson, and A. Richter. *The ISOLDE facility at the PS Booster. CERN/PSCC*, 89:29, 1989.

[3] R. Anne, S. E. Arnell, R. Bimbot, H. Emling, D. Guillemaud-Mueller, P. G. Hansen, L. Johannsen, B. Jonson, M. Lewitowicz, S. Mattsson, A. C. Mueller, R. Neugart, G. Nyman, F. Pougheon, A. Richter, K. Riisager, M. G. Saint-Laurent, G. Schrieder, O. Sorlin, and K. Wilhelmsen. *Observation of forward neutrons from the break-up of the ^{11}Li neutron halo. Physics Letters B*, 250(1,2):19–23, 1990.

[4] E. Arnold, J. Bonn, R. Gegenwart, W. Neu, R. Neugart, E.-W. Otten, G. Ulm, and K. Wendt. *Nuclear spin and magnetic moment of ^{11}Li. Physics Letters B*, 197:311, 1987.

[5] N. W. Ashcroft and N. D. Mermin. *Solid state physics.* W. B. Sounders Company, internal edition edition, 1976.

[6] G. Audi and A. H. Wapstra. *The 1993 atomic mass evaluation(II). Nuclear Physics A*, 565:1–65, 1993.

[7] R. E. Azuma, T. Björnstad, H. Å. Gustafsson, P. G. Hansen, B. Jonson, S. Mattsson, G. Nyman, A. M. Poskanzer, and H. L. Ravn. *Beta-delayed three-neutron radioactivity of ^{11}Li. Physics Letters*, 96B(1,2):31–34, 1980.

[8] R. E. Azuma, L. C. Carraz, P. G. Hansen, B. Jonson, K.-L. Kratz, S. Mattsson, G. Nyman, H. Ohm, H. L. Ravn, A. Schröder, and W. Ziegert. *First observation of beta-delayed two-neutron radioactivity: ^{11}Li. Physical Review Letters*, 43(22):1652–1654, 1979.

[9] A. Balfour and D. H. Marwick. *Programming in standard FORTRAN 77.* Heinemann Educational Books, London, 1987. first printed in 1979.

[10] H. Behrens and W. Bühring. *Electron radial wave functions and nuclear beta-decay.* Clarendon Press, Oxford, UK, 1st edition, 1982.

[11] C. A. Bertulani, L. F. Canto, and M. S. Hussein. *The structure and reactions of neutron-rich nuclei. Physics Reports*, 226:281–376, 1993.

[12] T. Björnstad, H. Å. Gustafsson, P. G. Hansen, B. Jonson, V. Lindfors, S. Mattsson, A. M. Poskanzer, H. L. Ravn, and T. I. collaboration. *Delayed neutron emission probabilities of ^{9}Li and ^{11}Li. Nuclear Physics A*, 359:1–8, 1981.

[13] T. Björnstad, E. Hagebø, P. Hoff, O. C. Jonsson, E. Kugler, H. L. Ravn, S. Sundell, B. Vosicki, and the ISOLDE Collaboration. *Methods for production of intense beams of unstable nuclei: New developments at ISOLDE. Physica Scripta*, 34:578–590, 1986.

[14] B. Blank, J. J. Gaimard, H. Geissel, K. H. Schmidt, H. Stelzer, K. Sümmerer, D. Bazin, R. D. Moral, J. P. Dufour, A. Fleury, F. Humbert, H. G. Clerc, and M. Steiner. *Charge-changing cross sections of the neutron-rich isotopes $^{8,9,11}Li$. Zeitschrift für Physik A*, 343:375–379, 1992.

[15] A. Bohr and B. R. Mottelson. *Nuclear structure*, volume 1. W. A. Benjamin, Inc, New York, USA, 1st edition, 1969.

[16] P. Bopp, D. Dubbers, L. Hornig, E. Klemt, J. Last, H. Schütze, S. J. Friedman, and O. Schärpf. *Beta-decay asymmetry of the neutron and g_A/g_V. Physical Review Letters*, 56(9):919–922, 1986.

[17] M. J. G. Borge, J. Deding, P. G. Hansen, B. Jonson, G. M. Pinedo, P. Møller, G. Nyman, A. Poves, A. Richter, K. Riisager, O. Tengblad, and the ISOLDE Collaboration. *Beta-decay to the proton halo state in ^{17}F. Physics Letters B*, 317:25–30, 1993.

[18] R. Brun, O. Couet, C. Vandoni, and P. Zanarina. *Physics Analysis Workstation (PAW) Libery Long Writeup Q121.* CERN Geneva, Switzerland, February 1995.

[19] CN Division, CERN Geneva, Switzerland. *CERN Program Library - Short Writeups*, June 1993.

[20] CN Division, CERN Geneva, Switzerland. *MINUIT - Reference Manual - Library Long Writeup D506*, February 1993. vers. 94.1.

[21] CN Division, CERN Geneva, Switzerland. *HBOOK - Reference manual - Library Long Writeup Y250*, January 1995. vers. 4.22.

[22] F. A. Cotton, G. Wilkinson, and P. L. Gaus. *Basic inorganic chemistry.* John Wiley & Sons, New York, 2nd edition, 1987.

[23] M. Cronqvist, B. Jonson, T. Nilsson, G. Nyman, K. Riisager, H. A. Roth, Ö. Skeppstedt, O. Tengblad, and K. Wilhelmsen. *Experimental determination of cross-talk between neutron detectors. Nuclear Instruments and Methods in Physics Research*, 317A:273–280, 1992.

[24] K. Debertin and G. Richard. *Gamma- and x-ray spectrometry with semiconductor detectors.* North-Holland, Amsterdam, 1988.

[25] P. Désesquelles. Private communication. ISN, Grenoble, France, December 1995.

[26] P. Désesquelles, A. J. Cole, A. Dauchy, A. Giorni, D. Heuer, A. Lleres, C. Morand, J. Saint-Martin, P. Stassi, J. B. Viano, B. Chambon, B. Cheynis, and D. Drain. *Cross talk and diaphony in neutron detectors. Nuclear Instruments and Methods in Physics Research*, A307:366–373, 1991.

[27] C. Détraz, D. Guillemaud, M. Langevin, F. Naulin, M. Epherre, R. Klapisch, M. de Saint-Simon, C. Thibault, and F. Touchard. *The γ activity from ^{11}Li beta decay. J. Physique - LETTRES*, 41(19):459–461, 1980.

[28] EG&G ORTEC, Oak Ridge, USA. *Modular pulse-processing electronics and semiconductor radiation detectors*, 1995.

[29] H. G. Essel. *GOOSY Manual.* GSI, Darmstadt, Germany, June 1988. vers. 1.2.

[30] H. O. U. Fynbo. Doppler broadened peaks, unpublished. IFA, Aarhus University, Denmark, December 1995.

[31] P. G. Hansen. Nuclear structure at the drip lines. *Nuclear Physics*, A553:89c–106c, 1993.

[32] P. G. Hansen, A. S. Jensen, and B. Jonson. Nuclear halos. In *Annual review of nuclear and particle science*, volume 45. 1995. to be published.

[33] P. G. Hansen and B. Jonson. The neutron halo of extremely neutron-rich nuclei. *Europhysics letters*, 4:409–414, 1987.

[34] R. Hofstadter. Alkali halide scintillation counters. *Physical Review*, 74:100–101, 1948.

[35] F. Humbert. *Kinematisch vollständige Messung der Aufbruchreaktionen von leichten, neutronenreichen Kernen am Beispiel des Halokerns ^{11}Li.* PhD thesis, Technische Hochschule, Darmstadt, Gernamny, 1995. not published.

[36] Y. Jading and K. Riisager. Systematic errors in χ^2-fitting of poisson distributions. *Nuclear Instruments and Methods in Physics Research*, A, 1996. in press.

[37] L. Johannsen. *The halo of ^{11}Li.* PhD thesis, IFA, Aarhus University, Denmark, 1990. not published.

[38] B. Jonson, H. Å. Gustafsson, P. G. Hansen, P. Hoff, P. O. Larsson, S. Mattsson, G. Nyman, H. L. Ravn, and D. Schardt. Beta-delayed two-neutron and three-neutron emission. In *4th international conference on nuclei far from stability*, pages 265–275, L. O. Skolen, Helsingør, Denmark, June 1981. CERN.

[39] B. Jonson, H. L. Ravn, and G. Walter. *ISOLDE PS Booster facility at CERN: experiments with slow radioactive beams. Nuclear Physics News*, 3(2):5–16, 1993.

[40] G. F. Knoll. *Radiation detection and measurement.* John Wiley & Sons, New York, second edition, 1989.

[41] K. S. Krane. *Introductory nuclear physics.* John Wiley & Sons, New York, rev. edition, 1988.

[42] E. Kugler, D. Fiander, B. Jonson, H. Haas, A. Przewloka, H. L. Ravn, D. J. Simon, K. Zimmer, and the ISOLDE Collaboration. *The new CERN-ISOLDE on-line mass-separator facility at the PS-Booster. Nuclear Instruments and Methods in Physics Research*, B(70):41–49, 1992.

[43] M. Langevin, C. Détraz, M. Epherre, D. Guillemaud-Mueller, B. Jonson, C. Thibault, and the ISOLDE Collaboration. Observation of β-delayed triton emission. *Physics Letters*, 146B(3,4):176–178, 1984.

[44] M. Langevin, C. Détraz, D. Guillemaud-Mueller, F. Naulin, M. Epherre, R. Klapisch, S. K. T. Mark, M. de Saint-Simon, C. Thibault, and F. Touchard. *β-delayed charged particles from ^{9}Li and ^{11}Li. Nuclear Physics*, A366:449–460, 1981.

[45] W. R. Leo. *Techniques for nuclear and particle physics experiments.* Springer-Verlag, Berlin, Germany, 2nd edition, 1994.

[46] I. R. Lerate. *Estudio de la radiación gamma emitida tras la desintegración beta del núcleo de 11-Li.* Master's thesis, trabajo de investigación, Cádiz, Spain, 1996. not published.

[47] P. Marmier and E. Sheldon. *Physics of nuclei and particles*, volume 1. Academic Press, New York, 1969.

[48] D. J. Millener, J. W. Olness, E. K. Warburton, and S. S. Hanna. *Strong* E1 *transitions in* ^{9}Be, ^{11}Be *and* ^{13}C. *Physical Review C*, 28(2):497–505, 1983.

[49] I. Mukha, M. J. G. Borge, D. Guillemaud-Mueller, P. Hornshøj, F. Humbert, B. Jonson, T. E. Leth, G. M. Pinedo, T. Nilsson, G. Nyman, K. Riisager, G. Schrieder, M. H. Smedberg, O. Tengblad, K. W. Rolander, and the ISOLDE collaboration. Observation of the ^{11}li(β-d) decay. *Physics Letter B*, 367:65, 1996.

[50] T. Nilsson. *Development of an energy-loss detector for charged particles.* Master's thesis, CTH, Göteborg, Sweden, 1989. not published.

[51] The nobel foundation. World Wide Web. http://www.nobel.se.

[52] G. Nyman, R. E. Azuma, P. G. Hansen, B. Jonson, P. O. Larsson, S. Mattsson, A. Richter, K. Riisager, O. Tengblad, K. Wilhelmsen, and the ISOLDE Collaboration. *The beta decay of* ^{9}Li *to levels in* ^{9}Be*: A new look. Nuclear Physics A*, 510:189–208, 1990.

[53] E. M. Pell. *Effect of Li-B ion pairing on* LI^{+} *ion drift in Si. Journal of Applied Physics*, 31(9):1675–1679, 1960.

[54] J. C. Philippot. Automatic processing of diode spectrometry. *IEEE, Transactions on nuclear science*, 17(3):446–488, 1970.

[55] *Review of particle properties*, volume 204 of *Physics Letters B*, 1988.

[56] R. Resbick. *Introduction to special relativity.* John Wiley & Sons, New York, 1968.

[57] K. Riisager. Nuclear halo states. *Reviews of modern physics*, 66(3):1105–1116, July 1994.

[58] E. Roeckl, P. F. Dittner, C. Détraz, R. Klapisch, C. Thibault, and C. Rigaud. *Decay properties of neutron-rich isotopes, ^{11}Li and $^{27-31}Na$.* *Physical Review C*, 10(3):1181–1188, 1974.

[59] K. W. Rolander. *β-decay of light neutron rich nuclei.* Licentiate thesis, CTH, Göteborg, Sweden, 1991. not published.

[60] K. W. Rolander. *Neutron halo nuclei.* PhD thesis, CTH, Göteborg, Sweden, 1993. not published.

[61] P. J. Siemens and A. S. jensen. *Elements of nuclei - Many-body physics with the strong interaction.* Addison Wesley, Redwood City, California, USA, 1987.

[62] H. Simon. Untersuchung an einem magnetspektrometer für experimente mit exotischen strahlen. Master's thesis, Technische Hochschule, Darmstadt, Germany, 1994. not published.

[63] A. Sirlin. *Remarks concerning the $O(Z\alpha^2)$ corrections to Fermi decays, conserved-vector-current predictions, and universality.* *Physical Review D*, 35(11):3423–3427, 1987.

[64] T. Suzuki and T. Otsuka. Configuration of the two-neutron halo of ^{11}li and gamow-teller transition. *Physical Review C*, 50(2):R555–R558, 1994.

[65] I. Tanihata, H. Hamagaki, O. Hashimoto, Y. Shida, N. Yoshikawa, K. Sugimoto, O. Yamakawa, T. Kobayashi, and N. Takahashi. Measurements of interaction cross sections and nuclear radii in the light p-shell region. *Physical Review Letters*, 55(24):2676–2679, 1985.

[66] University of Chicago. *Encyclopædia Britanica*, volume 2, 1974. page 172-173.

[67] D. H. Wilkinson and B. E. F. Macefield. A parametrization of the phase space factor for allowed β-decay. *Nuclear Physics A*, 232:58–92, 1974.

[68] S. Wolfram. *Mathematica - A system for doing mathematics by computer.* Addison-Wesley Publishing Company, Inc., 2nd edition, 1991.

[69] C. S. Wu and S. A. Moszkowski. *Beta decay.* John Wiley & Sons, New York, 1966.

[70] M. V. Zhukov, B. V. Danilin, D. V. Fedorov, J. M. Bang, I. J. Thompson, and J. S. Vaagen. *Bound state properties of Borromean halo nuclei: ^{6}He and ^{11}Li.* *Physics Reports*, 231(4):151–199, 1993.

List of Figures

List of Tables